Coupled Black Hole and Galaxy Formation in the Young Universe

THOMAS ANDREW TARGETT

Institute for Astronomy

School of Physics

University of Edinburgh

Doctor of Philosophy

March 2007

Abstract

This thesis presents results from three major imaging studies designed to determine the properties of massive galaxies selected at high redshift. The most massive known galaxies at high redshift (i.e. radio galaxies), the most massive known starbursts at high redshift (i.e. submillimetre galaxies), and the most massive known black holes at high redshifts (i.e. quasars) have been targeted, with the aim of better establishing the relationship between these different classes of massive object.

The results from deep $K-$band imaging of the most luminous radio galaxies at $z \sim 2$ and the brightest submillimetre sources in the 8- mJy survey are presented. Morphological properties are measured and compared to explore whether submillimetre hosts are the progenitors of today's most massive ellipticals. Two-dimensional modelling finds that the high-redshift radio galaxies have surface brightness distributions consistent with those expected for classic ellipticals (Sérsic parameter, $n = 4$), with n in the range $2.5 < n < 5.75$ and $< n >= 4.04 \pm 0.27$. In contrast, submillimetre galaxies are found to be disks (Sérsic parameter, $n = 1$) with n in the range $1.0 < n < 2.5$ and $< n >= 1.46 \pm 0.16$. The half-light radii of the radio hosts are distributed over a range $2 < r_{1/2} < 16$ kpc with $< r_{1/2} >= 7.85 \pm 1.2$ kpc, while submillimetre sources are smaller, with $1 < r_{1/2} < 6$ kpc and $< r_{1/2} >= 3.15 \pm 0.29$ kpc. The $z \sim 2$ radio galaxies are found to be, on average, a factor ~ 2 smaller than massive radio galaxies at $z < 1$ and follow a Kormendy $(\mu_e - r_e)$ relation similar to that of 3C-type galaxies at low redshift after evolutionary corrections, assuming a burst-formation model at $z = 3$, consistent with the median redshift of the submillimetre sources. The luminosities of the submillimetre galaxies are ~ 1.5 magnitudes brighter than Lyman-break galax-

ies at comparable redshifts, indicating that submillimetre galaxies are significantly more massive. Finally, surface mass densities for both source types are found to be consistent with quiescent elliptical galaxies at high redshift, and not star-forming or Lyman-break galaxies.

The results are presented of a study that uses the 3CRR sample of radio-loud active galactic nuclei to investigate the evolution of the black-hole:spheroid mass ratio in the most massive early-type galaxies from $0 < z < 2$. Radio-loud unification is exploited to obtain virial (linewidth) black hole mass estimates from the 3CRR quasars, and stellar mass estimates from the 3CRR radio galaxies, thereby providing black hole and stellar mass estimates for a single population of early-type galaxies. At low redshift ($z \lesssim 1$) the 3CRR sample is consistent with a black-hole:spheroid mass ratio of $M_{bh}/M_{bulge} \simeq 0.002$, in good agreement with that observed locally for quiescent galaxies of similar stellar mass ($M_{bulge} \simeq 5 \times 10^{11}\,\mathrm{M}_{\odot}$). However, over the redshift interval $0 < z < 2$ the 3CRR black-hole:spheroid mass ratio is found to evolve as $M_{bh}/M_{bulge} \propto (1+z)^{2.07 \pm 0.76}$, reaching $M_{bh}/M_{bulge} \simeq 0.008$ by redshift $z \simeq 2$. If confirmed, the detection of evolution in the 3CRR black-hole:spheroid mass ratio further strengthens the evidence that, at least for massive early-type galaxies, the growth of the central supermassive black hole may be completed before that of the host spheroid.

The results from an ongoing project to constrain the evolution of the black-hole:spheroid mass ratio at $z = 3, 4$ are presented. At these redshifts, quasars and their hosts provide a unique window on this evolution, as the only class of object in which both galaxy and black hole masses can be directly measured. Additionally, the black-hole:bulge mass ratios of flat spectrum quasars at $z \sim 1.5$ are used to determine whether the BLR in AGN possesses a spherical or disk-like morphology. It is demonstrated that both black hole and host galaxy masses can be obtained from emission linewidths and deep high-quality $K-$band imaging respectively. These pilot data represent the first attempt to constrain the black-hole:spheroid mass ratio as part of a statistically significant sample at $z = 3, 4$, a crucial epoch of galaxy formation and evolution.

Declaration

I declare that this thesis is not substantially the same as any that I have submitted for a degree or diploma or other qualification at any other University. I further state that no part of my thesis has already been or is being concurrently submitted for any such degree, diploma or other qualification.

Parts of the work contained in this thesis have been published, or are due to be published, in refereed scientific journals. Chapter 3 is taken from *'On the evolution of the black hole:spheroid mass ratio'*, McLure et al. (2006), MNRAS, 368, 1395-1403

This thesis is the outcome of my own work except where specifically indicated in the text.

Thomas Targett
Edinburgh,
March 2007

Contents

List of Figures

List of Tables

CHAPTER 1

Introduction

This thesis is concerned with high-redshift galaxies and the cosmological evolution of their stellar masses, morphologies, and black holes. A detailed discussion of relevant current research is presented in each chapter. This introductory chapter outlines the general principals and concepts used throughout the thesis.

1.1 Galaxies

Galaxy morphologies are categorised by the distribution of component stars and resulting surface brightness profiles. Hubble (1926) defined three primary groups: elliptical, spiral, and irregular. Current observations confirm that the vast majority of massive galaxies are spiral or elliptical.

Spiral galaxies

Ranging in mass from $\sim 10^9\,\mathrm{M}_\odot$ to $\sim 10^{13}\,\mathrm{M}_\odot$ and in size from ~ 1 to ~ 250 kpc, spiral (and barred spiral) galaxies are the most common known galaxy type. High levels of

star formation are often associated with these typically young, gas-rich environments, frequently localised in the spiral arms. Spiral galaxy surface brightness distributions are approximated by an exponential profile.

Elliptical galaxies

Elliptical (spheroidal) galaxies range in mass from $\sim 10^5\,M_\odot$ to the most massive bound stellar systems known at $\sim 10^{13}\,M_\odot$. Galaxy sizes are found to vary between ~ 1 and ~ 200 kpc. Preferentially located in cluster environments, ellipticals are typically gas-poor, with little star formation activity found in these old red systems. The dominant random motion of stars leads to a smooth surface brightness profile best approximated by a de Vaucouleurs law.

1.1.1 Surface brightness profiles

Galaxy surface brightness profiles are well described by an exponential profile for the disk component and a de Vaucouleurs law ($r^{1/4}$) for the spheroid (hereafter 'bulge'). The exponential is described in Equation 1.1

$$\begin{aligned} \Sigma(r) &= \Sigma_0 exp\left(-\frac{r}{\alpha}\right) \\ \mu(r) &= \mu_0 + 1.0857\left(\frac{r}{\alpha}\right) \end{aligned} \tag{1.1}$$

where Σ_0 and μ_0 are the central surface brightness in $\mathrm{Wm^{-2}Hz^{-1}arcsec^{-2}}$ and magnitudes $\mathrm{arcsec^{-2}}$ respectively, and α is the exponential scalelength. The de Vaucouleurs (1959) profile is described in Equation 1.2

$$\begin{aligned} \Sigma(r) &= \Sigma_{r_e} exp\left\{-7.669\left[\left(\frac{r}{r_e}\right)^{1/4} - 1\right]\right\} \\ \mu(r) &= \mu_{r_e} + 8.327\left[\left(\frac{r}{r_e}\right)^{1/4} - 1\right] \end{aligned} \tag{1.2}$$

where r_e is the half-light or effective radius (radius enclosing half of the galaxy's flux). Σ_{r_e} and μ_{r_e} are the surface brightness measured at r_e. The constants are calculated such that half of the galaxy light is enclosed when the profile is integrated to r_e.

Sérsic (1968) gives a generalised form for surface-brightness profiles, shown in Equation 1.3

$$\Sigma(r) = \Sigma_{r_e} exp\left\{k\left[\left(\frac{r}{r_e}\right)^{1/\beta} - 1\right]\right\}$$
$$\mu(r) = \mu_{r_e} + 1.0857\left[\left(\frac{r}{r_e}\right)^{1/\beta} - 1\right] \tag{1.3}$$

where $k = 1.99992\beta - 0.3271$ (Capaccioli et al. 1989). The de Vaucouleurs and exponential profiles are represented in Equation 1.3 where $k = 7.669$ and $\beta = 4$ for ellipticals and $k = 1.678$ and $\beta = 1$ for disks. Conversion between half-light radius and scalelength is then expressed in Equation 1.4.

$$r_e = k^{\beta}\alpha \tag{1.4}$$

When fitting galaxy surface brightnesses with the Sérsic profile, the Sérsic index n (where $n = \beta$) is adopted to describe the behaviour of the profile.

1.2 Active and high-redshift galaxies

Active Galactic Nucleus (AGN) refers to the existence of energetic phenomena in the nucleus (or central region) of galaxies that cannot be attributed clearly and directly to stars. AGN are classified by luminosity, spectral energy distribution (SED) content, and radio properties. Historically AGN are classified into several subclasses: Seyfert galaxies, quasars, radio galaxies, BL Lac objects, and optically violent variables. Example spectra for common classes of AGN are shown in Figure 1.1.[1] The properties of Seyfert galaxies, quasars, radio galaxies, submillimetre galaxies, and several classes of high-redshift galaxy are discussed below.

[1]Image from http://www.astro.queensu.ca.

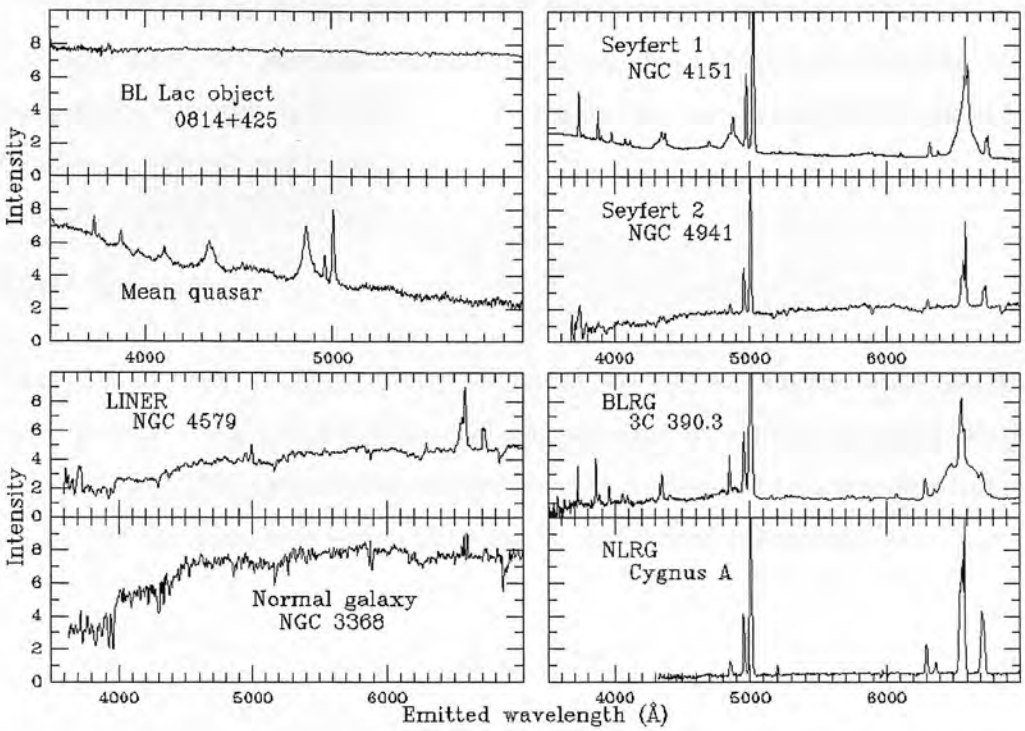

Figure 1.1: Examples of averaged spectra for common AGN types.

1.2.1 Seyfert galaxies

Seyfert galaxies are lower-luminosity AGN ($M_B > -21.5 + 5log h_o$ criteria from Schmidt & Green 1983), categorised by a compact unresolved nucleus $\sim 10 - 100$ times more luminous than the typically resolved spiral host. The optical spectra contain strong high-ionisation emission lines. Seyfert galaxies are subcategorized as Type 1 or Type 2 by emission linewidth. Type 1 Seyferts have two sets of emission lines superimposed on the host and AGN continuum spectra. The first set is characteristic of low-density ionised gas with widths corresponding to velocities of several hundred kilometres per second (broader than emission linewidths in quiescent galaxies), and referred to as narrow lines, i.e. FWHM < 2000km s^{-1}. The second set, known as broad lines (i.e. FWHM > 2000km s^{-1}), is characteristic of high-density gas with velocities of several thousand kilometres per second. By contrast, Type 2 Seyfert galaxies present only narrow emission linewidths.

In addition to the strong emission lines, weak absorption features associated with late-type stars in the host galaxy are seen in the spectra of Type 1 & 2 Seyferts. However, these absorption features are typically diluted by the non-stellar 'featureless continuum' associated with the AGN.

1.2.2 Quasars

Quasi Stellar Objects (QSOs), known as quasars, are the most luminous class of AGN ($M_B < -21.5 + 5log h_o$). Quasar host galaxies are typically old massive ellipticals (e.g. Dunlop et al. 2003), generally unresolved beneath the dominant nuclear light from the AGN. The dominant broad-band SEDs can be represented as a power law

$$F_\nu = C\nu^{-\alpha} \tag{1.5}$$

where α is the power-law index , C is a constant, and F_ν is the specific flux, usually given in $\mathrm{ergs\,s^{-1}cm^{-2}Hz^{-1}}$. Emission lines in quasar spectra are markedly similar to those of Type 1 Seyferts, possessing both broad and narrow emission lines superimposed upon the dominant featureless continuum and host galaxy.

1.2.3 Radio galaxies

Broad-line and narrow-line radio galaxies exhibit spectra similar to those of Type 1 and Type 2 Seyferts respectively, although unlike Seyferts, radio galaxy hosts are typically elliptical rather than spiral. With little or no contribution to galaxy light from the AGN in the optical or infrared, radio hosts appear quiescent. However, some extended line emission in the direction of the radio jets is often found, consistent with the so-called alignment effect (e.g. van Breugel, Heckman & Miley 1984; Inskip et al. 2002).

Radio morphology can be broadly described in terms of two components: the 'extended' spatially resolved and the 'compact' unresolved (at 1" resolution). The extended component morphology is generally double, with lobes of radio emission often on megaparsec scales located symmetrically astride the host. The compact component

is often coincident with the optical position of the AGN. One of the significant differences between the extended and compact components is that the extended regions are optically thin to their own synchrotron emission, whereas the compact component is not. Very long baseline interferometry yields upper limits on the size of the compact core, typically of the order ~ 0.001pc.

Extended radio structures can be further divided into two separate luminosity classes (Fanaroff & Riley 1974). The fainter Class I (FRI) are edge-darkened, with decreasing surface brightness towards their limbs. The more luminous FRII sources are edge-brightened, believed to arise from shock heating as the radio-emitting plasma interacts with the intergalactic medium.

1.2.4 Submillimetre galaxies

Submillimetre (submm) galaxies, selected by their significant (> 3 mJy at $850\,\mu$m) submm fluxes, exceed the submilliJansky level expected from stellar SED models at these wavelengths (Mortier et al. 2005). Current theory suggests that submm hosts are heavily dust-obscured star-forming galaxies, re-radiating absorbed optical/ultraviolet light at submm wavelengths. Such galaxies would be expected to have much higher infrared luminosities than would be inferred from optical/ultraviolet observations alone. Although difficult to constrain, current estimates place these sources at high redshift. Assuming a standard solar neighbourhood initial mass function (IMF), the observed $850\,\mu$m flux densities of several mJy imply star formation rates (SFRs) of $\sim 1000\,\mathrm{M_\odot yr^{-1}}$. It has been suggested that submm galaxies are the progenitors of present-day massive ellipticals (Hughes et al. 1998; Scott et al. 2002), given that: 1) the inferred star-formation rates from the submm flux densities are sufficient to assemble the stellar population of the most massive elliptical galaxy in ~ 1 Gyr; 2) the co-moving number density of bright submm sources in the redshift interval $z = 2 - 3$ is comparable to the present-day number density of bright $> 2 - 3L^\star$ ellipticals (Scott et al. 2002); 3) tentative detections of clustering suggest that the submm galaxies trace the collapse of rare, high-density overdensities at high redshift (Almaini et al. 2003; Greve et al. 2004).

1.2.5 Extremely red objects

Reported in Elston, Rieke & Rieke (1988), extremely red objects (EROs) are typically defined as having $R - K > 5$ or $I - K > 4$ in Vega (Caputi et al. 2004). The traditional picture identifies EROs with either passively evolving elliptical galaxies or young starbursts strongly reddened by dust at $z > 1$. This view has been confirmed by spectroscopic (Dunlop et al. 1996; Soifer et al. 1999; Cimatti et al. 2002; Saracco et al. 2003) and submillimetre surveys (Cimatti et al. 1998; Dey et al. 1999; Wehner, Barger & Kneib 2002).

1.2.6 Distant red galaxies

Distant red galaxies (DRGs) are selected by a colour-cut criterion of $J - Ks > 2.3$, in Vega (Saracco et al. 2001; Franx et al. 2003; van Dokkum et al. 2003), believed to select galaxies with prominent rest-frame optical breaks at $z > 2$. The DRG population comprises both passively evolving elliptical galaxies and young dust-enshrouded starbursts, similar to the dual population found for EROs. Results from Lane et al. (2007) show that DRGs from the redder end of the sample are similar to (and also selected as) EROs, indicating overlap between the two classes of red object.

1.2.7 Lyman-break galaxies

The Lyman-break technique uses colour selection to identify high-redshift galaxies through multiband imaging across the rest frame 912Å Lyman-continuum discontinuity (Steidel et al. 1996, redshifted into the optical window. Galaxies selected in this way are referred to as Lyman-break galaxies (LBGs). LBGs are found to be dust-enshrouded starbursts, possessing star-formation rates > 10 solar-masses/yr (Rigopoulou et al. 2006) and considerable amounts of dust (e.g., Sawicki & Yee 1998, Rigopoulou et al. 2006). LBGs are typically bluer than EROs and DRGs.

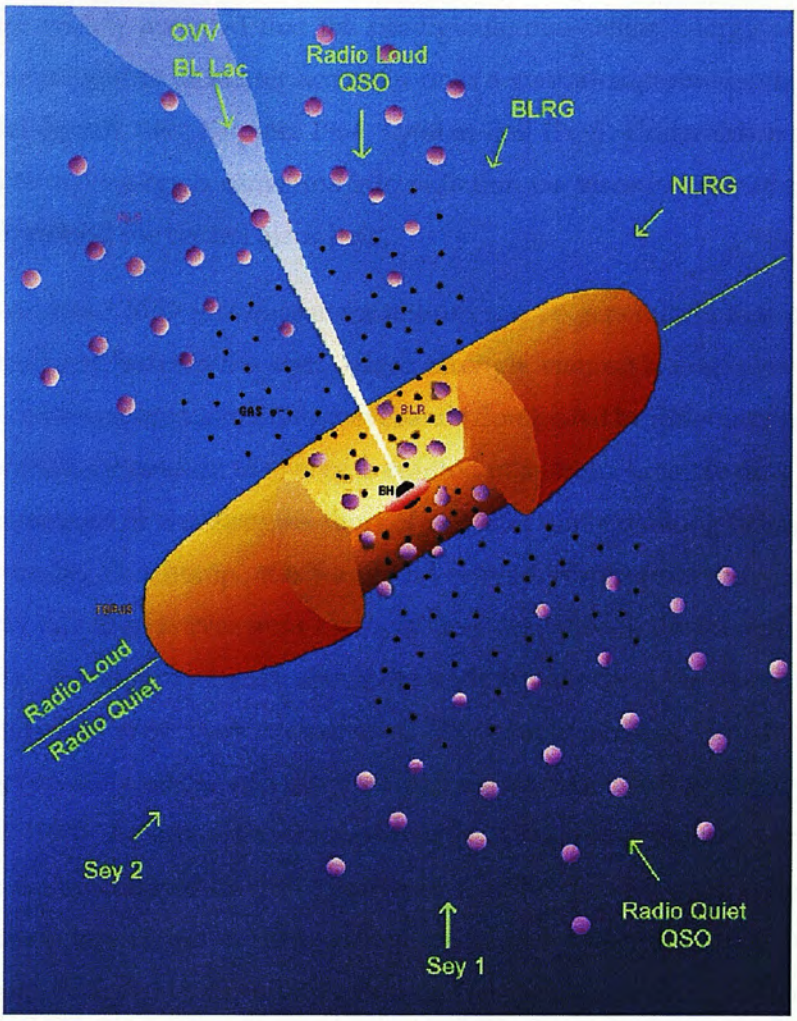

Figure 1.2: The standard model of AGN. Viewing angle towards a common central engine determines the observed properties of the system. The top and bottom sections show the radio-loud and radio-quiet regimes respectively.

1.3 The standard model of AGN

Observationally, a small but significant fraction of galaxies are dominated by emission from a concentrated central region of small angular size (e.g. Peterson 1997). Under the well-established, orientation-dependent unification picture (e.g. Barthel 1989; Antonucci 1993), a central engine common to all classes of AGN can explain the various observed properties depending upon viewing angle. An example of this unified scheme is shown in Figure 1.2.[2]

[2]Image from http://www.star.le.ac.uk.

It is now widely accepted that the prodigious, non-stellar, energy output from AGN is a consequence of matter accretion onto a central super-massive black bole (SMBH) (Zel'dovich 1964, Salpeter 1964, Lynden-Bell 1969). Under this model, gravitational potential energy is converted into radiation via viscous dissipation in an accretion disk around the central black hole.

The broad-band SED of a quasar continuum can be generalised to a power law. Several significant features are seen, which strongly suggest a multiple-component continuum, with emission in various wavebands dominated by different physical processes. A significant amount of energy is emitted in a strong broad feature that dominates the spectrum at wavelengths short of $\sim 4000\mathring{A}$ and extending beyond the UV. Known as the 'big blue bump', this feature is believed to arise from the superposition of blackbody radiation curves from a temperature gradation in the accretion disk (Peterson 1997). A soft X-ray excess above the underlying power-law spectrum is also found, believed to arise from up-scatter of UV/optical photons from the accretion disk by hot (possibly relativistic) electrons in a corona surrounding the disk (Haardt & Maraschi 1993). At submillimetre wavelengths, UV/optical photons can be reprocessed into the far-infrared by dust to produce brighter than expected submm fluxes. Studies of the submm regime also reveal a sharp drop in power known as the 'submillimetre break', believed to arise from a drop in the emitting efficiency of small grains at low frequencies (Draine & Lee 1984).

Around the black hole/accretion disk system are fast-moving clouds of gas, highly ionised by the nuclear light, giving rise to the broad emission linewidths seen in quasars and Type 1 Seyferts. These broad lines are for permitted transitions only, implying that cloud density is sufficiently high to suppress forbidden transitions. The morphology of this broad-line region (BLR) is currently unconstrained. The BLR is surrounded by a large dusty region, typically referred to as the torus. Where the observer's viewing angle intersects the torus, emission from both the accretion disk and the BLR are obscured. A continuum of fast-moving gas clouds extends from the BLR, whose orbital velocity and density fall with increasing radius from the black hole. This continuum is subclassified into the narrow line region (NLR) and extremely

narrow line region (ENLR), where both forbidden and permitted transitions give rise to the narrow emission lines common to AGN spectra. Additionally, approximately 10 per cent of AGN are classified as radio-loud, with highly columnated radio jets emanating from their nuclei (Mushotzky 2004).

Under this orientation-based model, viewing angle towards the central engine and obscuration by the torus governs the observed properties of AGN. When the observer's line of sight does not intersect the dusty torus, AGN spectra contain varying degrees of Doppler-boosted nuclear light (typically dominating the host) and the broad and narrow emission lines associated with the BLR and NLR. When the observer's line of sight intersects the torus, both nuclear and BLR emission are obscured, and the resulting spectra comprise only narrow emission lines superimposed upon those of the host galaxy.

1.4 Super-massive black holes

It is now established that at low redshift essentially all massive galaxies contain a central super-massive black hole (Kormendy & Richstone 1995, and references therein). Several empirical correlations are found between black hole mass (M_{bh}) and host galaxy properties, such as stellar velocity dispersion (e.g. Tremaine et al. 2002), radio luminosity (e.g. Laor 2000), and mass of the host spheroid (e.g. McLure & Dunlop 2002). In consequence, it is widely accepted that the formation and evolution of super-massive black holes and their host galaxies must be intimately related. Clearly, the co-evolution of black hole and host is critical to the understanding of galaxy formation and evolution.

At present, M_{bh} can only be inferred from the orbital radius and velocity of stars and gas around the black hole (see Equation 1.6). Several methods are available to determine M_{bh} at low redshift. Genzel et al. (1997) resolve stars in Keplarian orbits around the central black hole in the Milky Way using $K-$band observations in five epochs between 1992 and 1996. These data imply the presence of a $\sim 10^6\,\mathrm{M}_\odot$ black hole. For local galaxies, where regions surrounding the central engine can be resolved

with the Hubble Space Telescope (HST), stellar velocity dispersions (e.g. Young et al. 1978) and gas dynamics (e.g. Harms et al. 1994) can be used to estimate M_{bh}. However, difficulty in resolving stellar or gas velocity dispersions around black holes render such techniques impracticable at high redshift.

$$M_{bh} = G^{-1} R_{orb} V_{orb}^2 \tag{1.6}$$

1.4.1 Reverberation mapping and virial mass estimators

At present, the most direct measurements of AGN central black hole masses at high redshift come from the reverberation mapping studies of 17 Seyferts and 17 PG quasars by Wandel et al. (1999) and Kaspi et al. (2000), respectively. Reverberation mapping uses the time lag between variations in the AGN continuum and the resulting reverberation of the broad emission lines to provide a direct measurement of BLR radius from the central ionizing source ($R_{BLR} = c\tau$, where τ is the time lag between the continuum and Hβ variations). By combining these measurements with the assumption that the FWHM of the broad emission linewidths reflects the virialized bulk motion of the line-emitting material, the so-called virial estimate of the central black hole mass can be produced (see Wandel et al. 1999, for a full discussion).

Although the virial mass estimate is potentially subject to many uncertainties (e.g. Krolik 2001), comparison with predictions of the completely independent relation between black hole mass and host-galaxy stellar velocity dispersion have shown the two to be in excellent agreement (Ferrarese et al. 2001; Gebhardt et al. 2000).

Given the observation-heavy requirements of measuring black hole mass via reverberation mapping, it is unrealistic to expect that measurements can be obtained for large samples of quasars, even at low redshift. However, the existing reverberation mapping of low-redshift AGN reveals correlations between R_{BLR} and the monochromatic AGN continuum luminosity at 1350Å, 3000Å, and 5100Å (e.g. Kaspi et al. 2000; McLure & Jarvis 2002; Vestergaard & Peterson 2006). Examples of these correlations from McLure & Jarvis (2002) are shown in Figure 1.3. Under the assumptions that BLR

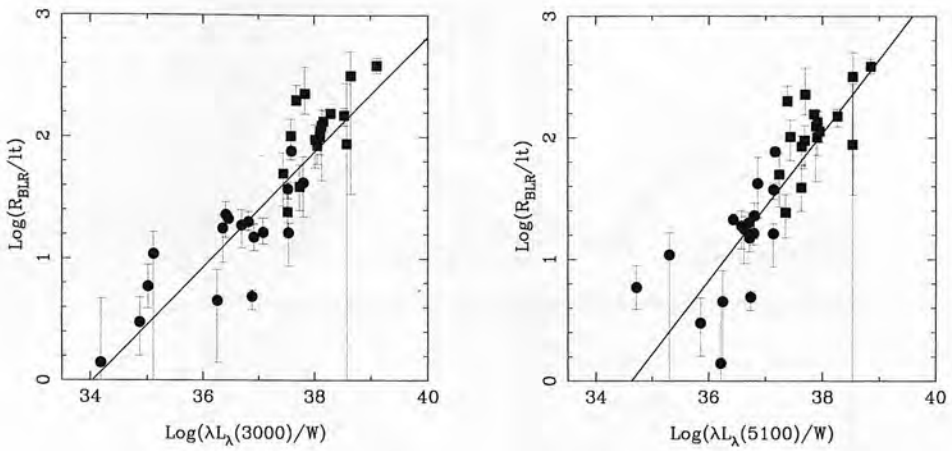

Figure 1.3: The correlation between broad-line radius and AGN continuum luminosity at 3000Å and 5100Å from McLure & Jarvis (2002). The 17 PG quasars are shown as filled squares and the 17 Seyfert galaxies as filled circles.

width traces the Keplarian velocity of the broad-line gas (e.g. Peterson & Wandel 2000; Onken & Peterson 2002) and that R_{BLR} correlates with certain monochromatic AGN continuum luminosities, it is possible to produce a virial black hole mass estimate from a single spectrum. The virial mass estimators provide a powerful tool for determining AGN black hole mass at high redshift for a large sample of broad-line AGN.

1.5 Galaxy masses from SED fitting

Galaxy masses can be estimated from multi-frequency data via evolutionary stellar population synthesis model-fitting to spectral energy distributions (e.g. Bruzual & Charlot 2003). The Bruzual & Charlot 2003 software comprises libraries of model galaxy SEDs derived from integrated stellar populations with specified metallicity, dust content, initial mass function (IMF), and star-formation history as a function of the population age. Input galaxy spectra are matched to the best-fit model SED via chi-squared fitting. Total stellar mass can then be estimated from the star-formation history of the best-fit model.

Critical to the determination of galaxy mass from SED fitting is the UV-to-optical flux ratio (e.g., the inflection around the Balmer/4000$\AA$ break), which gauges the ratio of early-type to late-type stars, diagnosing the past star-formation history of a galaxy.

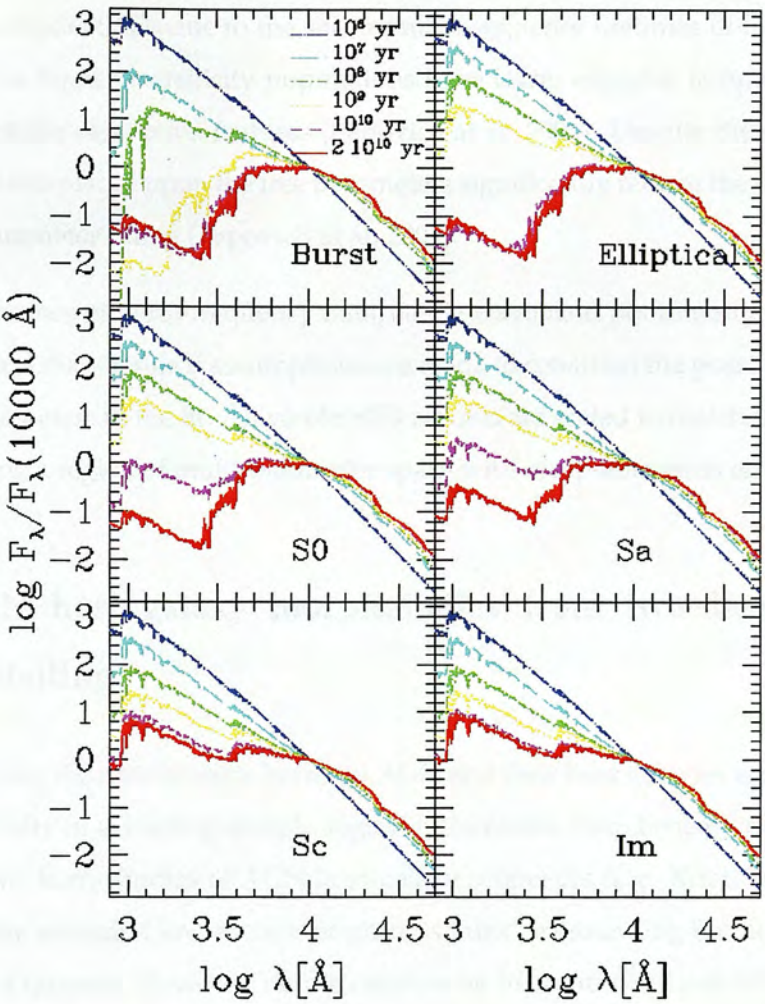

Figure 1.4: Examples of stellar population synthesis model evolution with age.

An example of a model SED's evolution with age is shown in Figure 1.4. [3]. Depletion of early-type stars with age increases the prominence of the 4000Å/Balmer break, providing a useful diagnostic of stellar age (see Papovich et al. 2001 and references therein). However, the behaviour of this spectral feature is degenerate with other free parameters in the fit. A non-instantaneous SFR can mask the effects of stellar-population aging by maintaining emission at wavelengths $< 4000Å$. Attenuation by dust can also affect estimated stellar population age, where shorter wavelengths are more readily reprocessed into the far-infrared, mimicking the appearance of an aging stellar population (e.g. Madau et al. 1996). Furthermore, increasing the metallicity

[3]Image from http://webast.ast.obs-mip.fr/hyperz/

reddens the model SEDs due to the shorter main-sequence lifetimes of higher metallicity stars, as higher metallicity populations have lower effective temperatures and stronger metallic absorption features (Papovich at al. 2001). Despite these degeneracies, constraints placed upon the free parameters significantly reduce the likelihood of incorrect parameter fitting (Papovich at al. 2001).

In the absence of multi-frequency data, single waveband photometry can be used to determine a mass range if assumptions are made to constrain the possible values of the free parameters in the fit. All viable SED models are scaled to match the available data, defining a region of multi-parameter space with acceptable mass estimates.

1.6 AGN host galaxy morphologies from two-dimensional modelling

Understanding the relationships between AGN and their host galaxies is complicated by the difficulty in extracting morphological information from beneath the dominant nuclear light. Early studies of AGN host-galaxy properties (e.g. Kristian 1973) were limited to the extended low surface-brightness 'fuzz' surrounding the dominant nuclear light of quasars. However, no information on the centre of these AGN could be extracted, nor could high-redshift AGN be examined given that the angular size of the PSF was larger than the host.

Smith et al. (1986) used one-dimensional radial profile fitting to determine relative contributions from AGN and host. However, one-dimensional profile fitting is limited by its inability to model the effects of a source's axial ratio or position angle on the half-light radius and surface-brightness parameters.

Two-dimensional modelling can be used to to recover both the nuclear-to-host flux ratio and morphological information from AGN hosts. Full details of the two-dimensional modelling code used here can be found in McLure et al. (2000). Using this code, a model galaxy is constructed with the free parameters:

- L_{nuc} = luminosity of nuclear component
- L_{host} = luminosity of host galaxy
- μ_e = surface brightness
- $r_{1/2}$ = half-light radius
- Θ = position angle
- $\frac{a}{b}$ = axial ratio
- n = Sérsic index

Using one-dimensional radial profile fitting, an initial model (with or without the nuclear point source) is created and convolved with a PSF derived from either the original image or simulation. Each pixel in the fit is assigned an error based on its Poisson (shot) noise (assuming independence of adjacent pixels), and the χ^2 of the PSF-convolved model galaxy is measured against the original data. By incremental modifications to the free parameters, χ^2 is minimised using a downhill-simplex technique (Press 1992) until a minimum is found. In order to ensure that the solution was stable (and not a local minimum), the modelling code was repeatedly restarted from close to the minimum solution. Each iteration started with the best-fit values from the previous run, modified with a random perturbation. After the final modelling iteration, the model galaxy was then re-binned to a higher resolution and the best-fitting solution was shifted around the image centroid to account for possible sub-pixel misalignment between the model and data.

McLure et al. (2000) find that modelling of galaxy parameters from simulated data recovered values to within ~ 10 per cent of the original. As emphasised in McLure et al. (2000), the success of this modelling depends on an accurate high-dynamic-range PSF.

1.7 Galaxy evolution

In the local universe, the population of massive galaxies (stellar masses $> 10^{11}\,M_{\odot}$) is dominated by early-types (Baldry et al. 2004) of large size (Shen et al. 2003). These relaxed ellipticals typically contain old, metal-rich stellar populations that are believed to have formed rapidly in the early universe (Heavens et al. 2004; Feulner et al. 2005; Thomas et al. 2005). However, it is currently not known whether these stars formed in the same system or in lower-mass galaxies that later coalesced.

Two main formation models have been proposed in order to explain the properties of these galaxies: the so-called monolithic collapse model (Eggen, Lynden-Bell & Sandage 1962; Larson 1975; Arimoto & Yoshii 1987; Bressan, Chiosi & Fagotto 1994) and the hierarchical merging scenario (Toomre 1977; White & Frenk 1991). Both models are supported by different numerical simulations, and each accounts for elements of the current observations. The fast and dissipative monolithic collapse model accounts for the majority of stars in massive ellipticals being old (Mannucci et al. 2001) and rapidly formed (indicated by high [α/FE] ratios, as seen in Worthey et al. 1992). Analytically, cold dissipationless collapse (van Albada 1982; May & van Albada 1984; McGlynn 1984; Aguilar & Merritt 1990; Londrillo et al. 1991; Udry 1993; Hozumi et al. 2000; Trenti 2005), a process believed to dominate the last stages of highly dissipative collapse, can reproduce well the structural and dynamical properties of local spheroid galaxies. The hierarchical merging scenario is supported by the observed decline in the number of massive galaxies seen with increasing redshift. This decline is moderate since $z \sim 1$, and increases beyond this (Daddi, Cimatti & Renzini 2000; Pozzetti et al. 2003; Bell et al. 2004; Drory et al. 2004 & 2005; Daddi et al. 2005; Saracco et al. 2005; Faber et al. 2005; Pozzetti et al. 2007), indicating that smaller systems merge at higher redshift to produce the number of massive galaxies observed today. Furthermore, recent semi-analytical models using merging as the cornerstone of massive galaxy formation are better able to match the observed stellar populations and properties of local ellipticals (e.g. De Lucia et al. 2006).

Attempts to constrain galaxy-evolution models through cosmic time using number-density analysis or merger-rate estimation have proven challenging, given

the scarcity of massive galaxies and the clustered environment in which they are located (biasing pair fraction estimates). Results from such studies contain high degrees of uncertainty (e.g. Cimatti, Daddi, & Renzini 2006; Renzini 2007). A more robust technique for probing the history of massive galaxies is to examine the size evolution of these systems at a given stellar mass. In a monolithic scenario, in which a galaxy is fully assembled after the rapid formation of all its component stars, the stellar mass-size relation should remain relatively unchanged over cosmic time. In contrast, under the hierarchical merging scenario, the stellar mass-size relation will evolve as a result of the increasing size after each merger. The most massive galaxies can be expected to exhibit the largest size increase with time under the hierarchical merging model, predicted to be on the order of 1.5–3 for galaxies with masses $> 10^{11}\,\mathrm{M}_{\odot}$ (Khochfar & Silk 2006).

1.8 Thesis overview

Chapter 2 outlines how morphological parameters of the brightest radio galaxies at $z \sim 2$ and submillimetre galaxies from the 8 mJy survey are determined via two-dimensional modelling of deep $K-$band imaging. These data are used to determine whether submillimetre hosts are the progenitors of today's massive ellipticals.

Chapter 3 describes the McLure et al. (2006) study using the 3CRR sample of radio-loud active galactic nuclei to investigate the evolution of the black-hole:bulge mass ratio in the most massive early-type galaxies in the range $0 < z < 2$.

Chapter 4 describes a pilot program to determine the black-hole:bulge mass ratio in $z = 3, 4$ quasars. Additionally, black-hole:bulge mass ratios for flat-spectrum quasars at $z \sim 1.5$ are used to ascertain whether the BLR in AGN possesses a spherical or disk-like morphology.

Chapter 5 summarises all results and suggests possible further work.

The following cosmology is adopted throughout: $H_0 = 70\mathrm{km\,s^{-1}\,Mpc^{-1}}$, $\Omega_m = 0.3$, $\Omega_{\Lambda} = 0.7$.

CHAPTER 2

Morphologies of high-redshift submm and radio galaxies

The importance of infrared and submillimetre observations of high-redshift galaxies has long been recognised. In particular, near-infrared observations offer a more robust method of estimating galaxy stellar masses than optical imaging. This is because, for all but the youngest stellar populations, the light at rest-frame wavelengths $\lambda > 1\,\mu\mathrm{m}$ is dominated by the photospheres of evolved or long-lived stars. By contrast, the value of submm observations is such that, especially at high-redshift, they can sample galaxy light close to the peak of far-infrared emission produced by the reprocessing (by dust) of the ultraviolet emission from the youngest massive stars, formed via recent starburst activity.

Both of these complementary advantages were exploited before the advent of either near-infrared or submm imaging cameras. For example, Lilly & Longair (1984) used the single-element bolometer UKT9 on UKIRT to observe 3CR radio galaxies, and provide the first clear evidence of the existence of massive galaxies at redshifts $z > 1$. Ten years later, Dunlop et al. (1994) used the single-element bolometer UKT14

on the James Clerk Maxwell Telescope (JCMT) to measure the star-formation rate and dust/gas mass in what was at that time the most distant known galaxy (again a radio galaxy, 4C41.17) at $z = 3.8$.

However, observations with single-element bolometers have two obvious limitations. First, the position of the target object must be known, so it is only possible to observe objects which have already been discovered at some other waveband. Second, except for very bright galactic sources or nearby galaxies (across which a single-element bolometer can be scanned), it is not possible to obtain even crude morphological information on the near-infrared or submm light from distant galaxies.

Near-infrared imaging arrived in the late 1980s with IRCAM on UKIRT (McLean et al. 1986), while submm imaging was finally realised a decade later with SCUBA on the JCMT (Holland et al. 1998). The advent of near-infrared imaging allowed both the first surveys designed to select galaxies at near-infrared wavelengths (e.g. Glazebrook et al. 1994) and the first morphological studies of high-redshift radio galaxies (e.g. Dunlop & Peacock 1993). The advent of submm imaging enabled the first surveys for submm selected galaxies (e.g. Hughes et al. 1998), which have since revolutionised our picture of star formation in the young universe. Morphological studies at submm wavelengths are much more difficult due to the large (i.e. FWHM $\simeq$ 15 arcsec) size of the Airy disc delivered by the 15-m JCMT at $\lambda \simeq 850\,\mu$m, and are only now becoming possible with the commissioning of the SMA (e.g. Moran et al. 2001). Since these pioneering observations, infrared and submm galaxy surveys have transformed our knowledge of galaxy evolution.

At near-infrared wavelengths, a new generation of near-infrared surveys (e.g. K20. GOODS, GDDS) has now been successfully exploited to delineate the growth of stellar mass density as a function of cosmological time since $z \simeq 3$ (Fontana et al. 2004; Dickinson et al. 2004; Glazebrook et al. 2004; Caputi et al. 2006; Saracco et al. 2006). This work has demonstrated that massive ($\geq 10^{11}\,M_{\odot}$) galaxies are already in place at $z \simeq 2$ (contrary to model predictions of only five years ago), and that > 50 per cent of the local stellar mass density had formed by $z \simeq 1$. These fundamental results have clarified the concept of 'downsizing' and motivated the revision of current galaxy-

formation models (e.g. Bower et al. 2006; Croton et al. 2006) in an effort to match the observations. Under the downsizing model (Cowie et al. 1996), regardless of environment, a lower-mass galaxy forms stars at a later epoch than a more massive one. Specifically, a lower-mass galaxy undergoes the peak of star formation at a later epoch.

At submm wavelengths the data have also presented a major challenge to existing galaxy-formation models (e.g. Baugh et al. 2005), with large-scale surveys such as the 8-mJy survey (Scott et al. 2002; Ivison et al. 2002) and, most recently, the SHADES survey (Mortier et al. 2005; Coppin et al. 2006) revealing large numbers of apparently massive violently star-forming galaxies at redshifts $z \simeq 2$.

A key challenge now is to relate these populations of galaxies, selected at different wavelengths, both to each other and to other known populations of galaxies selected at both high and low redshift. The ultimate aim is to understand these different galaxy populations sufficiently well to define their roles in the history of structure formation within the now well-established ΛCDM cosmological framework.

In this chapter we attempt to take a step towards this goal via a deep, and high-quality near-infrared imaging study of a sample of luminous submm galaxies at $z \simeq 2$, and a comparison sample of the most luminous radio galaxies known at comparable redshifts. The primary aim was to compare the rest-frame optical properties of the submm galaxies with those of the most massive known galaxies at a comparable epoch. In particular we sought to obtain imaging of sufficient quality to determine the basic morphologies and sizes of the galaxies. There are several reasons why such information is now crucial for further progress in this field, namely:

1. Despite the fact that several hundred submm galaxies have now been uncovered, their nature is still unclear. This is largely because we lack information on the masses, sizes and morphologies of the galaxies which host the observed massive star-formation activity. In particular, it is unclear whether submm galaxies are disc galaxies (as might be expected for gas-rich star-forming systems) or massive ellipticals (as perhaps suggested by their number density, which matches that of present-day $> 2 - 3L^{\star}$ elliptical galaxies). A limited number of submm

galaxies have been studied in the infrared (e.g. Smail et al. 2003), but to date no systematic study of the morphologies of submm galaxies has been undertaken.

2. To judge the relevance of any size and morphological information which might be gleaned from the imaging of the submm galaxies, it is important to assemble data of comparable quality for a well-defined control sample. In this case we have chosen as our control sample the most luminous radio galaxies at comparable redshifts ($z \simeq 2$). This is a useful control sample because, given the now-well-established proportionality of black hole and spheroid mass (e.g. McLure & Dunlop 2002), we can be confident that these objects are the most massive galaxies in existence at this epoch. It is also known that these galaxies will undoubtedly end up as massive ellipticals, so this study offers an opportunity to determine the sizes and morphologies for galaxies that are guaranteed progenitors of massive ellipticals. Rather surprisingly, very-deep high-quality near-infrared imaging of these galaxies has not in fact been undertaken before. As a result, while the morphologies of radio galaxies out to $z \simeq 1$ are rather well defined (see, for example, McLure et al. 2004), their morphologies and sizes at $z \simeq 2$ have yet to be clarified.

3. Finally, in recent years it has become clear that the full power of deep near-infrared imaging can only be realised if the imaging obtained is of sufficient resolution (i.e. from space or in sufficiently good seeing) to allow at least the measurement of basic galaxy size. For example, recently Zirm et al. (2007) were able to demonstrate that passive red galaxies at high redshift are unexpectedly compact and cannot continue to evolve by purely passive evolution into any known type of low-redshift galaxy. By measuring the half-light radii of radio galaxies and submm galaxies at $z \simeq 2$, we therefore aim to shed light on the role of both classes of galaxy within the overall framework of galaxy formation and evolution.

2.1 Sample definition

The full sample in this chapter consists of 39 objects, comprising two subsamples of the 14 brightest radio galaxies at $z \sim 2$ and the 25 brightest submm sources in the 8-mJy survey. The $K-$band morphologies for these two classes of active galaxy are compared to determine if submm hosts are the progenitors of today's massive ellipticals. Full details of these objects are found in Table 2.1.

2.1.1 Radio galaxy sample

Of the 14 objects in the radio galaxy sample, 8 are drawn from the 3CRR catalogue (Laing, Riley & Longair 1983) and 6 from the equatorial Molonglo sample (Best et al. 1999), representing sources in the same extreme radio-power bracket between $1.5 < z < 2.5$. The 3CRR sample is complete to a 178 MHz flux limit of 10.9 Jy over an area of 4.2 steradians and contains a total of 170 steep-spectrum sources over the redshift range $0.0 < z < 2.0$. These data are essentially doubled by the Molonglo sample, a catalogue of radio sources complete down to a flux density limit of 1.01 Jy at 406 MHz. These two surveys provide a complete (*cf* Pentericci et al. 2001) sample of the most powerful, low-frequency-selected, radio sources in the range $1.5 < z < 2.5$. Based upon the early photometry of Lilly & Longair (1984), who establish that the 3CR radio galaxies follow a tight Hubble relationship out to $z > 1$, and near-infrared imaging studies of 3CR hosts (e.g. Dunlop & Peacock 1993, Best et al. 1998), it is generally accepted that bright 3CR radio sources provide an excellent probe of massive galaxies at $z \sim 2$.

2.1.2 SCUBA galaxy sample

The 25 submm galaxies are drawn from the 8-mJy survey, comprising the Lockman Hole East and Elais N2 field, covering 260 arcmin^2 to a typical rms noise level of $\sigma_{850} \simeq 2.5$ mJy beam^{-1} (Scott et al. 2002). These bright submm sources possess a signal-to-noise greater than 3.5σ at 850μm. In total, 17 $K-$band counterparts are identified

using 1.4 GHz imaging from Ivison et al. (2002) (hereafter IV02), $I-$band HST ACS imaging from Almaini et al. (2005), and the 1200 μm MAMBO survey.

2.1.3 Identification of $K-$band counterparts to submm data

Morphological studies at submm wavelengths are difficult, given the large (FWHM $\simeq$ 15 arcsec) size of the Airy disc delivered by the 15-m JCMT at $\lambda \simeq 850\,\mu$m. The identification of $K-$band counterparts to submm positions is also complicated by this large SCUBA error circle. The most robust identifications of submm sources in the 8- mJy survey were made by Ivison et al. (2002), using 1.4 GHz imaging from the Very Large Array (VLA) and ground-based optical and infrared imaging form the WHT and UKIRT respectively. Of the 17 submm sources listed in Table 2.1, 4 are undetected in the Ivison et al. (2002) radio data. These sources must be regarded as ambiguous identifications, and are hereafter separated from the secure radio identifications during analysis. These unsecured identifications were made using $I-$band HST ACS imaging from Almaini et al. (2005), and the 1200-μm MAMBO survey. Following Pope et al. (2005) the criterion that submm galaxies are typically very red in $I-K$ (see also Smail et al. 2004) was used to select the most likely $K-$band counterparts. In the case of LE 850.04, where no optical imaging was available, a $K-$band sources closest to the submm position was selected. It should be noted that although LE 850.04 is therefore the most ambiguous identification, no other $K-$band counterpart exists within the SCUBA error circle.

2.1.4 Redshifts

Obtaining spectroscopic redshifts for submm galaxies is complicated by the difficulty in correctly identifying optical/IR counterparts to submm flux. Where secure identifications exist, spectroscopic redshifts are typically only available for submm sources with optically bright counterparts or strong-lined AGN emission (Chapman et al. 2005). In the absence of secure spectroscopic redshifts, photometric redshifts are adopted from Aretxaga et al. (2007). These redshifts are found to be accurate to $\Delta z <$

Table 2.1: Details of the radio and submm galaxy $K-$band observations. Columns 1 lists the object names for the two samples. Column 2 lists other catalog names or whether a secure radio identification exists. Column 3 lists the date on which the observations were completed. Column 4 lists the total exposure time in seconds for each target. Column 5 lists the measured 6-arcsec aperture magnitude in Vega with associated errors. Columns 6, 7, 8 and list the adopted redshifts, the type of redshift, and associated references: A from Best el al. (1999), B from Hewitt & Burbidge (1991), C from Spinrad et al. (1985), a from Aretxaga et al. (2005), b from Aretxaga, priv. comm., c from Chapman et al. (2003), d from Chapman et al. (2005), e from Ivison et al. (2005), f from Smail et al. (2003).

Source	Object ID	Obs. date	Exp. time	$K-$mag	z	z-type	z-reff
0016−12	3C008	25/08/2003	9480	18.13±0.01	1.589	z_{spect}	A
0128−26	PKS 0128−26	11/08/2005	18840	17.77±0.06	2.348	z_{spect}	A
0231+31	3C 068.2	24/01/2005	9720	17.97±0.04	1.575	z_{spect}	B
0310−15	PKS 0310−15	12/08/2005	8100	18.35±0.08	1.769	z_{spect}	A
0851−14	PKS 0851−14	05/03/2003	10140	17.87±0.02	1.665	z_{spect}	A
1008+46	3C 239	05/03/2003	11820	17.89±0.01	1.790	z_{spect}	C
1019+22	3C 241	12/03/2003	9600	17.75±0.01	1.617	z_{spect}	C
1120+05	3C 257	13/03/2003	22560	17.58±0.01	2.474	z_{spect}	B
1140−11	PKS 1140−11	24/12/2004	13920	18.79±0.05	1.935	z_{spect}	A
1404+34	3C 294	15/06/2003	11340	-	1.780	z_{spect}	B
1422−29	PKS 1422−29	13/03/2003	9600	17.69±0.01	1.632	z_{spect}	A
1533+55	3C 322	16/04/2003	9180	17.86±0.02	1.681	z_{spect}	B
1602−17	PKS 1602−17	16/02/3005	15120	17.63±0.02	2.043	z_{spect}	A
2356+43	3C 470	18/09/2003	10260	18.11±0.09	1.653	z_{spect}	B
N2 850.01	Radio ID	22/02/2002	4750	19.90±0.15	2.85/0.84	z_{spect}/z_{phot}	a/d
N2 850.02	Radio ID	23/03/2003	4500	20.77±0.27	2.454	z_{spect}	d
N2 850.03	ERO/VRO	23/03/2003	4500	21.33±0.27[i]	4.0	z_{phot}	b
N2 850.04	Radio ID	16/06/2002	4625	18.85±0.10	2.387	z_{spect}	f
N2 850.05	-	23/03/2003	5000	-	3.8	z_{phot}	b
N2 850.06	ERO/VRO	07/06/2003	5500	20.18±0.16	3.0	z_{phot}	b
N2 850.07	Radio ID	22/03/2003	5000	20.00±0.16	3.1	z_{phot}	b
N2 850.08	Radio ID	07/06/2003	5000	18.30±0.09	1.19	z_{spect}	d
N2 850.09	ERO/VRO	08/06/2003	4750	20.99±0.37	3.3	z_{phot}	b
N2 850.10	-	11/06/2003	5250	-	3.8	z_{phot}	b
N2 850.11	-	11/06/2003	5375	-	3.7	z_{phot}	b
N2 850.12	ERO/VRO	11/06/2003	5500	20.31±0.17	2.5	z_{phot}	a
N2 850.13	Radio ID	12/06/2003	5375	21.61±0.37	2.283	z_{spect}	d
N2 850.14	-	08/06/2003	4750	-	-	-	-
LE 850.01	Radio ID	22/02/2002	5500	21.09±0.06[i]	2.45	z_{phot}	b
LE 850.02	Radio ID	23/02/2002	5500	19.66±0.11	3.0	z_{spect}	d
LE 850.03	Radio ID	24/12/2002	5500	19.66±0.12	2.239	z_{spect}	d/e
LE 850.04	Submm pos.	22/02/2002	5500	20.74±0.14	3.7	z_{phot}	b
LE 850.05	-	24/12/2002	5500	-	-	-	-
LE 850.06	Radio ID	25/12/2002	5625	19.16±0.17	2.610	z_{spect}	c/e
LE 850.07	Radio ID	25/12/2002	5500	18.87±0.10	3.1	z_{phot}	b
LE 850.08	Radio ID	22/02/2002	5500	20.38±0.16	3.8	z_{phot}	b
LE 850.09	-	27/12/2002	5000	-	-	-	-
LE 850.15	-	25/12/2002	5625	-	2.429	z_{spect}	c
LE 850.17	-	27/12/2002	5000	-	4.0	z_{phot}	b

[i] Sky subtraction estimated for image statistics.

0.5 when compared to existing spectroscopic values. The $/deltaz < 0.5$ uncertainty could influence the derived values from two-dimensional modelling. However, given the high-redshift nature of these sources, modelling results obtained over the range of possible redshifts show no significant difference when compared with the results derived using the actual redshift values given in the literature. All photometric redshifts were assumed to have the largest possible error derived from Aretxaga et al. (2007).

2.2 Observations

2.2.1 UKIRT observations

The 14 radio galaxies were imaged in the $K-$band with the United Kingdom Infrared Telescope (UKIRT) on Mauna Kea. All observations used the UKIRT Fast-Track Imager (UFTI), a 1-2.5μm camera with a 1024^2 HgCdTe array and 0.09085 pixelscale, providing a 1.5′ × 1.5′ field of view. Data were taken in $<$ 0.6-arcsec seeing and photometric conditions. Integration times were set to obtain a signal-to-noise of 5σ at twice the expected half-light radius in the azimuthally binned luminosity profile. Note that even passive evolution of the stellar population offsets to some extent the impact of surface brightness dimming with increasing redshift. Galaxy scalelengths of 10 kpc were assumed, comparable to those found by McLure & Dunlop (2000) for 3CR galaxies at $z = 1$. Total $K-$band magnitudes were estimated using the infrared Hubble diagram of De Breuck et al. (2002).

2.2.2 Gemini observations

Submm sources were imaged in the $K-$band with the Gemini North Telescope on Mauna Kea. All observations used the Near-Infrared Imager (NIRI), a 1-5μm camera with a 1024^2 ALADDIN InSb array. Camera f/6 with a pixelscale of 0.1171 arc pixel^{-1} provided a 2.0′ × 2.0′ field of view. Data were taken in $<$ 0.6 arcsec seeing and photometric conditions. Integration times were constant over all observations at 1.5 hours per source, due to uncertainties in submm galaxy redshifts at the time of obser-

vation. These data reach a depth consistent with the longest exposures for $z > 2$ radio galaxies. Current estimates typically place submm hosts at higher redshifts than the massive radio galaxies, although there is significant overlap between the two samples. Despite the higher redshift of the submm galaxies, Section 2.7 indicates that extended emission is not lost in the wings of the submm sources.

2.3 Data reduction

Rigorous data reduction was critical for accurate determination of host-galaxy parameters. Crucially, full masking of all extended emission visible in a final mosaic is necessary in all flat-fields to avoid introducing unseen (in individual frames) defects. Such flaws result in loss of extended emission in the final image and difficulty in accurately determining parameters such as half-light radius.

Pipeline reductions are now available for most astronomical data, as well as standard IRAF scripts for more detailed manual reductions. Significant improvements in image quality are possible with the rigorous two-stage data reduction described, using IRAF packages and IDL software written for specific tasks. Initially, a mosaiced image (flawed due to source contamination in the flat-field) is created, from which source masks are derived. The masks are then employed in the second phase to eliminate *all* source flux from the flat-fields. The data-reduction process is described below:

- All data were initially processed to incorporate the header component of the multi-extension-fits file (MEF) into the data frame, as IRAF routines typically will not accept MEF files.
- Multiple dark images of integration times equal to the science frames were obtained with all science data, combined to produce an averaged dark frame, and subtracted from the science data.
- In cases where lamp- or dome-flats were available from beginning/end-of-night calibration data, it was found that fluctuations in flat-field structure typically

varied on timescales far shorter than an hour. Consequently, sky-flats are necessary to obtain the higher image quality.

- Data from UKIRT and Gemini were taken in a standard 9-point jitter pattern with 12-arcsec offsets. Individual flat-fields were created for each science frame. Numerous variations in image combination were tested to determine which provided the best image quality in the flat-fielded data. It was found that a median filter combination of neighbouring frames with 2.5σ clipping provided the best image quality, as determined by the standard deviation in a 200×200 pixel patch on each image known to be empty. This level of sigma-clipping was found (by inspection) to remove visible counts from sources and cosmic rays, while not excluding pixels with high relative sensitivities. However, sigma-clipping in individual frames cannot remove the substantial amounts of extended emission around a source that does not appear distinct from the noise until summed. If extended emission is present in any of the frames combined to create the flat, sections of the flat will become biased towards artificially high values. Dividing raw frames by a flat containing such defects will remove flux from around the brighter parts of an excluded source. Loss of such signal will distort the luminosity profile of the object used to determine galaxy parameters. Failure to mask extended emission often results in faint negative defects in a final mosaic (due to positive defects in the flat), with a 9-point pattern around an extended source. Such defects are often buried (although still present) beneath poor sky-subtraction or low-quality flat-fielding in pipeline reductions.

- To achieve best image quality, the number of neighbouring frames combined in the flat-fields must balance better signal-to-noise from including an increasing number of frames against flat-field structure variations with time from fluctuations in detector response and temperature. Flat-field structure was found to be stable for $\sim$15 minutes around each frame. For consistency, images observed at the start and end of the observation were flat-fielded by combining 30 minutes of data preceding or following their observation. All dark-subtracted science frames were then divided by their normalised flat-fields.

- A map of bad pixels in the array was obtained by identifying pixels consistently 3σ below the mean sky level in 80 per cent of the data, regardless of jitter position. These pixels were excluded from the reduction.

- Cosmic ray rejection using sigma-clipping and full-width half-maximum analysis was used to reject cosmic rays from individual images.

- Each frame was individually sky-subtracted using the median sigma-clipped sky value from a 200×200 pixel region known to be devoid of source flux. Sky-subtraction was necessary, as mean image counts and telescope pointing vary during the course of an observation. As a result, bad pixels masked during the observation will appear to move relative to sources on the image. Consequently, some areas around bad pixels will contain only frames from portions of the observation in which they were not masked. If mean image counts were increasing, a patch of sky excluded at the beginning (but observed later as the bad pixels move relatively to the sky) would derive solely from frames with higher mean counts. Conversely, a neighbouring patch (masked after telescope pointing drift) will derive from earlier frames containing lower mean counts.

- Offset frames were registered using the IRAF routine REGISTER. A bright compact star (present at all jitter positions) was identified on each flat-fielded frame. All other stars with a clearly defined peak (as determined by inspection of surface plots) in the linear CCD response regime were then identified in one reference image. An initial alignment was made from the single reference star, which was then modified to find the best-fit for all stars identified in the reference image. The resulting shiftlist therefore compensated for small image rotations or drift over the course of the observation. The FWHM of sources in mosaics derived from this shifting technique were found to be ~ 10 per cent smaller than that in mosaics shifted with telescope-offset-based shiftlists.

- Pixels were summed with the total counts from all frames and normalised by an exposure map constructed during reduction. This initial registered image was then used to create individual masks for all science frames. Masks were tailored to include all source flux in the mosaiced image, without including noise peaks.

- The individual source masks were used in the second phase of reduction. Following the processes described above, frames were re-flat-fielded with the masks to exclude all source flux visible in the final mosaic from each image. Cosmic ray rejection at a higher sigma-clipping level was also possible, as source masks removed the risk of 'zapping' stellar or QSO cores as cosmic rays. These flat-fielded data were then re-reduced to produce a final mosaic for analysis.

2.3.1 Photometry and astrometry

Aperture photometry listed in Table 2.1 was obtained using the IRAF APPHOT package. Imperfections in the sky-subtraction lead to residual sky in the science frames, the removal of which was critical for accurate photometry. An initial sky estimate using sigma-clipped statistics from an annulus about the source was later checked via curve-of-growth analysis, indicating that a slight bias towards high pixel values had resulted in an overestimate of the sky background using the annulus technique. Accurate background levels were obtained via fitting to sky pixels in the curve-of-growth analysis, thus providing an unbiased background level for subtraction. Faint standard stars were observed for each target object for photometric calibration. These data were reduced via the process applied to the science data. Aperture photometry for these stars produced zero-points for each target, consistent around 22.3 ± 0.06 for UFTI and 23.68 ± 0.08 for NIRI data.

Given the numerous faint sources visible in these deep data, accurate astrometry was essential for identifying IV02 radio positions with $K-$band hosts. Using GAIA, finding-charts from the Two Micron All Sky Survey (2MASS) were obtained, and the coordinates of stars present in both the 2MASS data and the $K-$band imaging were used to determine the plate solution for each image. This process took into account any rotation of the array with respect to the north/south axis, typically on the order of 1^o. With the exception of two fields, between 3 and 10 stars were present in both the 2MASS data and in each of the $K-$band images. After correction, the offsets between coordinates of 2MASS sources and their counterparts in the $K-$band data were consistently < 0.1 arcsec.

2.3.2 Point spread function

A point spread function (PSF) for each science frame was built using the IRAF package PSF for use during two-dimensional modelling (see Section 2.4). Stars of comparable brightness to the target were selected and fit with multiple statistical distribution types to determine the best fit. The resulting models were then centroided, averaged, and processed with look-up tables to reproduce any asymmetries in the PSF.

2.4 Host galaxy analysis

The results of two-dimensional modelling for all objects with reliable $K-$band IDs are presented in Table 2.2. Full details of the two-dimensional modelling code can be found in McLure et al. (2000). Modelling of galaxy parameters from simulated data indicated that host morphology is recovered accurately to within ~ 10 per cent. As emphasised in McLure et al. (2000), the success of this modelling depends on an accurate high-dynamic-range PSF. Galaxy parameters are fit by minimising χ^2 using a downhill-simplex technique. The model galaxy is constructed with 5 free parameters: luminosity, scalelength, mean surface brightness, position angle, and axial ratio. In order to ensure that the solution was stable (and not a local minimum), the modelling code was repeatedly restarted from close to the minimum solution.

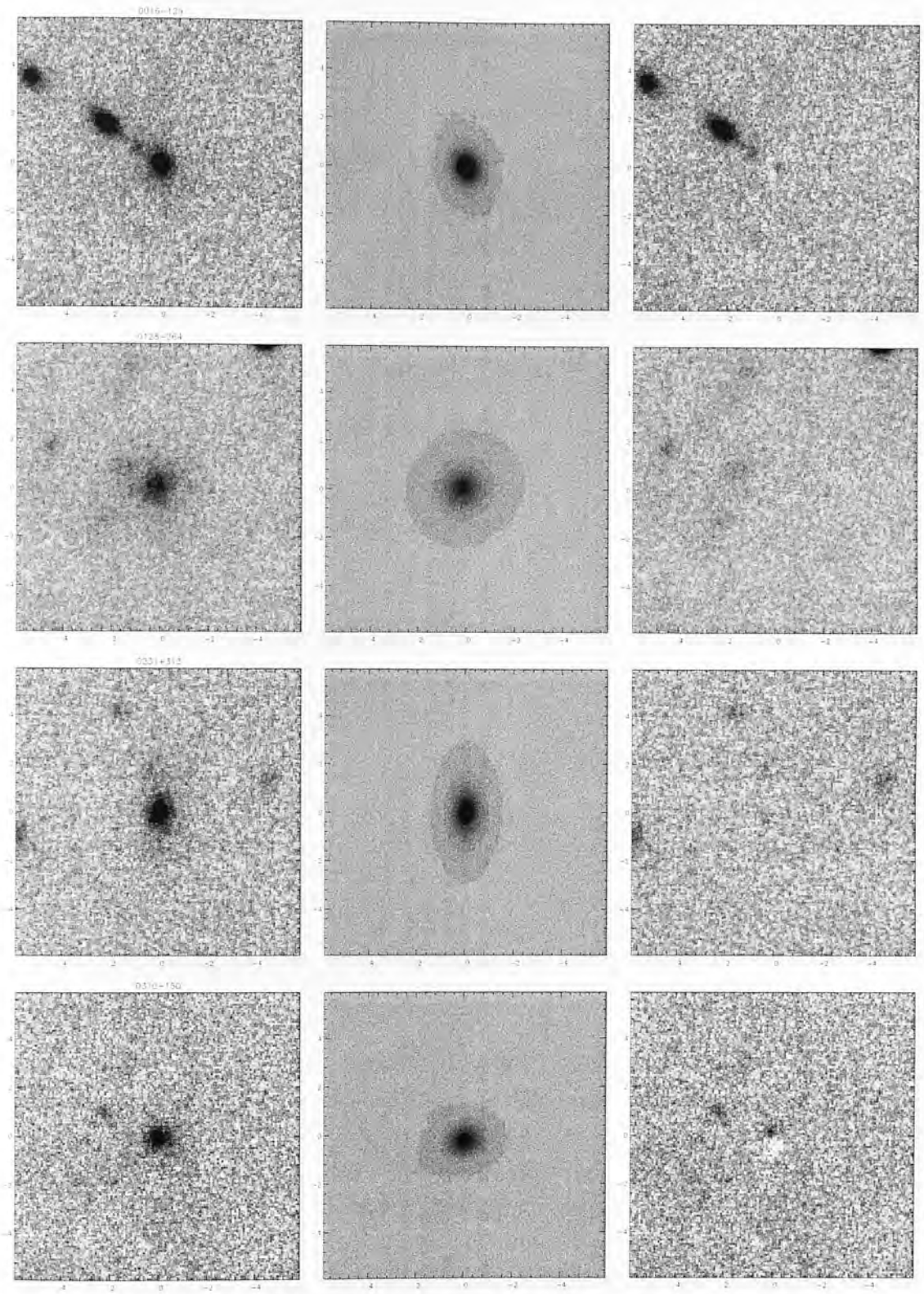

Figure 2.1: Two-dimensional modelling of the $z \sim 2$ radio galaxies. The left-hand panel shows the reduced $K-$band image centred on the radio host. The middle panel shows the best-fitting two-dimensional model. The right-hand panel shows the residual image after subtraction of the model from the science data. All panels are $12.0'' \times 12.0''$. Images are displayed at 2.5σ above and 1σ below the median sky value.

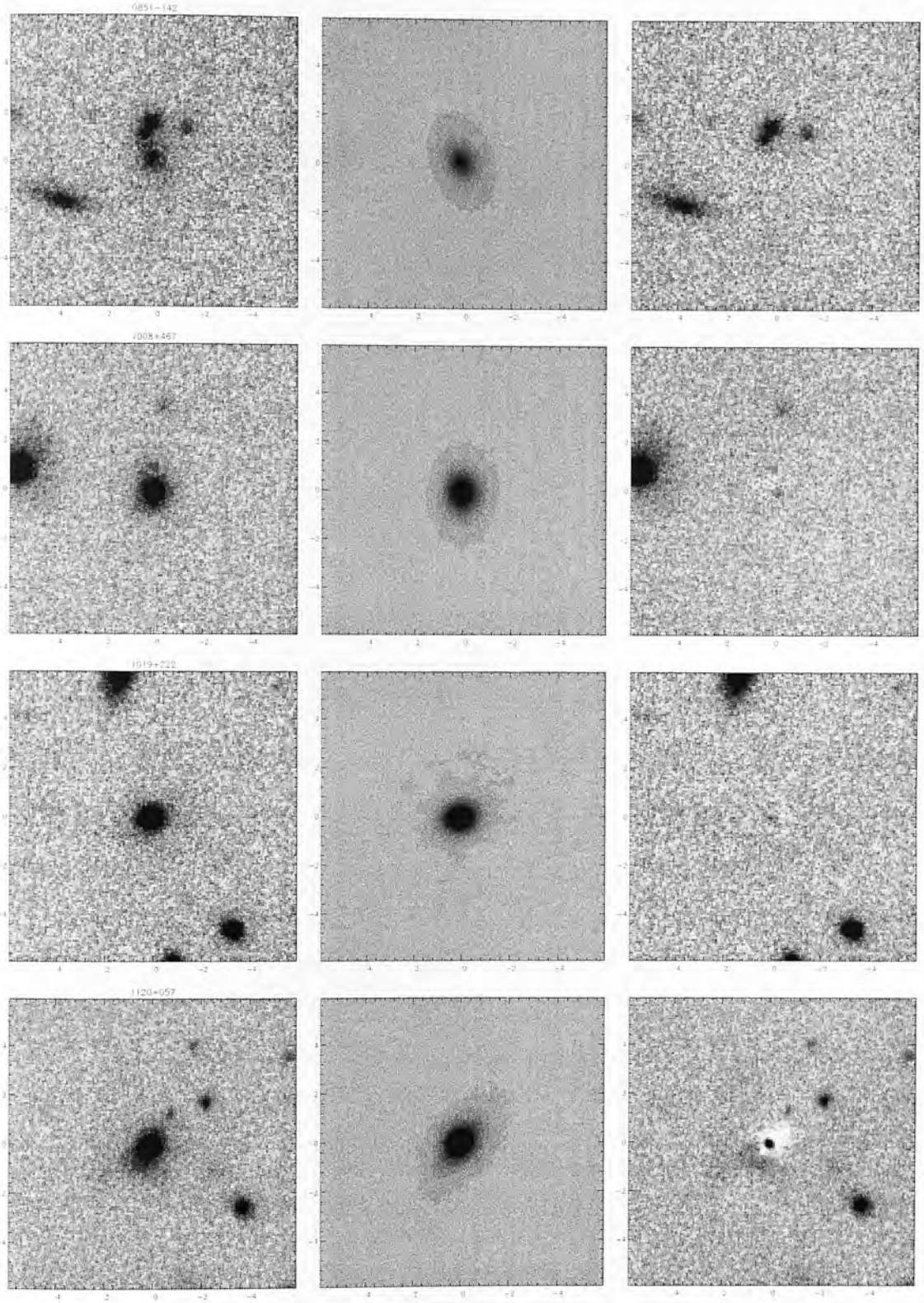

Figure 2.1: - continued

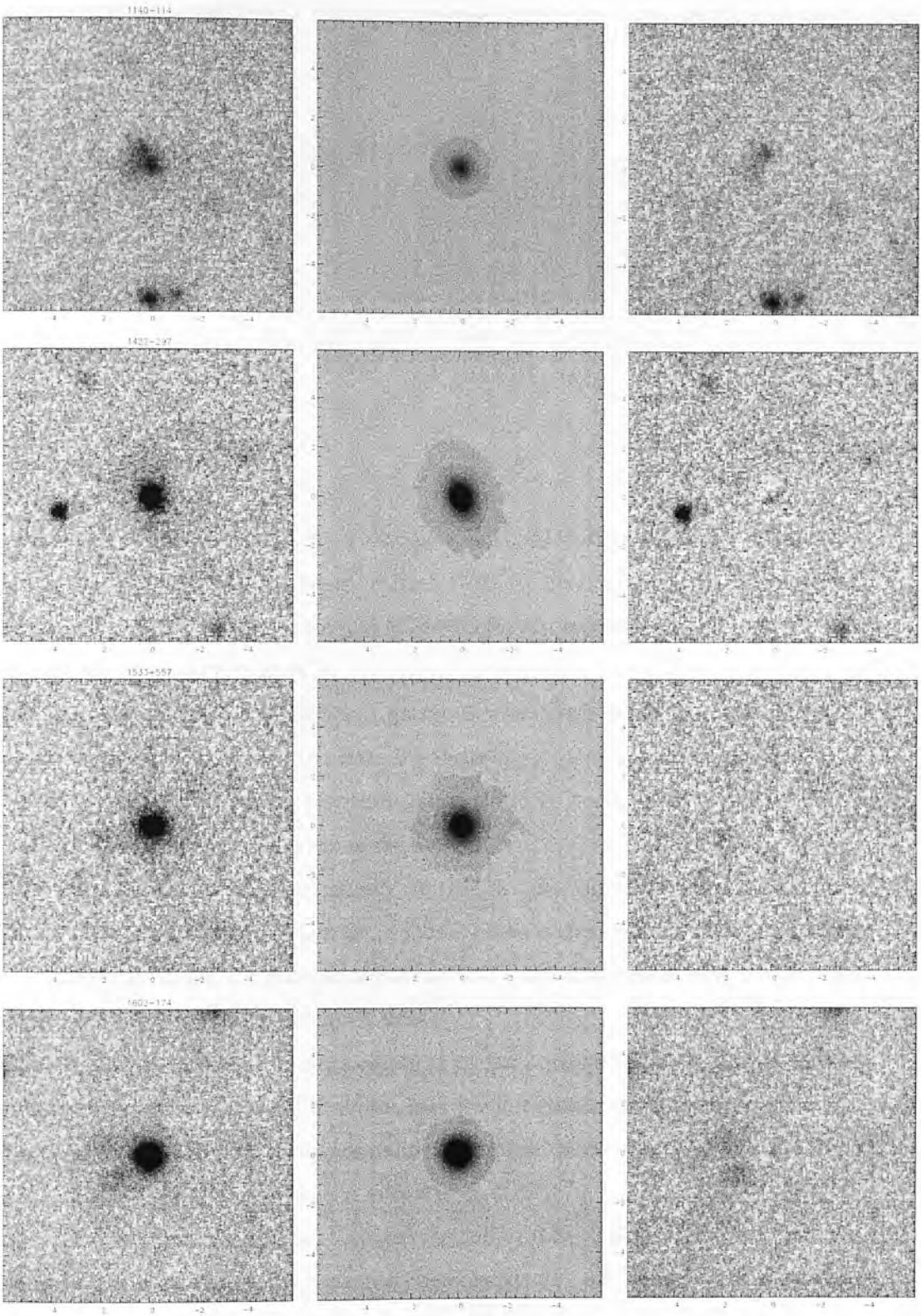

Figure 2.1: - continued

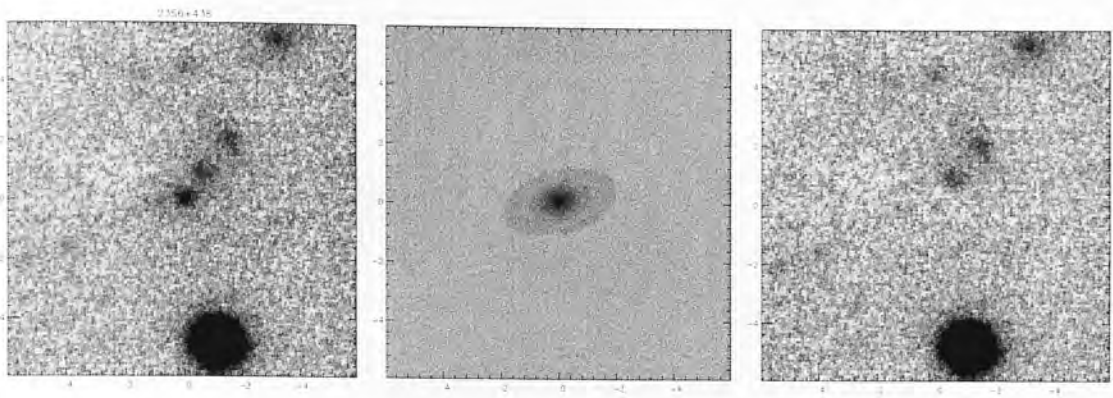

Figure 2.1: - continued

2.4.1 Source notes

Source identifications for SCUBA galaxies were based upon 850 μm detections from Scott et al. (2002), 1.4 GHz imaging from IV02, $I-$band HST ACS imaging from Almaini et al. (2005), and the 1200-μm MAMBO survey. Non-detections and unusable data are shown in Appendix A.1.

0016−12 A large extended elliptical galaxy is coincident with the radio position. Merger activity is suggested between the radio host and a small companion $\sim$ 1.1 arcsec north-east and a large elliptical galaxy 3 arcsec north-east. A diffuse tail of extended emission stretches north of the merger.

0128−26 A disturbed elliptical galaxy surrounded by significant levels of diffuse emission is situated between two radio lobes. There is clear merger activity between irregular companions $\sim$ 1.7 arcsec north-east and $\sim$ 2.8 arcsec south-west, with other potential companion objects within 5 arcsec.

0231+31 This radio host is a large elliptical galaxy surrounded by diffuse extended emission. There is evidence for a late-stage merger with a faint object $\sim$ 1.8 arcsec north-east. The position corresponds to faint radio detections, misaligned with a radio-lobe to the south-east, as seen in Best et al. (1997).

0310−15 A relatively compact galaxy surrounded by diffuse emission coincident with the radio position. A faint companion object located $\sim$ 2.5 arcsec north-east could indicate merger activity.

0851−14 An ambiguous identification from radio data is made for this source in Best

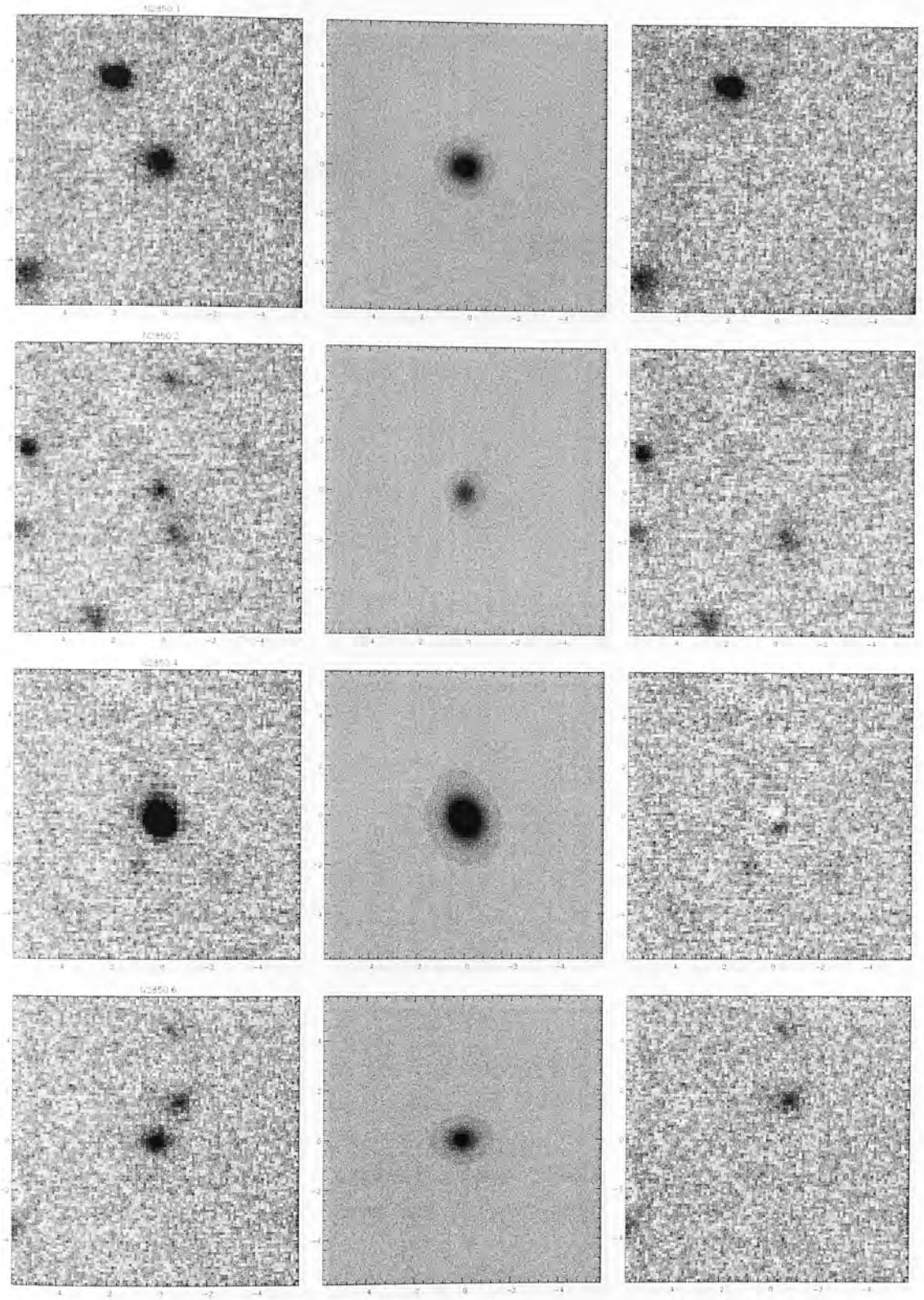

Figure 2.2: Two-dimensional modelling of the SCUBA galaxy imaging. The left-hand panel shows the reduced $K-$band image centred on the radio host. The middle panel shows the best-fitting two-dimensional model. The right-hand panel shows the residual image after subtraction of model from the science data. All panels are 12.0″×12.0″. Images are displayed at 2.5σ above and 1σ below the median sky value.

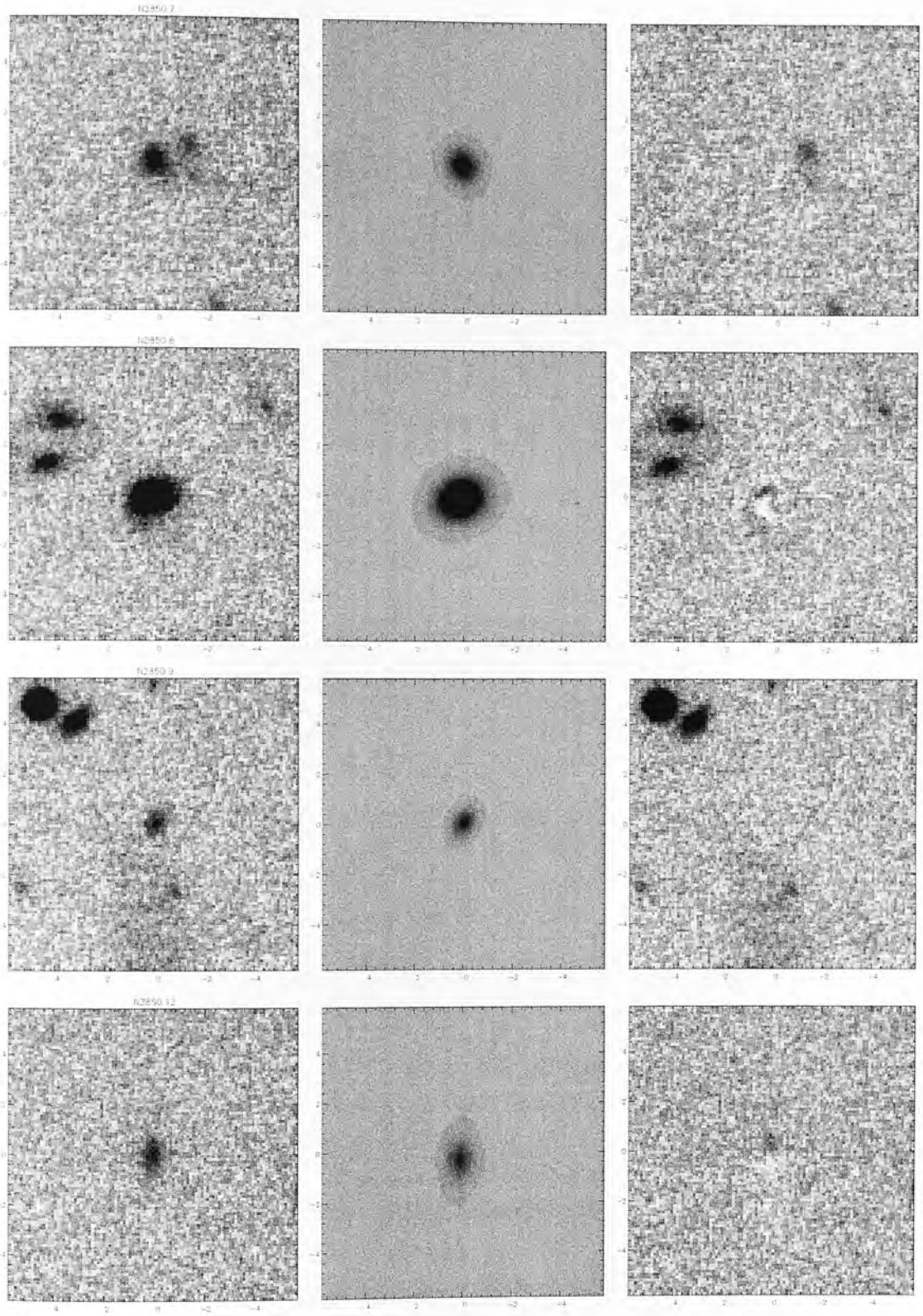

Figure 2.2: - continued

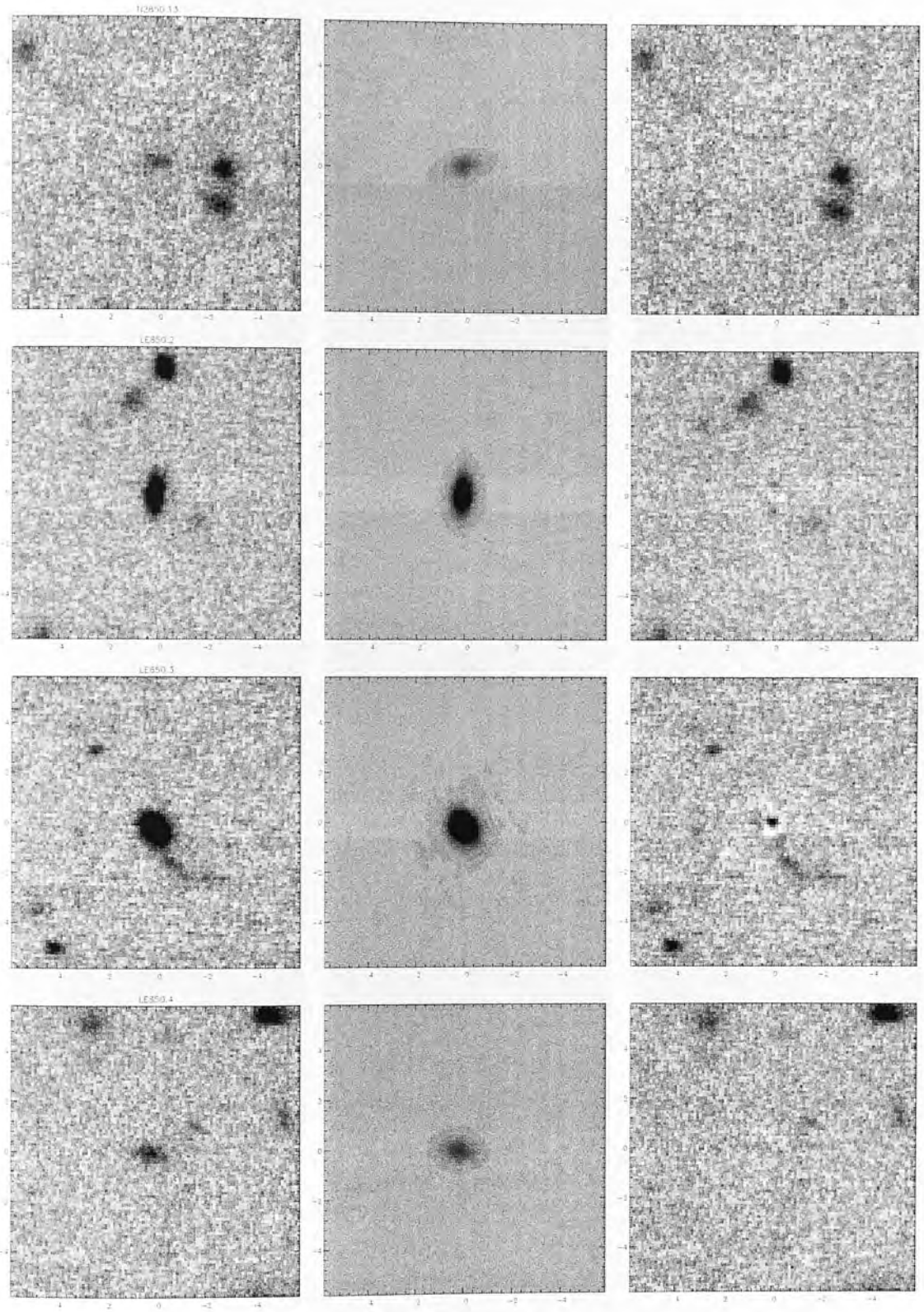

Figure 2.2: - continued

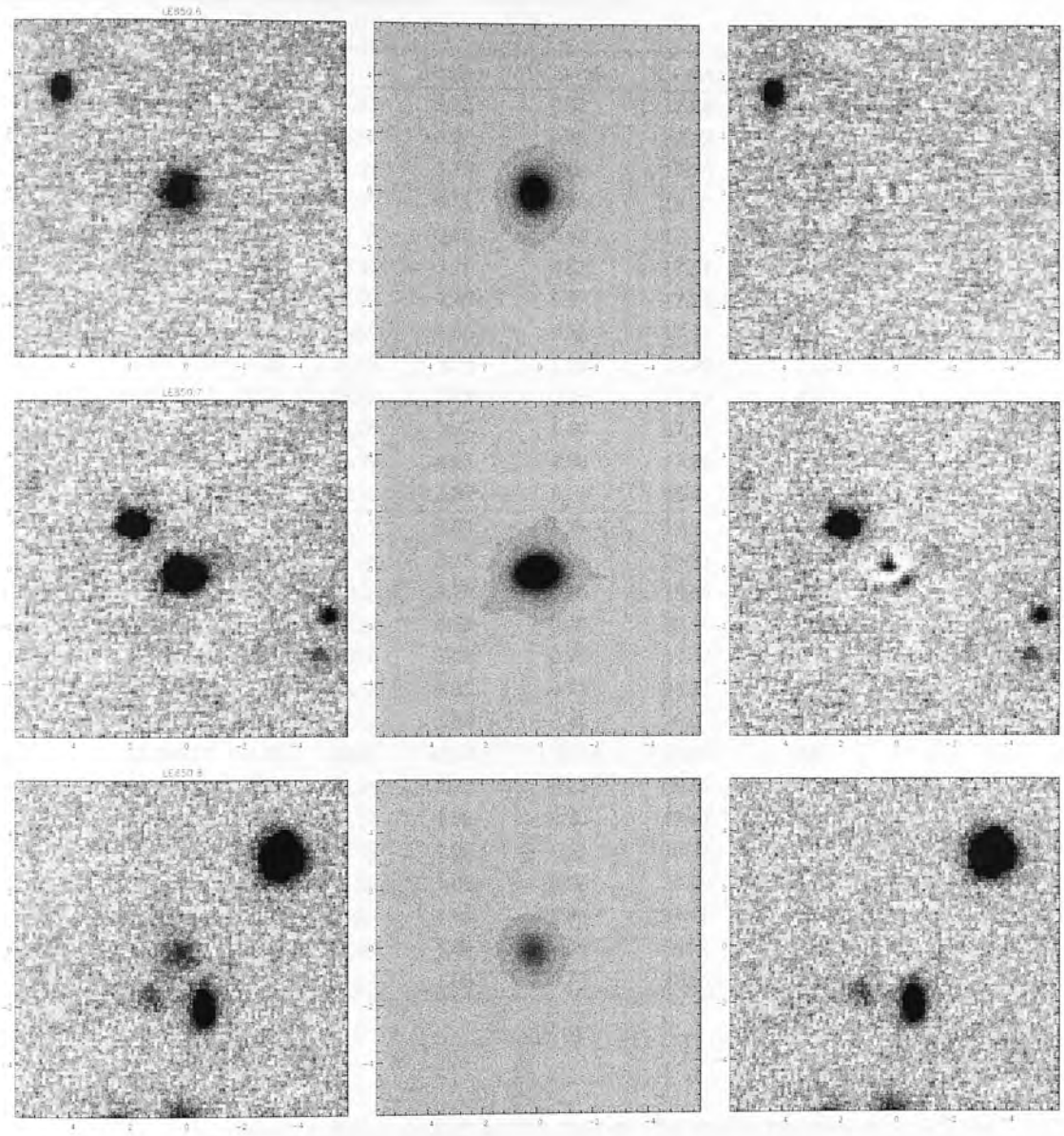

Figure 2.2: - continued

Table 2.2: Results from two-dimensional modelling. Column 2 lists the semi-major axis scale-length of the host galaxy fit in kiloparsecs. Column 3 lists the mean surface brightness in $K-$magnitudes per square arcsec. Column 4 lists the value of the Sérsic index (n). Column 5 lists the axial ratio of the host galaxy. Column 6 lists the total host-integrated $K-$band magnitude in Vega. Column 7 lists the reduced χ^2 of the model fit.

Source	$r_{1/2}$	$< \mu_e >$	Sérsic n	Axial ratio	$K-$mag	Reduced χ^2
0016−129	7.57	19.03	5.23	0.52	17.84	1.01
0128−264	15.66	20.64	3.28	0.45	17.37	0.94
0231+313	11.53	19.49	2.73	0.69	17.70	0.95
0310−150	7.75	19.51	4.51	0.33	18.07	0.82
0851−142	9.72	19.78	3.85	0.68	18.19	0.80
1008+467	4.24	17.44	3.76	0.85	17.81	0.94
1019+222	3.05	17.09	4.48	0.59	17.72	0.99
1120+057	11.85	16.69	6.26	0.42	17.44	1.14
1140−114	4.20	19.39	3.05	1.00	18.90	1.02
1422−297	9.29	19.16	5.74	0.45	17.40	0.97
1533+557	2.28	16.78	3.92	1.00	17.82	0.93
1602−174	0.90	14.99	4.67	0.88	17.84	0.88
2356+438	11.02	20.11	3.87	0.71	18.47	0.99
N2 850.1	2.09	18.61	1.74	0.76	19.77	0.99
N2 850.2	1.15	17.78	3.33	0.47	20.83	1.06
N2 850.4	3.24	18.2	1.79	0.66	18.65	0.85
N2 850.6	1.95	18.14	3.29	0.37	20.19	0.90
N2 850.7	2.77	19.16	1.08	0.75	19.67	0.72
N2 850.8	3.70	18.09	1.35	0.72	18.21	0.79
N2 850.9	3.05	19.74	1.08	0.41	20.65	0.79
N2 850.12	4.65	19.11	2.17	0.20	20.06	0.93
N2 850.13	5.78	20.34	2.75	0.22	20.76	0.79
LE 850.2	3.88	18.24	1.00	0.20	19.48	0.82
LE 850.3	2.56	17.53	1.00	0.53	18.75	0.58
LE 850.4	2.87	18.76	1.00	0.20	20.49	0.96
LE 850.6	3.60	19.3	1.99	0.89	19.16	0.90
LE 850.7	2.82	17.89	1.00	0.55	18.71	0.80
LE 850.8	3.10	20.04	1.00	0.75	20.16	0.72

et al. (1999), who select a disky object to the east of the radio position as seen in R-band imaging. Our deep K-band data reveals a multi-component merging system closer to the radio coordinate, composed of several disturbed objects with diffuse emission stretching south. The larger (southernmost) component of this merger was identified as the radio galaxy.

1008+46 This large elliptical galaxy is located between two radio lobes. A small

companion ~ 1 arcsec to the north suggests a late-stage merger.

1019+22 This large elliptical galaxy incident with radio position is surrounded by diffuse emission. Although no clear companions are visible, multiple faint sources are distributed around the galaxy.

1120+05 3C257 is the highest redshift radio galaxy in the 3C catalogue. A distorted elliptical galaxy with companion objects located to the north-west indicates recent merger activity. Inspection of the galaxy reveals an obscured point-like nucleus, clearly shown in the two-dimensional modelling residual.

1140−11 Evidence of a merger is indicated by a faint galaxy to the north-east merging into the primary disturbed source. The two $K-$band sources correspond to two radio detections. Extended emission surrounds the source and concentrates between the host and companion and to the south-east.

1404+34 Although clearly discernible, the target is obscured by a saturated star to the west. Host-galaxy analysis is impossible due to flat-fielding errors around the star and the large saturation line stretching close to the radio galaxy.

1422−29 This large elliptical galaxy has faint irregularities in its morphology. Significant diffuse emission surrounds the source, with concentrations to the south and a possible remnant of a faint companion.

1533+55 Strong extended emission surrounds this bright galaxy. A probable companion is found ~ 2 arcsec to the east.

1602−17 The counterpart to the radio data coincides with a radio core between two lobes. Host morphology is distorted by apparent nuclear activity, and two protrusions stretch to the east and south-east. $R-$band imaging from Best et al. (1999) presents a distinctly different morphology, with no sign of the active nucleus, suggesting obscured AGN emission. The point-like nature is also indicated by collapse of the half-light radius in the two-dimensional model.

2356+43 Several small galaxies linked by extended emission are the most likely counterpart to the radio data. The southernmost is the largest and shows evidence of interaction with the other two.

N2 850.01 A compact galaxy is aligned with the brighter of a close pair of radio sources associated with the submm emission (the brightest in the Elais N2 field).

Although this is a clear IR identification, some controversy surrounds the redshift estimate. Chapman et al. (2003) claim $z = 0.840$, although this is unconfirmed with CO. Recent estimates from Aretxaga et al. (2005) suggest a higher redshift of $z = 2.85$, adopted in this paper. The morphology appears to be a face-on spiral, although some distortion leads to ambiguity in this assessment.

N2 850.02 This submm source is associated with a close pair of compact galaxies, both highlighted by IV02 as hosts. The northerly object is incident with the radio emission and presents a far smaller $I - K$ colour, and hence the likely source of submm emission. The morphology of this object is unclear, although partial overlap of extended emission between the two objects suggests some interaction.

N2 850.03 No clear radio detection or $K-$band galaxy could be seen near to the submm position, although the source is confirmed in MAMBO, suggesting that the host could be at high redshift. Numerous compact sources surround the submm position in the $I-$band data, although there is no clear counterpart. The host was taken to be the object closest to the faint radio detection with the lowest $I - K$ colour. No clear morphology is discernible in the $K-$band data.

N2 850.04 A clear radio detection is incident with a large elliptical host. One of the largest of the submm hosts, the source does not appear extended, although some diffuse emission stretches away to the north and south-west in what could be evidence of merger activity. The $I-$band imaging reveals a clearly disturbed multi-component morphology.

N2 850.05 This submm source is not detected in the K or $I-$band imaging, the radio data from IV02, or the 1200-μm MAMBO survey. The $K-$band image is centred on the submm position.

N2 850.06 A pair of galaxies close to the submm position is identified without radio emission in IV02. The southerly object of the pair is classified as an extremely red object ($I - K = 4.1$) and is larger in both the K and $I-$band data. No clear morphology is visible, although the source is surrounded by diffuse emission.

N2 850.07 The largest of several galaxies showing evidence of recent interaction is incident with a radio detection. $I-$band imaging reveals a clearly disturbed galaxy with several distinct components.

N2 850.08 A bright $K-$band galaxy is associated with the radio and submm positions. The host seems to be a face-on spiral, with asymmetries and faint tidal trails suggesting a merging system. The $I-$band data clearly shows a late-stage merger.

N2 850.09 IV02 find a large low-surface-brightness (LSB) galaxy surrounding their radio detection. Although this object is seen in both the K and $I-$band data, it appears to comprise numerous small sub-clumps and is not a clear counterpart to the submm data. The faint ERO to the north-west of this LSB galaxy was adopted as the submm host, which coincides with a second faint radio position.

N2 850.10 No clear radio, $K-$band, or $I-$band counterpart is found for this source. The object highlighted in IV02 appears to be stellar in nature under two-dimensional modelling and in the $I-$band data. The $K-$band image is centred on a faint potential counterpart close to the submm position.

N2 850.11 This submm source is not detected in the K or $I-$band imaging or the radio data. The area around the submm position is devoid of any potential counterparts. The $K-$band image is centred on a bright radio detection $\sim$ 14 arcsec south-west, although this is an unlikely submm host.

N2 850.12 No clear radio source is association with the submm position. The identification was made from $I - K$ colours and matches IV02. An elongated very red object was found, which appears irregular in the $I-$band data.

N2 850.13 A faint galaxy is associated with the given radio position. Faint extended emission was found around the source, suggesting interaction with a pair of galaxies to the west.

N2 850.14 No radio or plausible $K-$band counterpart is found for this source.

LE 850.01 A diffuse unresolved galaxy incident with the radio position was found. Extended emission stretches south-east to a bright peak at the radio position.

LE 850.02 A large edge-on spiral galaxy is coincident with the fainter of two radio detections in close proximity to the submm position. Overlap in extended emission with a small potential companion object $\sim$ 2 arcsec to the south-east suggests interaction between the two.

LE 850.03 The radio position falls on a large late-stage merger with a bright tidal tail stretching to the south-west. The galaxy is asymmetrical with a bright core and

limited extended emission.

LE 850.04 In the absence of a strong radio identification, we have selected a galaxy in close proximity to the submm position, showing evidence of interaction with a small companion object to the north-west.

LE 850.05 This submm source is not detected in the K or $I-$band imaging or radio data. The $K-$band image is centred on the submm position.

LE 850.06 A late-stage merger system is indicated by a tidal tail stretching to the south-east.

LE 850.07 A large host galaxy matching the radio position is found, surrounded by extended emission.

LE 850.08 The system is composed of 3 apparently interacting objects. Although the larger galaxy to the south-west would seem a likely host, the radio data indicates the fainter object to the north-east is the source of submm emission.

LE 850.09 A non-detection in the $K-$band imaging; the apparent source seen close to the submm position in the $K-$band data is a residual from a saturated star near the target.

LE 850.15 This submm source is not clearly detected in the $K-$band or radio data. The $K-$band image is centred on the submm position.

LE 850.17 This submm source is not clearly detected in the $K-$band or radio data. The $K-$band image is centred on a faint potential counterpart close to the submm position.

2.5 Results

2.5.1 Two-dimensional modelling

A clear separation is found in the sizes and luminosity profiles of these two classes of active galaxy, as seen in Table 2.2. The high-redshift radio galaxies emerge as large relaxed ellipticals, while the SCUBA sources are massive disks. A comparison of the Sérsic indices is presented in Figure 2.3. Submm galaxies with reliable modelling results possess Sérsic values peaked at $n = 1$ in the range $1 < n < 2.5$. It should be noted that the two-dimensional modelling code is restricted to Sérsic values of $n > 1$. Source modelling without the lower n limit finds values consistent with ~ 1. The Sérsic indices of the radio galaxies are in the range $2.5 < n < 5.75$ and peaked around $n = 4$, corresponding with a de Vaucouleurs profile. The distribution of half-light radii is seen in Figure 2.4. Submm sources are clearly peaked around $r_{1/2} \sim 3\,\mathrm{kpc}$, while the radio galaxies are spread over a large range with an average $r_{1/2} = 8\,\mathrm{kpc}$. These results are placed in context with galaxies at similar redshifts in Section 2.6.1.

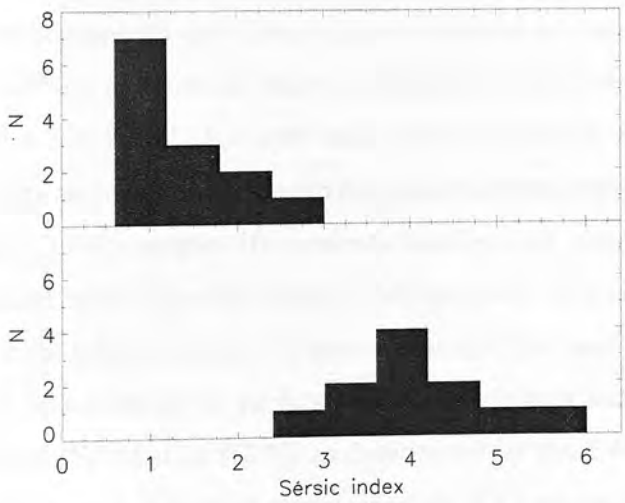

Figure 2.3: Histogram of Sérsic n for submm galaxies (above) and radio hosts (below) from two-dimensional modelling.

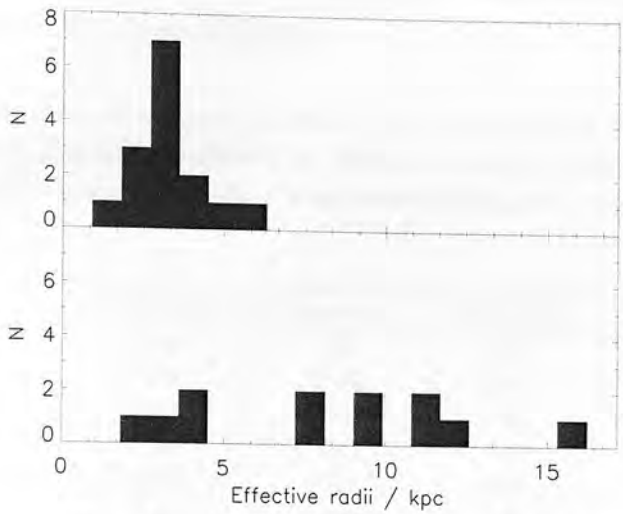

Figure 2.4: Histogram of $r_{1/2}$ for submm galaxies (above) and radio hosts (below) from two-dimensional modelling.

2.5.2 Verification of modelling results

Modelling of simulated data

The accuracy of scalelength and Sérsic index recovery was examined via two-dimensional modelling of synthetic galaxies. Model galaxies were constructed with $r_{1/2}$ of 1, 1.5, 2, 3, 4, 5, 6, 7, and 8 kpc with Sérsic values of 1 and 4. The Axial ratio and position angle were set to be constant, with luminosity and redshift set from the mean values of the radio galaxy sample. The synthetic sources were inserted into an image, with noise levels set based upon the average RMS-per-pixel values derived from photometry of the radio galaxy sample. To ensure that all PSFs used during modelling were sufficiently well matched to the hosts, the synthetic data were convolved with the poorest quality PSF (that of 3C239) as determined by the FWHM. Background counts were added to each simulated model using the IRAF routine MKNOISE. Using the science frame for 3C239, a new PSF was constructed using an alternate selection of stars on the field. These 18 synthetic galaxies were modelled using the alternate PSF, the results of which are shown in Tables 2.3 and 2.4. It was found that the two-dimensional modelling accurately recovers the scalelength of all simulated sources.

Sérsic parameters are recovered where $r_{1/2} > 2\,\mathrm{kpc}$, below which galaxies simulated to be ellipticals and disks appear similar.

Table 2.3: Results of two-dimensional modelling tests using synthetic disk galaxies ($n = 1$). Column 1 lists the actual scalelengths of the simulated sources. Columns 2 and 3 list the recovered scalelengths and Sérsic indices from the modelling code. $r_{1/2}$ values are given in parsecs.

Simulated $r_{1/2}$	Recovered $r_{1/2}$	Recovered n
1000	770	1.32
1500	1246	1.99
2000	1966	1.65
3000	3156	1.12
4000	4781	1.05
5000	5246	1.02
6000	6375	1.02
7000	7580	1.03
8000	8238	1.00
9000	9238	1.00
10000	10292	1.00

Table 2.4: Results of two-dimensional modelling tests using synthetic elliptical galaxies ($n = 4$). Column 1 lists the actual scalelengths of the simulated sources. Columns 2 and 3 list the recovered scalelengths and Sérsic indices from the modelling code. $r_{1/2}$ values are given in parsecs.

Simulated $r_{1/2}$	Recovered $r_{1/2}$	Recovered n
1000	876	2.46
1500	1703	3.54
2000	2122	3.71
3000	3747	3.65
4000	4551	2.68
5000	5279	3.28
6000	5693	3.10
7000	6658	3.27
8000	7998	3.59
9000	9066	3.85
10000	10022	3.26

As seen in Table 2.2 all submm hosts, with the exception of N2 850.2 and N2 850.6, possess Sérsic values consistent with disk-like morphologies. The scalelengths of these two outliers are comparable to the $\sim$ 2 kpc recovery limit, implying that these high Sérsic parameters are an artifact of the modelling and not source morphology. This revision reinforces the conclusion that the radio galaxies are ellipticals, while submm hosts are disk-like.

These results demonstrate that the UKIRT radio galaxy data is of sufficient quality to recover host-galaxy morphologies using two-dimensional modelling. However, although the submm galaxy Gemini data are typically deeper, the signal-to-noise ratio is typically lower given the faint nature of the sources. Recovery of similar simulated data with noise levels set to those of the Gemini data would confirm the results derived from the two-dimensional modelling.

Non-parametric tests of $r_{1/2}$

The Petrosian radius and $r_{1/2}$ were determined from a curve-of-growth analysis for comparison with the modelling results. These data are shown in Table 2.5. Surface-brightness profiles for each object were plotted using data obtained with the IRAF package PHOT, measuring progressively larger apertures out to a radius of 12 arcsec. Upon determining the extent of the total flux from the source, the $r_{1/2}$ was read from the profile. The Petrosian radius was defined as described by Blanton et al. (2001) and Yasuda et al. (2001), taken to be the point at which the ratio of the surface brightness in an annulus at radius r to the mean surface within an aperture of radius r equals 0.2. The $r_{1/2}$ from two-dimensional modelling, curve-of-growth, and Petrosian technique are generally consistent while the scalelengths of the sources are greater than those of the PSFs, typically corresponding to $\sim$ 4 kpc. As the two-dimensional model deconvolves the PSF from the data before modelling, the code was able to fit scalelengths smaller than the PSF-limited curve-of-growth or Petrosian techniques.

Table 2.5: Comparison of half-light radius estimates. Column 1 lists the source name. Columns 2, 3, and 4 list the half-light radii in kpc derived via two-dimensional modelling, curve-of-growth analysis, and the Petrosian radius respectively.

Source	$r_{1/2}$ model	$r_{1/2}$ growth	$r_{1/2}$ Petrosian
0016−129	7.57	6.51	6.13
0128−264	15.66	11.36	11.71
0231+313	11.53	7.03	9.61
0310−150	7.75	9.24	8.07
0851−142	9.72	10.84	9.92
1008+467	4.24	6.00	6.25
1019+222	3.05	5.30	6.05
1120+057	11.85	5.73	6.88
1140−114	4.20	6.10	6.38
1422−297	9.29	7.04	9.28
1533+557	2.28	7.00	7.26
1602−174	0.90	6.11	6.59
2356+438	11.02	12.79	14.18
N2 850.1	2.09	4.27	4.98
N2 850.2	1.15	4.35	4.31
N2 850.4	3.24	4.70	4.57
N2 850.6	1.95	4.50	5.68
N2 850.7	2.77	3.92	3.86
N2 850.8	3.70	4.87	5.25
N2 850.9	3.05	3.11	3.13
N2 850.12	4.65	5.20	5.20
N2 850.13	5.78	4.48	4.32
LE 850.2	3.88	3.89	4.04
LE 850.3	2.56	3.67	3.93
LE 850.4	2.87	4.14	4.23
LE 850.6	3.60	5.40	4.56
LE 850.7	2.82	4.15	4.12
LE 850.8	3.10	4.82	4.00

Non-parametric tests of Sérsic index

The distribution of the axial ratios and concentration indices for the two samples are plotted as a model-independent test of host morphology. The axial ratios are plotted in Figure 2.5. Although a Kolmogorov-Smirnov (KS) test does not find a significant difference between the two samples, it is interesting to note that four objects in the submm sample appear consistent with edge-on disks, contrasted with an absence of radio galaxies at this low value.

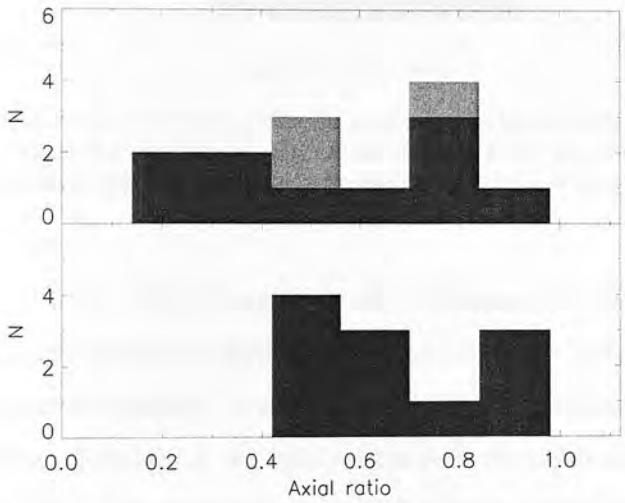

Figure 2.5: Distribution of axial ratios for submm galaxies (above) and radio galaxies (below) from two-dimensional modelling. The secure submm hosts are shown with dark grey shading, while unsecure identifications are indicated by light grey shading.

The distribution of source concentration index is shown in Figure 2.6. Concentration index represents the fraction of stars in the bulge component of a galaxy (Conselice 2003), and was calculated using Equation 2.1, where r_{80} and r_{20} are the radii containing 80 per cent and 20 per cent of the total light from the galaxy.

$$C = 5 \times \log(r_{80}/r_{20}) \tag{2.1}$$

The lower values of the submm sources are consistent with those expected for late-type galaxies, while the higher values for the radio galaxies suggest early-type

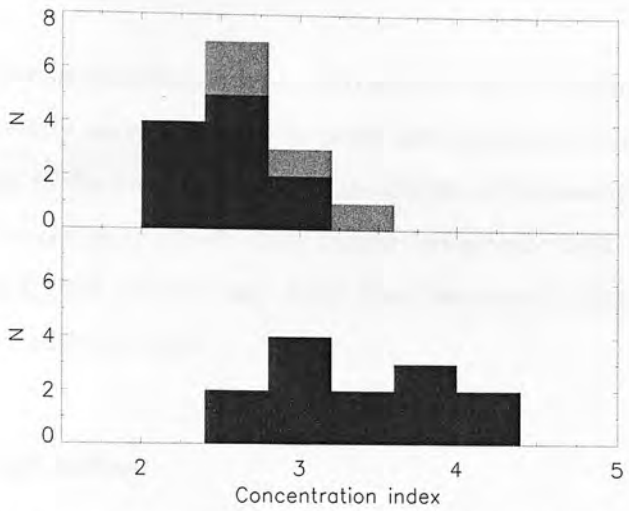

Figure 2.6: Distribution concentration index for submm galaxies (above) and radio hosts (below) from two-dimensional modelling. The secure submm hosts are shown with dark grey shading, while unsecure identifications are indicated by light grey shading.

hosts. A KS test finds a significant separation between the two samples, with a $P = 0.01$ that the two are drawn from the same distribution. It should be noted that constraining source morphology from concentration index typically requires higher-resolution data than that used in this study. However, the separation found between these two samples suggests a difference in morphology consistent with the modelling results. Of the five radio hosts with highest concentration indices, two (1120+057 and 1602−174) show evidence of unresolved nuclear activity, as noted in Section 2.4.1.

The ability of the two-dimensional modelling to recover accurate morphological information from simulated data, and the consistency of these results with multiple non-parametric tests of $r_{1/2}$ and Sérsic index, support the view of radio galaxies as relaxed ellipticals and submm hosts as massive disks.

2.6 Discussion

We compare the most luminous known radio galaxies at $z \sim 2$ to the brightest submm sources in the 8-mJy survey. It must be noted that whereas the radio galaxies are a complete sample of the most radio-luminous objects in the redshift range $1.5 < z < 2.5$, the submm sources are drawn solely from a 260-arcmin^2 field. Consequently, the nature of these SCUBA galaxies may differ from the most luminous submm objects detected in subsequent surveys.

2.6.1 Half-light radius

A comparison of $r_{1/2}$ with redshift for the samples is presented in Figure 2.7. The $z \sim 2$ radio galaxies are found to be, on average, a factor ~ 2 smaller than the $z < 1$ 3CRR radio galaxies from McLure et al (2004). The $z \sim 2$ radio hosts represent some of the most massive galaxies in place at $z \sim 2$, implying that they are the progenitors of the most massive galaxies at $z = 0$. It can be argued that passive evolution alone could account for the difference in $K-$band magnitude between the $z \sim 2$ and $z \sim 0$ radio galaxies, as indicated by the infrared Hubble diagram in Figure 2.13. This assessment would seem to be supported by the similarity of 3C-type radio galaxy scalelengths for $0 < z < 1$ sources. However, passive evolution alone cannot account for the approximate factor-of-two decrease found in $r_{1/2}$ of the $z \sim 2$ radio galaxies. By implication, the $z \sim 2$ radio galaxies would need to undergo major mergers to relax their $r_{1/2}$ to local values. Submm galaxies are found to be significantly smaller than the massive radio hosts at $z \sim 2$.

2.6.2 The Kormendy relation

Early-type galaxies are known to exist on a two-dimensional manifold (fundamental plane), defined by effective scalelength, mean surface brightness, and the central stellar velocity dispersion in three-dimensional parameter space (e.g. Dressler et al. 1987; Djorgovski & Davis 1987). The Kormendy or $\mu_e - r_e$ relation (Kormendy 1977) allows

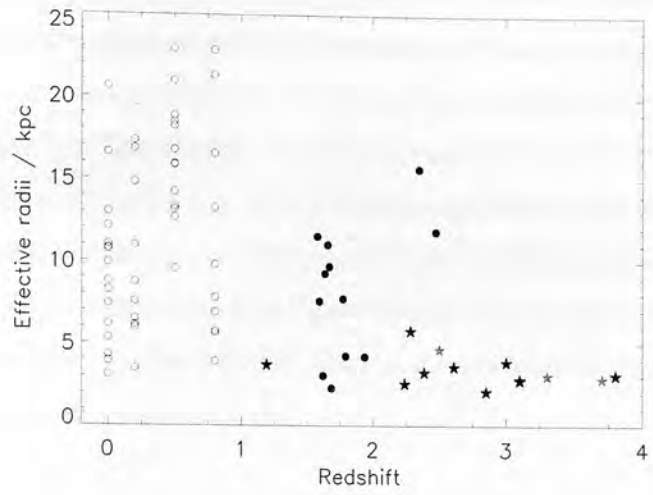

Figure 2.7: Distribution of $r_{1/2}$ with redshift for low-redshift 3C galaxies (open circles) from McLure et al. (2004), $z \sim 2$ radio galaxies (filled circles), and submm sources (filled stars). The secure submm hosts are shown with dark grey shading, while unsecure identifications are indicated by light grey shading.

examination of the photometric projection of the fundamental plane using only the scalelength and surface-brightness parameters.

The $R-$band Kormendy relation for the $z \sim 2$ radio galaxies and $z = 0$ 3C-type galaxies from McLure et al. (2004) is shown in the top panel of Figure 2.8. The $< \mu >_e$ values of the $z \sim 2$ radio galaxy samples have been K corrected, corrected for $(1 + z)^4$ surface-brightness dimming, and converted into the $R-$band. The sources in the McLure et al. sample have also been corrected for passive evolution with Bruzual & Charlot (2003) galaxy-evolution models. Using the MPFITFUN least-squares routine, the best-fitting form of the Kormendy relation for the non-evolutionary corrected $z \sim 2$ radio galaxy sample is

$$< \mu >_e = 3.96(\pm 1.19) \log r_e + 14.39(\pm 1.03) \quad (2.2)$$

Given that the galaxies in the McLure et al. Kormendy fit are at $z = 0$, or evolutionary-corrected to that redshift, the vertical offset between the two populations is a direct indication of the amount of luminosity evolution between $z = 0$ and

$z \sim 2$. If the two samples are fitted with a Kormendy relation of fixed slope 3.87 (intermediate of their two independent fits), then the best-fitting intercepts are 14.46 and 16.22 for the $z \sim 2$ radio galaxies and 3C-type galaxies respectively (as seen in the top panel of Figure 2.8). This directly implies 1.76 magnitudes of $R-$band luminosity evolution between $z \sim 2$ and $z = 0$. This is in good agreement with the evolutionary correction derived from the $z_{form} = 3$ Bruzual & Charlot (2003) models for a passively evolving galaxy. In the central panel of Figure 2.8 the 3C-type galaxies from McLure et al. are again plotted, together with the now $z_{form} = 3$ evolutionary-corrected $z \sim 2$ radio galaxy sample which has the form

$$< \mu >_e = 3.74(\pm 0.44) \log r_e + 16.38(\pm 0.47) \tag{2.3}$$

This result suggests that a galaxy formed in a burst at $z = 3$ could passively evolve to reproduce the observed Kormendy relation for these 3C galaxies. The average redshift of the submm sources is $\simeq 2.77$. As the submm galaxies exhibit the 1000 solar-masses/yr star-formation rate necessary to assemble massive galaxies within 1 Gyr, it is possible that they represent the progenitors of today's massive ellipticals.

The $K-$band Kormendy relation for the submm sources and $z \sim 2$ radio galaxies normalised to $z = 2$ using a $3/(1+z)^3$ surface-brightness dimming correction is plotted in the bottom panel of Figure 2.8. Neither has been corrected for passive evolution. Using the MPFITFUN routine, the best-fitting form of the Kormendy relation for these galaxies is

$$< \mu >_e = 3.97(\pm 0.83) \log r_e + 16.04(\pm 0.59) \tag{2.4}$$

This is in general agreement with the radio galaxy Kormendy relation, suggesting that despite the apparent morphological difference, the two classes of active galaxy could be related.

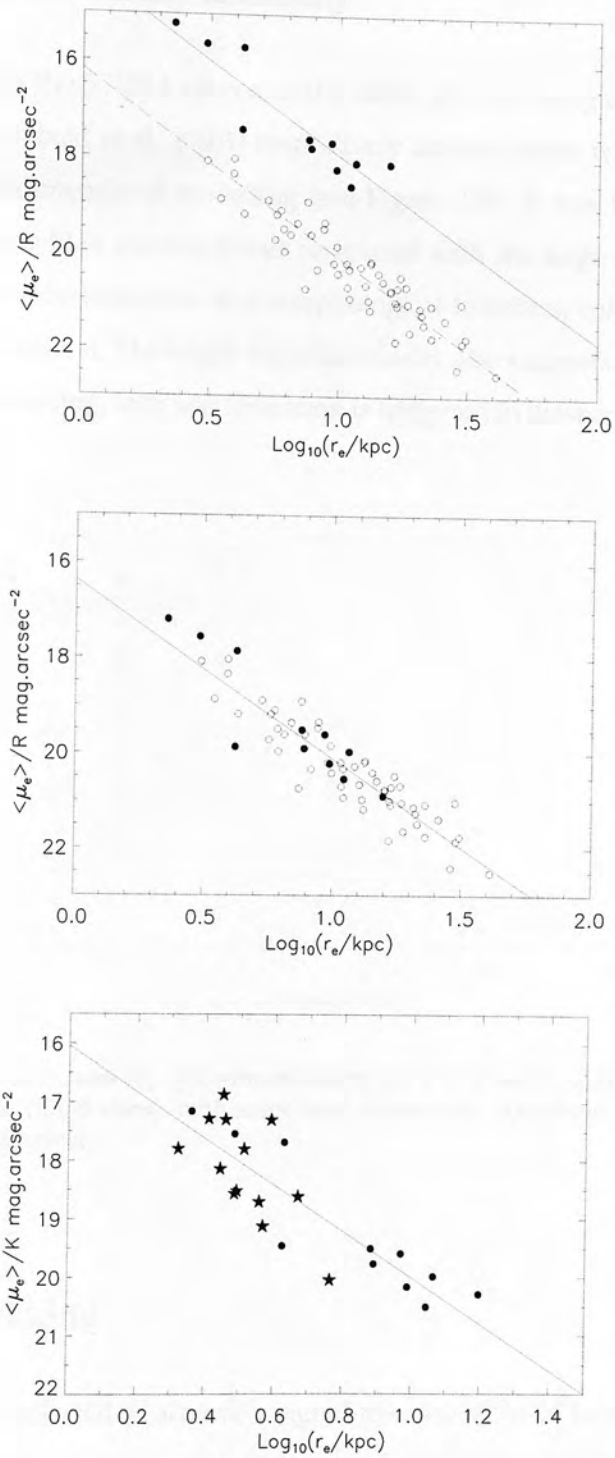

Figure 2.8: The top panel shows the best-fitting fixed-slope Kormendy relations for the $z \sim 2$ radio galaxy sample (solid line) and the $z = 0$ 3C-type galaxies from McLure et al. (2004) (dashed line). In the centre panel the $z \sim 2$ radio galaxies have been corrected for passive evolution of their stellar populations as described in the text. The bottom panel shows the best-fitting Kormendy relation to the $z \sim 2$ radio galaxies and submm galaxies corrected for $z = 2$ and without evolutionary corrections.

2.6.3 Sérsic index vs submm luminosity

Submm fluxes from the SCUBA sources and 4 radio galaxies using data from Scott et al. (2002) and Archibald et al. (2001) respectively are compared with Sérsic indices derived from two-dimensional modelling (see Figure 2.9). It was found that disky submm objects have high submm fluxes compared with the large spheroidal radio galaxies. This could be indicative of a morphological transition coinciding with the end of a massive starburst. The bright radio luminosity also suggests that despite substantial black hole feeding, little star formation is triggered in these massive ellipticals as a result.

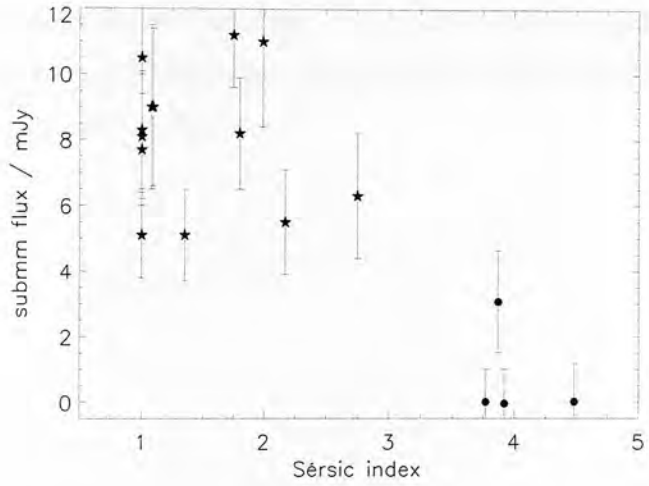

Figure 2.9: Plot of Sérsic index against submm fluxes for $z \sim 2$ radio galaxies (filled circles) and the submm hosts (filled stars), with associated errors from Archibald et al. (2001) and Scott et al. (2002) respectively.

2.7 Image stacking

The exposure times selected to achieve a signal-to-noise of 5σ at twice the expected 10 kpc scalelength allow accurate two-dimensional modelling of galaxy profiles. To exclude the possibility that extended emission could have been lost to noise, the data for both source types were stacked to create images with effective exposure times of 33.5 hours (on UKIRT) for the radio galaxies and 21.7 hours (on Gemini) for the

SCUBA sources (≡80 hours on UKIRT). All images were centroided, scaled to the average luminosity, aligned the same position angle, and mean-combined using the IRAF package IMCOMBINE. The resulting images were then modelled using PSFs created from a scaled stack of all individual PSFs, the results of which are presented in Figure 2.10 and Table 2.6.

The profiles of these two stacked images are seen in Figure 2.11. It is clear that there is a significant amount of extended emission around the radio galaxies out to a radius of ~ 5 arcsec, consistent with a large relaxed elliptical. In contrast, the profile of the submm galaxy stack confirms the compact nature of the source, with no signal detected beyond a radius of 2 arcsec. This clearly indicates that extended emission is not lost due to noise in the NIRI imaging. The results of the two-dimensional modelling are found in Table 2.6. These data are consistent with the average values of the individual objects included in the stack.

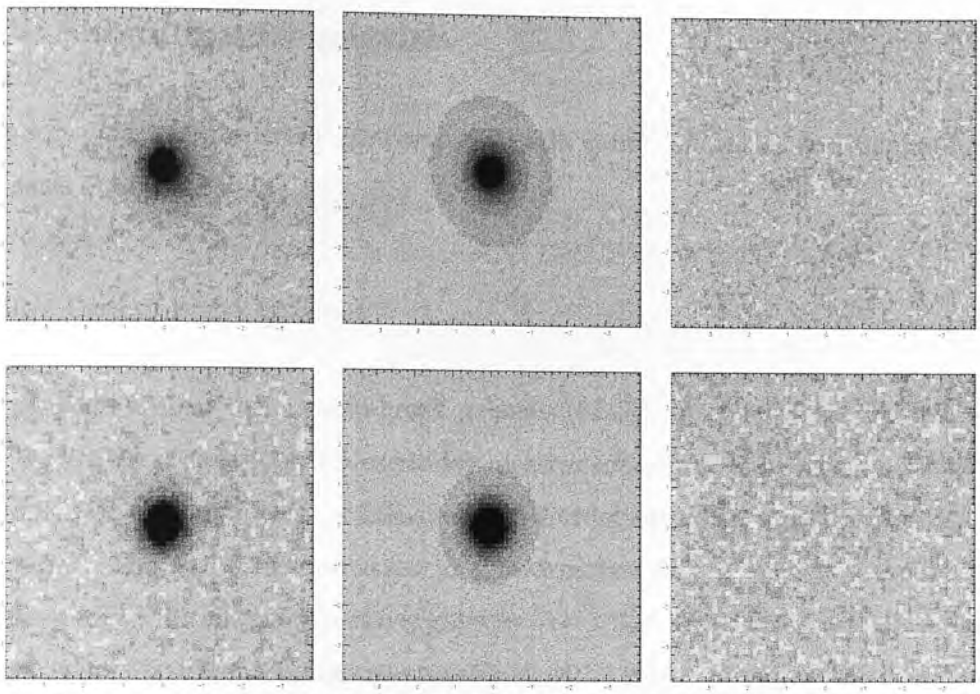

Figure 2.10: Two-dimensional modelling of stacked radio galaxies (above) and submm hosts SCUBA (below). The left-hand panels show the stacked image. The middle panels show the best-fitting models. The right-hand panels show the residual images produced by subtracting the best-fitting models from the stacked data. All panels are $8.0'' \times 8.0''$. Images are displayed at the average 2.5σ above and 1σ below for the stacked objects around the median sky value.

Table 2.6: Two-dimensional modelling results of stacked radio and SCUBA galaxies.

Source	$r_{1/2}$	$< \mu_e >$	Sérsic n	$K-$mag	reduced χ^2
Radio galaxy stack	6.12	19.18	4.6	17.88	.97
SCUBA galaxy stack	2.11	18.59	2.2	19.47	.94

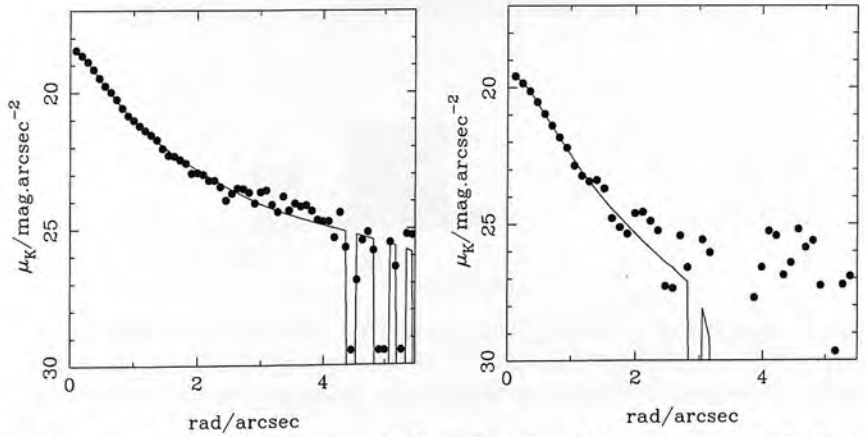

Figure 2.11: Luminosity profiles of stacked $z \sim 2$ radio (left) and submm galaxies (right).

2.8 Submillimetre galaxies

Submm galaxies' properties are compared with spiral, elliptical, and Lyman-break galaxies at high redshift.

2.8.1 Lyman-break galaxies

It has been argued that Lyman-break galaxies (LBGs), discovered by Steidel et al. (1999), are the progenitors of present-day massive spheroids. However, the relatively modest star-formation rates of LBGs fall 1 to 2 orders of magnitude short of this expectation. The $>$ 1000 solar-masses/yr star-formation rate of submm sources could account for the formation of massive galaxies in $\sim$ 1 Gyr. The distribution of $K-$band magnitudes for submm sources was compared with Lyman-break galaxies from Shapley et al. (2001), believed to represent normal field galaxies at $z \sim 3$. A clear separation between these two classes is found, with submm source on average 1.5 magnitudes brighter than the LBG population. This suggests that submm galaxies are significantly more massive than LBGs at $z \sim 3$.

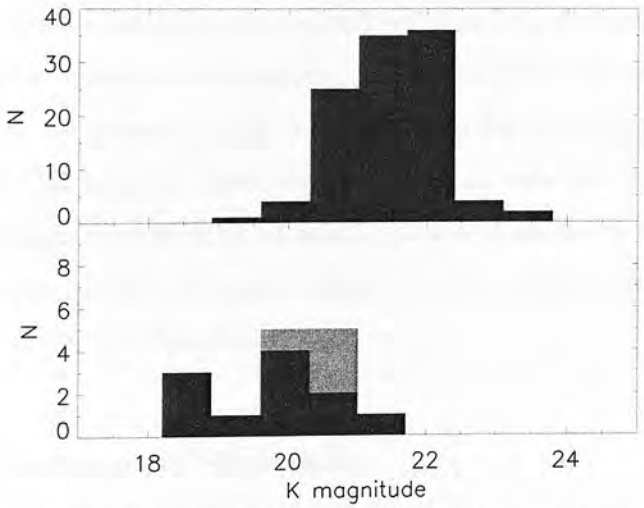

Figure 2.12: Magnitude distribution of Lyman-break galaxies (above) from Shapley et al. (2001) and submm galaxies (below) from two-dimensional modelling. The secure submm hosts are shown with dark grey shading, while unsecure identifications are indicated by light grey shading.

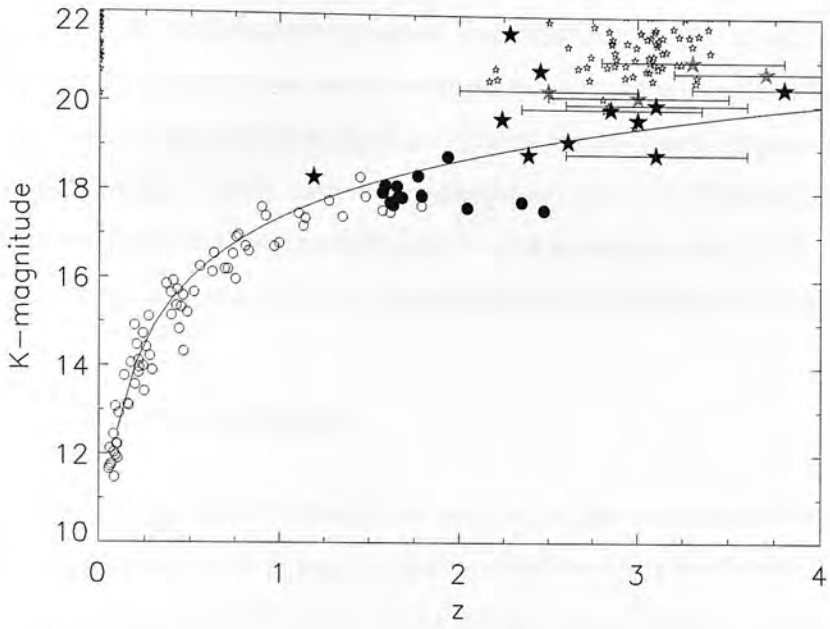

Figure 2.13: The infrared Hubble diagram for 3CRR radio galaxies (open circles) from Willott et al. (2003a), the $z \sim 2$ radio galaxies (filled circles), submm hosts (filled stars), and Lyman-break galaxies (open stars) from Shapley et al. (2001). The secure submm hosts are shown with dark grey shading, while unsecure identifications are indicated by light grey shading.

The infrared Hubble diagram ($K - z$ relation) for the radio galaxies, submm sources, and Lyman-break galaxies is plotted in Figure 2.13. It was found that the $z \sim 2$ radio galaxies are consistent with massive 3C galaxies from Willott et al. (2003a). The submm sources are generally more consistent with the formal best-fit to the 7CRS, 6CE, 6C and 3CRR samples from Willott et al. than with the fainter Lyman-break galaxies. A simple interpretation of submm source consistency with the Willott et al. fit is that the bright SCUBA galaxies could become massive ellipticals via passive evolution of their stellar populations.

2.8.2 Comparisons of half-light radii

A comparison of $r_{1/2}$ with redshift for the submm hosts to large spiral and elliptical galaxies at high redshift is presented in Figure 2.14. Submm hosts are found to be comparable in size to large disk-like galaxies at $1.4 < z < 3.0$ found in Labbé et al.

(2003) and the disk of old stars at $z \sim 2.5$ from Stockton et al. (2004). The ubiquitous disk-like profiles of the submm galaxies and similarity in size to these large disks suggest that SCUBA galaxies can be referred to as massive spirals at high redshift. Submm hosts are also found to have a $r_{1/2}$ similar to massive ellipticals at $z \sim 1.5$ from Longhetti et al. (2007), early-type galaxies at $1.4 < z < 3.0$ found in Daddi et al. (2005), and Distant Red Galaxies (DRGs) at $z \sim 2.5$ from Zirm et al. (2007). The submm hosts are comparable in $r_{1/2}$ to both massive spirals and ellipticals at high redshift.

2.8.3 Surface mass densities

The submm galaxies from the 8- mJy survey exhibit sizes consistent with the large spirals and elliptical galaxies at high redshift and follow a Kormendy relation similar to that of massive radio galaxies in the 3CRR sample. Inconsistency with the magnitude distribution and star-formation rate of Lyman-break galaxies suggests that these two classes of star-forming galaxy are distinct. In this section we test the assertion that submm galaxies are the progenitors of today's massive ellipticals through comparison of surface mass densities with high-redshift ellipticals, DRGs, and LBGs.

Zirm et al. (2007) separate quiescent and star-forming distant red galaxies at $z \sim 2.5$ in the Hubble Deep Field South (HDF-S) by fitting two SED models from Marston (2005): a single stellar population without dust, and constant star-formation with dust. These SED fits were also used to obtain stellar mass estimates, while morphological information was recovered via two-dimensional modelling. Galaxies best-fit by a passively evolving SED are found to be compact ($r_{1/2} \leq 1$ kpc), while the dusty star-forming sources possess more extended morphologies ($r_{1/2} \geq 2$ kpc). With similar mass estimates, the surface mass density (σ_{50}) of the quiescent and star-forming galaxies separate the two classes.

The Zirm et al. data are plotted in Figure 2.15. Star-forming DRGs are found to overlap with Lyman-break galaxies from the HDF-S in the region of local galaxy samples from Shen et al. (2003). The high surface densities of the quiescent DRGs suggest that for equivalence with local galaxies substantial downward evolution must take

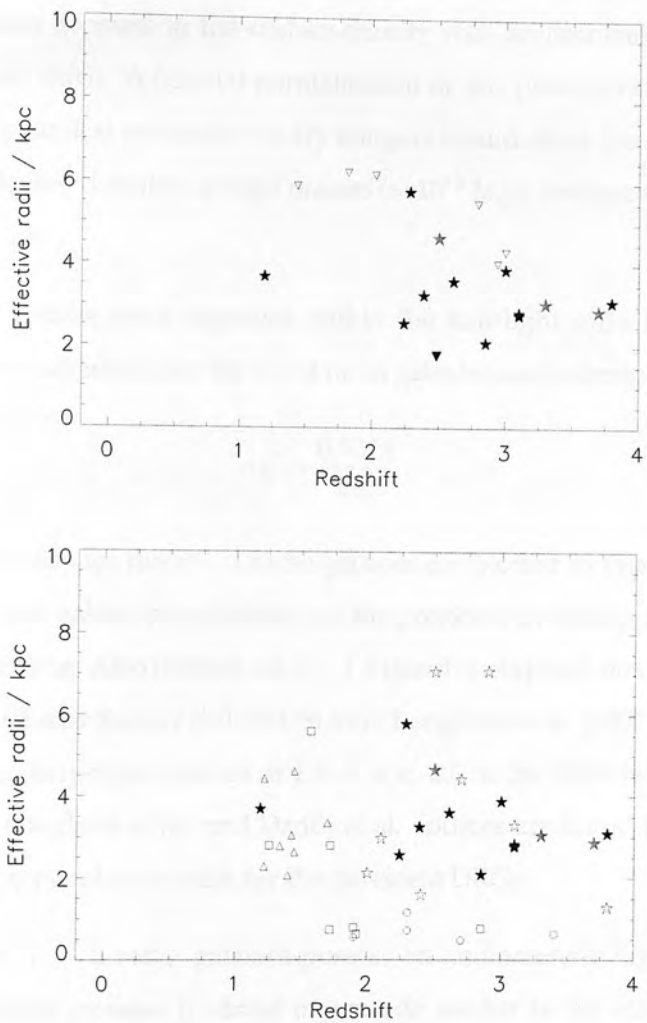

Figure 2.14: Distribution of $r_{1/2}$ with redshift for submm hosts (filled stars), massive high-redshift disks (top panel) and ellipticals (bottom panel). The inverted open triangles are large disk-like galaxies at $1.4 < z < 3.0$ found in Labbé et al. (2003). The filled inverted triangle is a disk of old stars at $z \sim 2.5$ from Stockton et al. (2004). The open circles and large open stars are respectively the quiescent and star-forming DRGs from Zirm et al. (2007). The open triangles are massive ellipticals at $z \sim 1.5$ from Longhetti et al. (2007), and the open squares are passively evolving early-type galaxies at $1.4 < z < 2.5$ from Daddi et al. (2005). The secure submm hosts are shown with dark grey shading, while unsecure identifications are indicated by light grey shading.

place between $z \sim 2$ and the present day. However, secular evolution of the compact DRGs' surface densities to local values would exceed the Hubble time. The necessary relaxation of $r_{1/2}$ is possible via dissipationless 'dry' merging (e.g. van Dokkum 2005), with a linear decrease in the surface density with accumulated mass (Nipoti, Londrillo, & Ciotti 2003). A fiducial normalisation of this power-law trend is shown in Figure 2.15. Dynamical evolution via dry mergers would allow the quiescent DRGs to reach local galaxies' densities at high masses ($\sim 10^{12}\,\mathrm{M}_{\odot}$), consistent with the $z \sim 2$ radio galaxy sample.

The average surface mass densities within the half-light radii (determined by Equation 2.5) were calculated for the $z \sim 2$ radio galaxies and submm hosts.

$$\sigma_{50} = \frac{0.5M\star}{\pi r_e^2} \tag{2.5}$$

Surface mass densities for the $z \sim 2$ radio galaxies are plotted in Figure 2.15 and are consistent with local galaxy populations and the projected evolution of the quiescent DRGs via dry merging. Also plotted are $z \sim 1.5$ massive elliptical field galaxies in the Munich Near-IR Cluster Survey (MUNICS) from Longhetti et al. (2007), and passively evolving massive early-type galaxies at $1.4 < z < 2.5$ in the HDF from Daddi et al. (2005). Both the Longhetti et al. and Daddi et al. sources are found to be consistent with the dry-merger evolution track for the quiescent DRGs.

Several of the $z \sim 2$ radio galaxies possess an anomalously high σ_{50} for their mass. These galaxies possess $K-$band magnitude similar to the other radio hosts, yet are a factor ~ 2 smaller in $r_{1/2}$. This compact $r_{1/2}$ could result from point-source contamination in the model fit reducing $r_{1/2}$. In addition, the mass estimates could be incorrect if these now-quiescent galaxies recently suffered a burst of star-formation.

The distribution of these data indicates that surface mass densities can be used to separate quiescent and star-forming DRGs. Surface mass densities for the submm sources are plotted with the Zirm et al. (2007) data in Figure 2.16. The σ_{50} was determined using $r_{1/2}$ from the two-dimensional modelling and mass estimates by match-

ing 6-arcsec aperture $K-$band magnitudes with a Bruzual & Charlot (2003) stellar population model. A majority of the submm galaxies are found to possess surface mass densities consistent with the ellipticals, with the remaining minority overlapping the star-forming DRGs, Lyman-breaks, and local populations.

A similar plot was constructed with submm galaxy mass estimates derived from Bruzual & Charlot (2003) model-fitting to multi-frequency data from IRAC, UKIRT, and Subaru. Mass estimates from multi-frequency SED fitting were found to be, on average, ~ 1.5 time smaller than the simpler mass estimates described above. This small decrease in mass proved negligible to the results, with submm galaxies common to both plots possessing the same association with the quiescent or star-forming DRGs regardless of adopted mass estimate. These trends suggest that the majority of the bright submm galaxies in the 8-mJy survey could evolve into massive ellipticals via dry mergers along the σ_{50} evolutionary track for quiescent DRGs and high-redshift ellipticals.

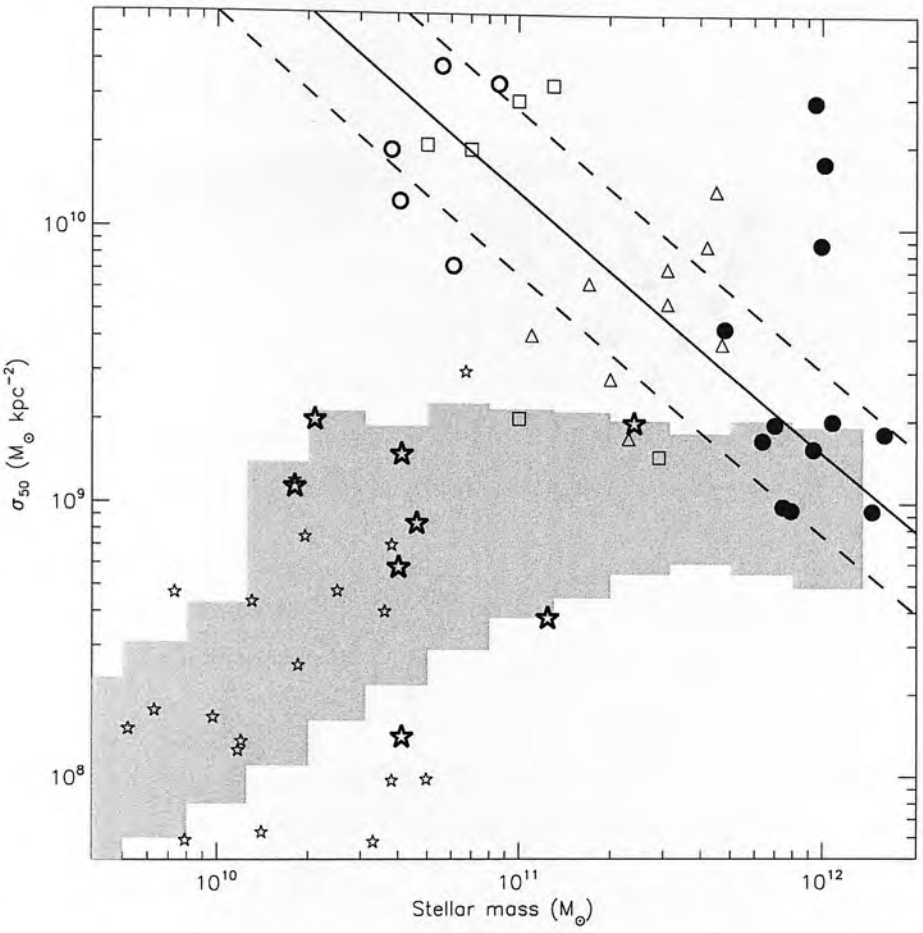

Figure 2.15: Average surface mass density within the half-light radius vs stellar mass. The $z \sim 2$ radio galaxies (filled circles) are shown with mass estimates from matching the 6-arcsec aperture $K-$band magnitudes with a Bruzual & Charlot (2003) stellar population model, and half-light radii from two-dimensional modelling. The open circles and large open stars are respectively the quiescent and star-forming DRGs from Zirm et al. (2007). The small open stars are Lyman-break galaxies also from Zirm et al. (2007). The solid line shows the simple trend of surface density with mass expected for dissipationless mergers (Nipoti, Londrillo, & Ciotti 2003) normalised to the quiescent DRGs from Zirm et al. (2007). Light-grey shading represents local values for early- and late-type galaxies from Shen et al. (2003). The open triangles are massive ellipticals at $z \sim 1.5$ from Longhetti et al. (2007), and the open squares are passively evolving early-type galaxies at $1.4 < z < 2.5$ from Daddi et al. (2005).

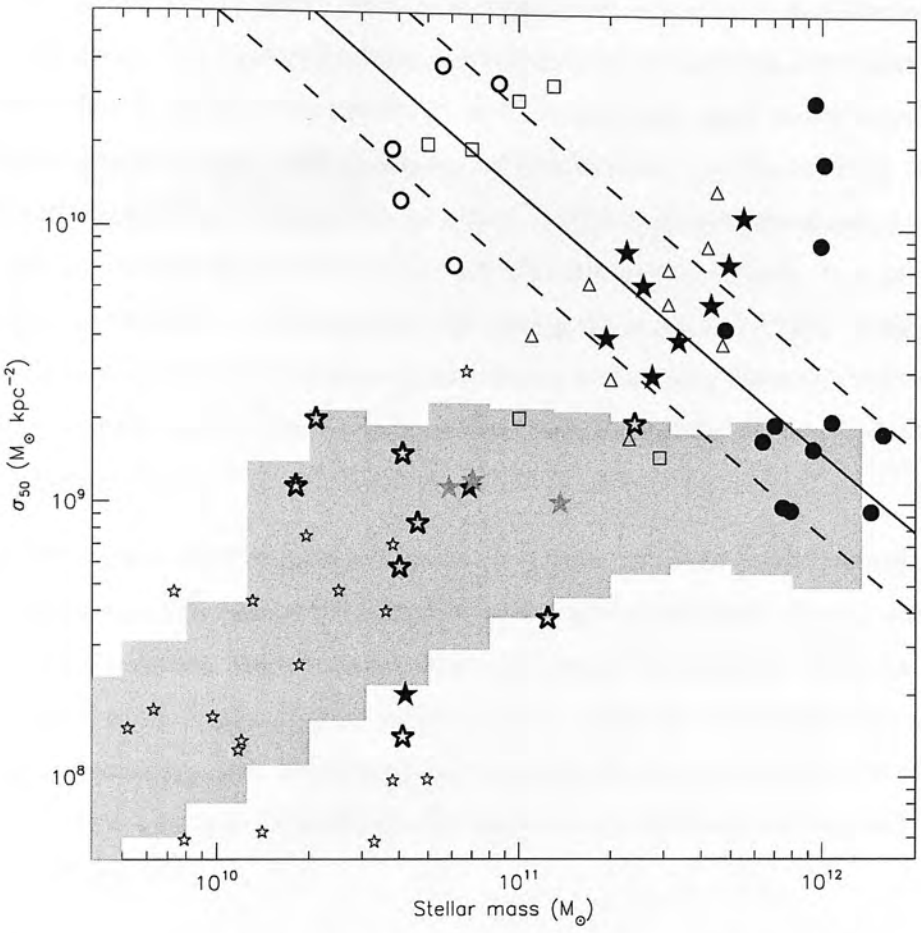

Figure 2.16: Average surface mass density within the half-light radius vs stellar mass. The submm hosts (filled stars) are shown with mass estimates from matching the 6-arcsec aperture $K-$band magnitudes with a Bruzual & Charlot (2003) stellar population model, and half-light radii from two-dimensional modelling. The secure submm hosts are shown with dark grey shading, while unsecure identifications are indicated by light grey shading. All other data matches Figure 2.15.

The properties of submm galaxies consistent with quiescent or star-forming DRGs are compared. The 5 submm galaxies consistent with star-forming DRGs and Lyman-break galaxies possess the lowest $K-$band magnitudes (and hence mass) of the SCUBA galaxy sample. With no significant difference in $r_{1/2}$, the resulting σ_{50} separates the two groups. Using averaged values, a slight but negligible decrease is found in submm luminosity from Scott et al. (2002) for the low σ_{50} sources. Also, all submm sources with high σ_{50} are identified with strong radio sources (IV02), while the low σ_{50} galaxies range from strong to non-detections in the radio. However, the variety of radio morphologies for low σ_{50} submm hosts does not distinguish them from high σ_{50} counterparts.

HST ACS $I-$band imaging of submm galaxies in the Elais N2 field from Almaini et al. (2005) reveals a substantial morphological difference between the two σ_{50} groups of submm galaxies. These data are shown in Figures 2.17 and 2.18. High σ_{50} sources are found to be bright compact major mergers, while low σ_{50} sources appear to be small diffuse irregulars. These merging systems could represent consistency with quiescent DRGs and high-redshift ellipticals along an evolutionary path towards todays' massive ellipticals.

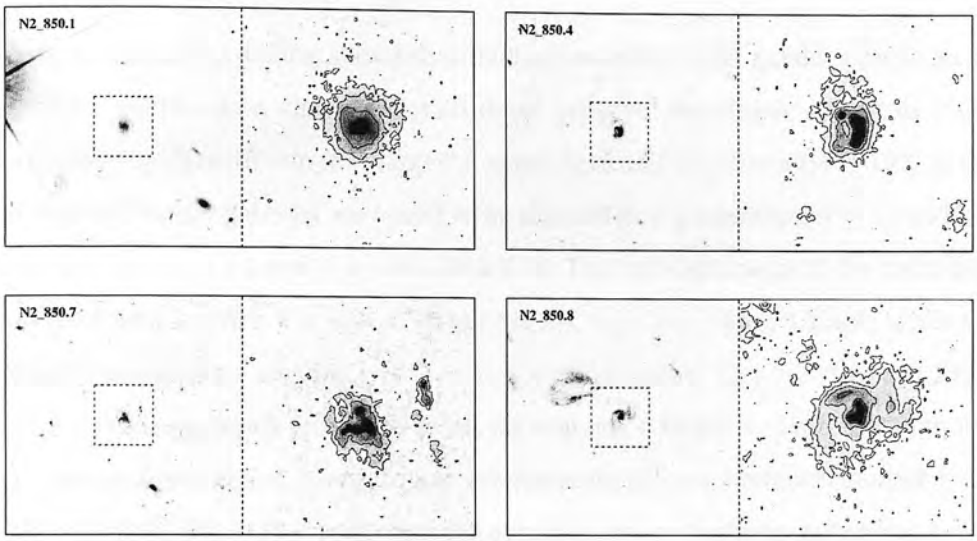

Figure 2.17: HST I−band imaging of submm hosts possessing K−band surface mass densities consistent with high-redshift quiescent DRGs and elliptical galaxies. Data taken from Almaini et al. (2005).

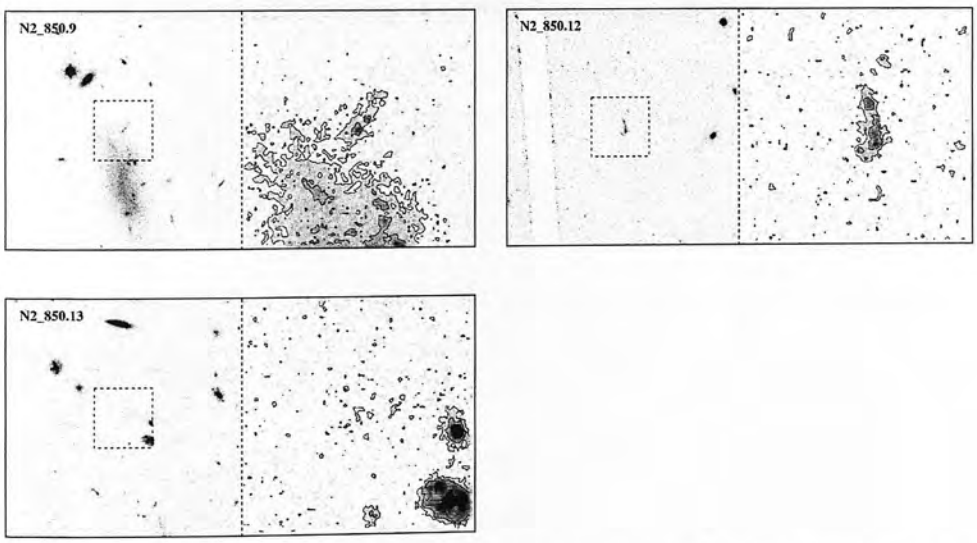

Figure 2.18: HST I−band imaging of submm hosts possessing K−band surface mass densities consistent with high-redshift star-forming DRGs and Lyman-break galaxies. Data taken from Almaini et al. (2005).

2.9 Summary

Two-dimensional modelling shows that the high-redshift radio galaxies have surface brightness distributions consistent with those expected for classic ellipticals (Sérsic parameter, $n = 4$), with n in the range $2.5 < n < 5.75$ and $< n >= 4.04 \pm 0.27$. In contrast, submillimetre galaxies are found to be disks (Sérsic parameter, $n = 1$) with n in the range $1.0 < n < 2.5$ and $< n >= 1.46 \pm 0.16$. The half-light radii of the radio hosts are spread over a range $2 < r_{1/2} < 16$ kpc with $< r_{1/2} >= 7.85 \pm 1.2$ kpc, while submillimetre sources are smaller, with $1 < r_{1/2} < 6$ kpc and $< r_{1/2} >= 3.15 \pm 0.29$ kpc. The $z \sim 2$ radio galaxies are found to be, on average, a factor ~ 2 smaller than massive radio galaxies at $z < 1$, and follow a Kormendy $(\mu_e - r_e)$ relation similar to that of 3C-type galaxies at low redshift after evolutionary corrections assuming a burst formation model at $z = 3$, consistent with the median redshift of the submillimetre sources. The $K-$band luminosities of the submillimetre galaxies are ~ 1.5 magnitudes brighter than Lyman-break galaxies at comparable redshifts, indicating that submillimetre galaxies are significantly more massive. Finally, surface mass densities for both source types are found to be consistent with quiescent elliptical galaxies at high redshift, and not star-forming or Lyman-break galaxies.

CHAPTER 3

The black hole–bulge mass relationship to z = 2

The work contained in this chapter has been published in a refereed scientific journal. Text and figures are from *'On the evolution of the black hole:spheroid mass ratio'*, McLure,R.J.; Jarvis,M.J.; **Targett,T.A.**; Dunlop,J.S.; Best,P.N. (2006), MNRAS, 368, 1395-1403. The contribution by the author included: program planning, data acquisition, data reduction, and data analysis for 3CRR radio-galaxies as described in Chapter 2.

3.1 Introduction

It is now established that at low redshift essentially all massive galaxies contain a central super-massive black hole, and that black hole mass (M_{bh}) and host spheroidal mass (M_{bulge}) are tightly correlated in both quiescent (Magorrian et al. 1998; Gebhardt et al. 2000; Ferrarese & Merritt 2000) and active galaxies (McLure & Dunlop 2001, 2002; Nelson et al. 2004). Consequently, it is widely accepted that the formation and evolution of super-massive black holes and their host spheroids must be intimately related.

At present we lack a good understanding of the origins of the black hole:spheroid connection or of its evolution with redshift. Fundamentally, it is not known whether black holes formed before, after, or coevally with their host spheroids.

Theoretical models of black hole:spheroid formation and growth can be tuned to reproduce the mass relation observed at $z = 0$ (e.g. Kauffmann & Haehnelt 2000; Archibald et al. 2002; Granato et al. 2004; Croton 2006; Robertson et al. 2006) but the empirical information required to verify or refute such models can only come from observational determination. Until now, the absence of data necessary for host-galaxy mass determination at high z has prevented further study.

Peng et al. (2006) recently concluded that the $M_{bh} : M_{bulge}$ ratio was a factor of $3 - 6$ times larger at $z \simeq 2$ than the present day, based on a sample of 15 quasars. Furthermore, at the very highest redshifts, there are also indications of evolution in the M_{bh}/M_{bulge} relation. The highest redshift quasar currently identified ($z = 6.41$) by the Sloan Digital Sky Survey (SDSS J1148+5251; Fan et al. 2003) is believed to harbour a central black hole of mass $\simeq 3 \times 10^9\,\mathrm{M}_\odot$ (Willott, McLure & Jarvis 2003a; Barth et al. 2003). However, using CO observations, Walter et al. (2004) recently estimated a dynamical mass of only $\simeq 5 \times 10^{10}\,\mathrm{M}_\odot$ for SDSS J1148+5251, clearly inconsistent with the locally observed $M_{bh} : M_{bulge}$ ratio of $\simeq 0.002$ (Marconi & Hunt 2003; Häring & Rix 2004).

Despite recent progress, addressing the evolution of the black hole:spheroid relation from an observational perspective is still a difficult proposition. The reasons for this are two-fold. Firstly, although in principal it is possible to obtain relatively accurate spheroid mass estimates for quiescent galaxies out to high redshifts, at present no viable technique is available to estimate their central black hole mass. Secondly, although it is now possible to obtain black hole mass estimates for broad-line active galactic nuclei (AGN) out to the highest redshifts using the so-called virial technique (Wandel, Peterson & Malkan 1999; Kaspi et al. 2000; McLure & Jarvis 2002; Vestergaard 2002), it remains extremely challenging to obtain accurate spheroid mass estimates for statistically significant samples of luminous high-redshift quasars.

We explore the possibility of exploiting the unification of radio-loud AGN to provide spheroidal and black hole mass estimates for a *single* population of massive early-type galaxies in the redshift range $0 < z < 2$. In the standard radio-loud unification scheme (e.g. Barthel 1989; Urry & Padovani 1995) radio-loud quasars and radio galaxies are drawn from the same parent population, with their classification as either quasars or radio galaxies dependent solely on whether our line-of-sight to the central engine intersects the obscuring torus, or not. Consequently, by using a complete sample of low-frequency selected radio-loud AGN we can adopt spheroidal mass estimates from the radio-galaxy component (where the central nucleus is obscured) and black hole mass estimates from the quasar component (where we have a direct line of sight to the central nucleus) as representative of the whole population.

3.2 Radio galaxy stellar masses

It has been known for more than twenty years that powerful radio galaxies display a tight correlation between redshift and apparent $K-$band magnitude; the so-called $K-z$ relation or near-infrared Hubble diagram (Lilly & Longair 1984). In its simplest interpretation the 3CRR $K-z$ relation is fully consistent with the passive evolution of an $\simeq 3L^{\star}$ elliptical galaxy formed in a single burst of star-formation at $z_f \gtrsim 5$ (e.g. Jarvis et al. 2001; Willott et al. 2003b). Alternatively, the $K-z$ relation is also consistent with the hierarchical merging paradigm, within which the $K-z$ relation is populated at each redshift by early-type galaxies at a specific stage of their evolutionary history (e.g. Best, Longair & Röttgering 1998). In either case, the stellar populations of the 3CRR radio galaxies ($K-$band luminosities and colours) are consistent with a high redshift of formation.

Consequently, we have based our stellar mass estimates for the 3CRR radio galaxies largely on the $K-$band photometry compiled by Willott et al. (2003b) for their study of the $K-z$ relation (corrected to a fixed 64 kpcaperture and for emission-line contamination). For the purposes of this study we have restricted ourselves to 3CRR radio galaxies with $z \geq 0.3$. The reasons for this decision are three-fold. Firstly, the

lowest redshift in the quasar component is $z = 0.305$, so it is only at $z > 0.3$ that a direct comparison between the radio galaxy and quasar components of the 3CRR sample can be made. Secondly, by restricting our analysis to $z \geq 0.3$, the 3CRR radio galaxies all have radio luminosities higher than the FRI/FRII break (Fanaroff & Riley 1974), ensuring that our radio-galaxy sample is comprised entirely of powerful FRII sources, the same radio morphology common to the entire 3CRR quasar sample. Thirdly, at $z \geq 0.3$ the radio galaxies all have radio luminosities greater than $L_{151\mathrm{MHz}} = 10^{26}\mathrm{WHz}^{-1}\mathrm{sr}^{-1}$, the radio luminosity above which the 3CRR sample is fully consistent with simple orientation-based unification (Willott et al. 2001).

The full 3CRR sample contains 57 radio galaxies in the redshift interval $0.3 < z < 1.8$. However, in this study we restrict our analysis to the complete sub-sample of 43 radio galaxies with $0.3 < z < 1.8$ and $\delta < 55°$, making it possible to compile a complete set of $K-$band photometry. The photometry for the vast majority of the sample (39/43 objects) is drawn from the compilation of Willott et al. (2003b). In addition we include K-band photometry for 3C324, 3C356 (Best, Longair & Röttgering 1997), 3C225B (Lilly & Longair 1984) and 3C322 (see Chapter 2).

In the redshift range $0.3 < z < 1.4$ the stellar masses of the 3CRR radio-galaxy hosts have been estimated by simply matching the 64 kpcaperture $K-$band magnitudes with a Bruzual & Charlot (2003) stellar population model which undergoes an instantaneous burst of star formation at a formation redshift of $z_f = 10$. At redshifts of $z \lesssim 1$, simply converting the observed $K-$band magnitudes directly into stellar mass estimates should be relatively robust, given that the underlying old stellar population should dominate rest wavelengths long-ward of 1μm. Moreover, there is now a wide variety of evidence that at $z \lesssim 1$ the properties of powerful radio-galaxy hosts (colours, scalelengths, Kormendy relation) are fully consistent with those of passively evolving early-type galaxies (McLure & Dunlop 2000; Best, Longair & Röttgering 1998; McLure et al. 2004).

However, at $z \gtrsim 1$ it could be argued that the $K-$band will be increasingly contaminated by any on-going star-formation. In order to quantify the level of on-going star-formation present in the 3CRR radio-galaxy hosts would require a level

of multi-wavelength data which does not presently exist. However, the necessary multi-wavelength data does exist for the K20 sample (Cimatti et al. 2002). The K20 sample is comprised of $\simeq 500$ galaxies in the Chandra Deep-field South region with $K_{vega} < 20$, is 97% spectroscopically complete, and has *ubvrizjhk* photometry available for each source. Based on this multi-wavelength data-set, Fontana et al. (2004) conducted a detailed study of the stellar masses of the K20 galaxies using detailed SED fitting. Furthermore, using the Fontana et al. results, Daddi et al. (2004) provide a fitting formula relating observed $K-$band magnitude to stellar mass for the K20 galaxies in the redshift range $1.4 < z < 2.5$ (see Equation 3.1), the most luminous of which are directly comparable to the 3CRR radio-galaxy hosts. Consequently, for the 3CRR radio-galaxy hosts at $z \geq 1.4$ we have adopted the stellar mass estimates provided by the Daddi et al. (2004) relation derived for the K20 sample.

$$\log(M_{bulge}/10^{11}\,\mathrm{M}_{\odot}) = -0.4(K_{mag} - 19.51) \tag{3.1}$$

The stellar mass estimates for the 3CRR radio-galaxy hosts are plotted as filled circles in Figure 3.1. A simple least-squares fit to the $M_{bulge} - z$ relation produces the result:

$$\log(M_{bulge}/\,\mathrm{M}_{\odot}) = 0.01(\pm 0.06)z + 11.73(\pm 0.06) \tag{3.2}$$

showing no evidence for evolution out to $z \simeq 2$, with the stellar masses remaining virtually constant at $\simeq 5 \times 10^{11}\,\mathrm{M}_{\odot}$. This places our stellar mass estimates for the 3CRR sample in good agreement with those derived by Rocca-Volmerange et al. (2004) using the PEGASÉ stellar population models. For completeness we have also plotted those $z < 0.3$ 3CRR radio galaxies with $K-$band photometry available in Willott et al. (2003b). Although they are not included in our analysis, the $z < 0.3$ 3CRR radio galaxies are clearly consistent with the $M_{bulge} - z$ relation fitted to the higher redshift objects. Finally, it should be noted that we have also chosen to exclude the 20 objects in the 3CRR sample which are classified as weak quasars or broad-line radio galaxies by Willott et al. (2003b). This is simply because the weak quasars are unsuitable for estimating host stellar masses (significant point-source contamination) or black hole mass (significant host-galaxy contamination). Within the radio-loud unification

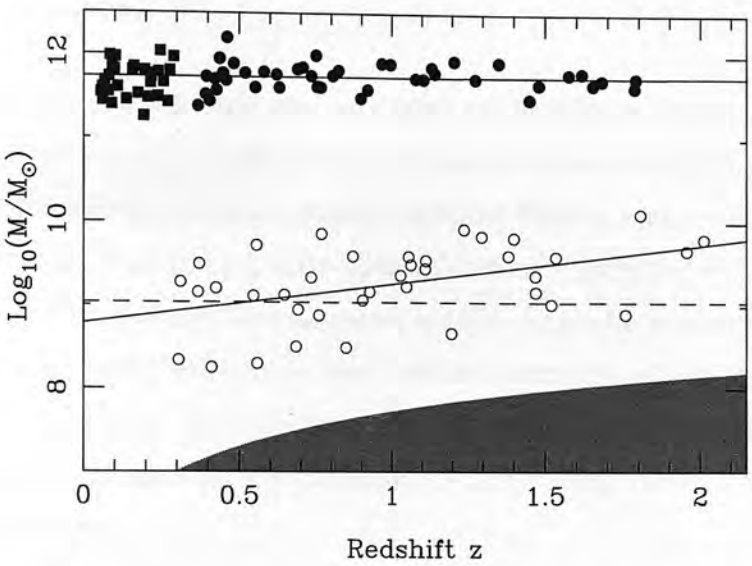

Figure 3.1: The evolution of the 3CRR radio-galaxy stellar masses (filled circles) and the 3CRR quasar black hole masses (open circles) with redshift. The solid lines are least-squares fits to the $M_{bulge} - z$ and $M_{bh} - z$ relations (Equations 3.2 & 3.3). The dashed line shows the predicted evolution of the 3CRR quasar black hole masses under the assumption that the $M_{bh} : M_{bulge}$ ratio remains constant at the local value. The filled squares show the $z < 0.3$ 3CRR radio galaxies which are not included in the fit to the 3CRR stellar masses (but are consistent with it). The shaded grey area illustrates the region from which the 3CRR quasar black hole masses are excluded by the radio flux limit (see Section 3.3 for a discussion).

scheme, weak quasars are viewed at an angle to the line-of-sight intermediate to that of quasars or radio galaxies, and their exclusion from our analysis should not therefore introduce any significant biases.

3.3 Quasar black hole masses

The black hole mass estimates for the 3CRR quasars are based on the so-called virial black hole mass estimator for broad-line AGN. Using a combination of literature data and new spectroscopic observations from ISIS on the WHT telescope we have compiled line-width measurements and black hole mass estimates for 38/39 of the broad-line quasars in the 3CRR sample. Full details of the data compiled on the 3CRR quasars, and the determination of the black hole mass estimates are provided in Table 3.1.

3.3.1 Observations

Optical spectra for the 3CRR quasars were taken on the William Herschel Telescope (WHT) on La Palma in the Canary Islands. Data were obtained with ISIS, double-arm medium-resolution long-slit spectrograph. R300B and R300R gratings were used with a 1 arcsec slit and 2 pixel binning in the spatial direction to provide a spectral resolution of ~ 3.8Å. This resolution was necessary to fully sample the narrowest expected broad lines (> 15Å FWHM), and any associated absorption troughs in MgII and CIV (e.g. Jarvis et al. (2003)). Exposure times were determined with the WHT exposure time calculator to provide a signal-to-noise ratio $> 10/pix$ using known $V-$band magnitudes of the targets.

The black hole mass estimates for the 3CRR quasars are based on the so-called virial black hole mass estimator for broad-line AGN (e.g. Wandel, Peterson & Malkan 1999; Kaspi et al. 2000). Under the assumption that the broad-line emitting gas is in virial motion within the central black hole's gravitational potential, the central black hole mass can be estimated via: $M_{bh} \simeq G^{-1} R_{blr} V^2$, where R_{blr} is the radius of the broad-line region (BLR) and V is the orbital velocity of the line-emitting gas. In practise R_{blr} is estimated via the correlation between optical luminosity and R_{blr} discovered from reverberation mapping of low-redshift AGN (Kaspi et al. 2000), and the gas orbital velocity is taken to be the FWHM of either the Hβ, MgII or CIV emission lines.

The black hole mass estimates for the 3CRR quasars are plotted as open circles in Figure 3.1. The best fit to the $M_{bh} - z$ relation (solid line) has the form:

$$\log(M_{bh}/\,\mathrm{M}_{\odot}) = 0.48(\pm 0.14)z + 8.78(\pm 0.15) \tag{3.3}$$

which is inconsistent with no evolution at the $> 3\sigma$ level. The dashed line in Figure 3.1 shows the predicted evolution of the quasar black hole masses under the assumption that the black hole masses remain a factor of $f = 0.002$ lower than the spheroid masses obtained from the radio-galaxy hosts (Equation 3.2). We have adopted $M_{bh}/M_{bulge} = 0.002$ because this is the ratio predicted by the recent studies of the local $M_{bh} : M_{bulge}$ ratio by Marconi & Hunt (2003) and Häring & Rix (2004) for a spheroidal mass of

Table 3.1: Details of the 3CRR quasars. Column one lists the source name, column two lists the source redshifts, and column three lists the V–band magnitudes. Column four lists the adopted broad-line FWHM measurements in units of 1000 km s^{-1} ($\star$ indicates a new line-width measurement based on a published spectrum), while column five lists which emission line the measurement are taken from. Column six lists the logarithm of the derived black hole mass estimates (units of $M_{\odot}$), and column seven provides the literature references from which the line-width measurements were taken. Objects listed as 'ISIS' in column seven are new line-width measurements based on spectra obtained for this study on the WHT telescope. Objects listed as 'SDSS' in column seven are new line-width measurements derived from publically available SDSS spectra. The numbered references listed in column seven are as follows: 1. Aars et al. (2005), 2. Aldcroft, Elvis & Bechtold (1994), 3. Barthel, Tytler & Thomson (1990), 4. Brotherton (1996), 5. Jackson & Browne (1991), 6. Lawrence et al. (1996), 7. Marziani et al. (2001).

Source	z	V	FWHM	Line	$M_{\rm bh}$	Reference
3C9	2.012	18.2	7.04	MgII	9.8	SDSS
3C14	1.469	20.0	9.68	MgII	9.4	ISIS
3C43	1.470	20.0	6.01	MgII	9.2	ISIS
3C47	0.425	18.1	9.88	MgII	9.2	ISIS
3C48	0.367	16.2	7.32	Hβ	9.2	ISIS
3C68.1	1.238	19.5	16.88	MgII	9.9	ISIS
3C109	0.305	17.9	5.10	Hβ	8.3	ISIS
3C138	0.759	17.9	5.14	Hβ	8.9	ISIS
3C147	0.545	16.9	8.93	Hβ	9.1	6
3C175	0.768	16.6	10.90	MgII	9.9	ISIS
3C181	1.382	18.9	9.82	MgII	9.6	ISIS
3C186	1.063	17.6	8.45	MgII	9.5	SDSS
3C190	1.197	20.0	6.33	MgII	8.7	1
3C191	1.956	18.7	11.30	CIV	9.7	ISIS
3C196	0.871	17.6	9.81	MgII	9.6	6
3C204	1.112	18.2	9.23	MgII	9.5	ISIS
3C205	1.534	17.6	6.40	MgII	9.6	ISIS
3C207	0.684	18.2	3.63	MgII	8.5	ISIS
3C208	1.110	17.4	8.70	MgII	9.4	ISIS
3C212	1.049	19.1	8.58	MgII	9.2	1
3C215	0.411	18.3	4.44	Hβ	8.3	4
3C245	1.029	17.3	$\star$6.82	MgII	9.4	1
3C249.1	0.311	15.7	7.83	Hβ	9.3	7
3C254	0.734	18.0	9.13	Hβ	9.3	5
3C263	0.646	16.3	4.76	Hβ	9.1	7
3C268.4	1.400	18.4	$\star$10.66	MgII	9.8	1
3C270.1	1.519	18.6	4.50	MgII	9.0	1
3C275.1	0.557	19.0	4.40	MgII	8.3	1
3C286	0.849	18.0	$\star$2.25	MgII	8.5	2
3C287	1.055	17.7	$\star$8.73	MgII	9.6	2
3C309.1	0.904	16.8	4.23	Hβ	9.1	6
3C334	0.555	16.4	10.65	Hβ	9.7	7
3C336	0.927	17.5	7.10	Hβ	9.2	4
3C351	0.371	15.3	8.76	Hβ	9.5	7
4C16.49	1.296	18.5	$\star$13.98	MgII	9.8	1
3C380	0.691	16.8	4.28	Hβ	8.9	7
3C432	1.805	18.0	11.37	MgII	10.1	1
3C454	1.757	18.5	4.78	CIV	8.9	3

$5 \times 10^{11}\,M_{\odot}$. The dashed line produces a fit with $\chi^2 = 63.9$ (36 degrees of freedom), compared to the best-fit with $\chi^2 = 40.6$. For two free parameters this $\Delta\chi^2 = 23.3$ suggests that the redshift dependence of the 3CRR $M_{bh} : M_{bulge}$ ratio is different from no evolution of the redshift zero normalisation at the$> 99.99\%$. [1]

Although the 3CRR sample is purely radio selected, and therefore does not have a defined optical flux limit, it is subject to an *effective* optical flux limit through the correlation between radio and optical luminosity (e.g. Serjeant et al. 1998). Consequently, it is of obvious concern that the apparent redshift evolution of the 3CRR quasar black hole masses may simply be the result of Malmquist bias.

However, it is relatively straightforward to demonstrate that this is not the case. As a function of redshift we are interested in calculating the minimum virial black hole mass that one of the 3CRR quasars could have, whilst still producing a radio source more luminous than the 3CRR flux limit. Therefore, at each redshift we first calculate the absolute radio luminosity of a source with an apparent flux density equal to the 10.9 Jy 3CRR flux limit (Laing, Riley & Longair 1983). Secondly, using the optical luminosity - radio luminosity distribution of the 3CRR quasars (Figure 3.2 we then determine the minimum allowable optical luminosity. In Figure 3.2 the adopted limiting optical luminosity as a function of radio luminosity is shown as the solid line. Although this linear relation between optical and radio luminosity provides a good description of the lower envelope of the 3CRR quasar optical luminosities, it is nevertheless somewhat arbitrary. However, it can be seen from Figure 3.2 that moving the adopted limit to significantly higher optical luminosities is clearly ruled out. Furthermore, it should be noted that moving the adopted limit to lower optical luminosities would imply greater sensitivity to lower black hole masses, making Malmquist bias less of a concern. Finally, to calculate the minimum virial black hole mass we assume that the broad emission-line velocity width must be > 2000 km s^{-1}, if the source is to be regarded as a broad-line Type 1 quasar. As a function of redshift, the resulting minimum allowable black hole mass, effectively the black hole mass completeness limit, is the upper envelope of the shaded grey region shown in Figure 3.1.

[1] All significances based on $\Delta\chi^2$ assume Gaussian errors. It should be noted that significances could be reduced depending on the true form of the error distributions.

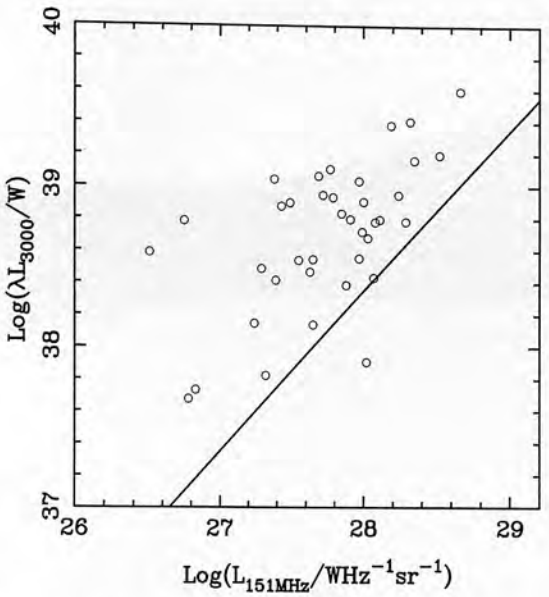

Figure 3.2: The distribution of the 3CRR quasars on the optical-radio luminosity plane. The solid line shows the relation for the lowest likely optical luminosity at a given radio luminosity adopted during the calculation of the black hole mass completeness limit as determined by eye.

The results of this calculation immediately demonstrate that the radio flux limit of the 3CRR sample does not automatically force the 3CRR quasar black hole masses to increase with redshift. On the contrary, it remains perfectly possible for the 3CRR quasars to harbour black hole masses as small as $\simeq 10^8\,\mathrm{M}_\odot$ right out to redshift $z \simeq 2$. Therefore, it seems clear that the redshift evolution of the 3CRR quasar black hole masses is genuine, and not the result of biases inherent to the 3CRR radio selection.

3.4 The evolution of the black hole:spheroid mass ratio

In Figure 3.3 we show the evolution of the $M_{bh} : M_{bulge}$ ratio within the 3CRR sample, where each data-point is simply $< log(M_{bh}/\mathrm{M}_\odot) > - < log(M_{bulge}/\mathrm{M}_\odot) >$ within each redshift bin. The solid line shows the best-fitting relation, which has the form:

$$\log(M_{bh}/M_{bulge}) = 2.07(\pm 0.76)\log(1+z) - 3.09(\pm 0.25) \tag{3.4}$$

with the dark-grey shaded region indicating the 1σ uncertainty on this fit. It can be seen from Equation 3.4 that the slope of the best-fitting relation is formally inconsis-

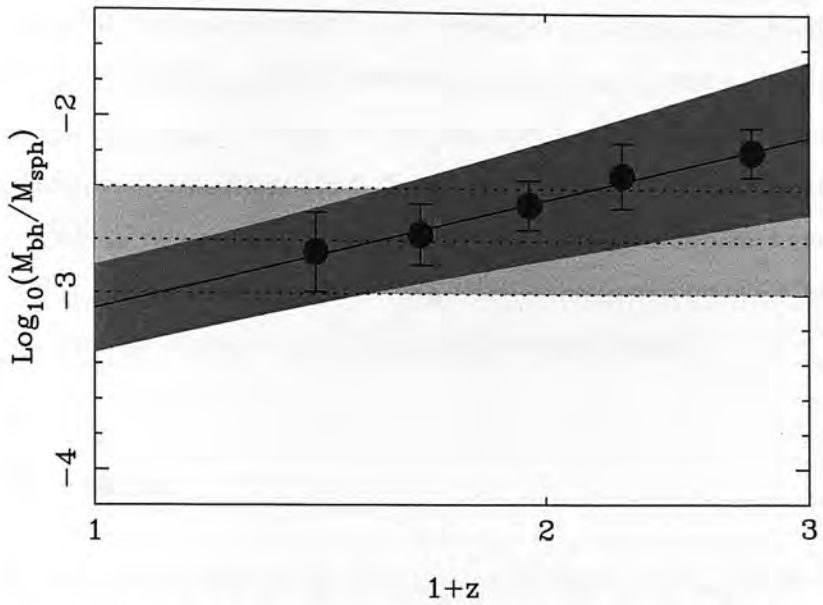

Figure 3.3: The evolution of the M_{bh}/M_{bulge} ratio for the 3CRR sample (see text for details). The solid line shows the best-fit to the observed evolution, while the dark grey shaded area shows the 1σ uncertainty of this fit. The light grey shaded area illustrates the ± 0.3 dex uncertainty on the local M_{bh} : M_{bulge} ratio, centred on $M_{bh}/M_{bulge} = 0.002$. The best-fit shown in this figure has a value of reduced $\chi^2 \ll 1$. However, alternative binning schemes produce reduced χ^2 values consistent with unity, while leaving the fitted parameters unchanged.

tent with a non-evolving M_{bh} : M_{bulge} ratio at the 2.7σ level (99%). However, it is important to note that the expected M_{bh} : M_{bulge} ratio for local quiescent galaxies of the same stellar mass as the 3CRR hosts is still relatively uncertain. In Figure 3.3 the light grey shaded area shows the ± 0.3 dex uncertainty on the redshift zero ratio of $M_{bh}/M_{bulge} = 0.002$ predicted by the recent M_{bh}/M_{bulge} studies of Marconi & Hunt (2003) and Häring & Rix (2004). It can be seen from Figure 3.3 that, although the M_{bh}/M_{bulge} ratio of the 3CRR sample is evolving over the redshift interval $0 < z < 2$, the normalisation remains within the current redshift zero uncertainties until $z \simeq 1.5$. Consequently, in evaluating the significance of the apparent evolution, it is perhaps better to look for the best non-evolving fit to the data with a normalisation within the redshift zero uncertainties (light grey shaded area). Under this constraint, the best fit to the data has $\log(M_{bh}/M_{bulge}) = -2.44 \pm 0.08$, just within the redshift zero uncertainties. However, the difference in chi-square between this non-evolving fit and the best fit is $\Delta\chi^2 = 7.4$, which for two free parameters is significant at the 98% level.

Consequently, we conclude that the data presented in Figure 3.3 provide strong evidence that the M_{bh}/M_{bulge} ratio within the 3CRR sample evolves with redshift, changing from $M_{bh}/M_{bulge} \simeq 0.002$ at redshift zero to $M_{bh}/M_{bulge} \simeq 0.008$ by redshift two. However, given the relatively large uncertainties on the local normalisation of the $M_{bh} : M_{bulge}$ ratio, it is also clear that the veracity of the apparent evolution in the $M_{bh} : M_{bulge}$ ratio of massive early-type galaxies suggested by the 3CRR sample will only be thoroughly tested by moving to higher redshifts still.

3.5 Discussion

The results presented in the last section suggest that the $M_{bh} : M_{bulge}$ ratio within the 3CRR sample is evolving with redshift, increasing by a factor of $\simeq 4$ compared to the local value by a redshift of $z \simeq 2$. However, given that the 3CRR sample is comprised of the most luminous radio-loud AGN in the universe, is it reasonable to assume that this result is in anyway representative of the dominant, quiescent early-type galaxy population? Two lines of reasoning would argue that it probably is. Firstly, recent studies of both the radio-galaxy $K - z$ diagram (e.g. Rocca-Volmerange et al. 2004) and the host galaxies of powerful radio galaxies (McLure et al. 2004; Bettoni et al. 2003; Dunlop et al. 2003; McLure & Dunlop 2000) have demonstrated that 3C-class radio-loud AGN are representative of the high-mass end of the early-type galaxy population in terms of mass, colour, half-light radius and fundamental plane location. Secondly, as previously mentioned, estimates of the duty cycle of radio-loud AGN are typically in the range $10^7 - 10^8$ years, which accounts for a negligible fraction of the evolutionary history of the host galaxies ($\simeq 10^{10}$ years). Therefore, there seems little evidence to suggest that the 3CRR sample is anything other than a random sample of the very high-mass end of the early-type mass function over the redshift interval $0 < z < 2$.

Finally, it is worth returning to the issue of the $M_{bh} : M_{bulge}$ ratio implied for the highest redshift SDSS quasar; SDSS J1148+5251 ($z = 6.41$). Both Willott, McLure & Jarvis (2003a) and Barth et al. (2003) estimate the central black hole mass to be $\simeq 3 \times 10^9$ M$_\odot$, a value which is consistent with assuming Eddington limited accretion.

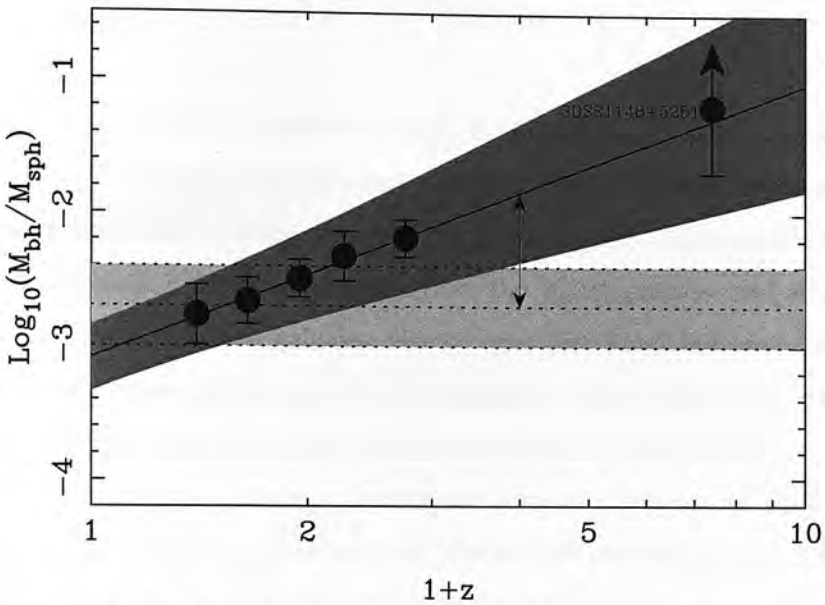

Figure 3.4: The evolution of the M_{bh} : M_{bulge} ratio for the 3CRR sample as shown in Figure 3.3, except now extrapolated out to redshift $z = 9$. Also plotted is an estimate of the M_{bh} : M_{bulge} ratio for the $z = 6.41$ SDSS quasar SDSS J1148+5251 (Fan et al. 2003) using the black hole mass estimate of Willott et al. (2003a) and the dynamical mass estimate of Walter et al. (2004). The up arrow indicates that the estimated M_{bh} : M_{bulge} ratio is based on the Walter et al. (2004) *dynamical* mass estimate, whereas the enclosed stellar mass could be considerably lower. The double arrow at $z = 3$ illustrates that the M_{bh} : M_{bulge} ratio of massive early type galaxies should be a factor of $\simeq$ 10 higher by this redshift, if the evolution suggested by the 3CRR sample is correct.

In contrast, the dynamical mass estimate of Walter et al. (2004) is only $\simeq 5 \times 10^{10}\,M_{\odot}$, implying a M_{bh} : M_{bulge} ratio of $\simeq$ 0.06, a factor of $\simeq$ 30 higher than observed locally. This is illustrated in Figure 3.4, which shows the implied M_{bh} : M_{bulge} ratio of SDSS J1148+5251 compared to the evolving 3CRR M_{bh}/M_{bulge} relation extrapolated to redshift nine. Although the good agreement between the two is no doubt fortuitous, nevertheless, it is clear that the M_{bh} : M_{bulge} ratio of SDSS J1148+5251 does not appear to be consistent with the expected local value. Figure 3.4 also demonstrates that the evolution of the M_{bh} : M_{bulge} ratio suggested by the 3CRR sample, if correct, will result in the $z \simeq 3$ M_{bh} : M_{bulge} ratio being a factor of $\simeq$ 10 higher than the local value. Such a significant difference should be detectable directly from the luminosities of the host galaxies of quasars with virial black hole mass estimates. The question of whether $z \simeq 3\&4$ quasars suggest any evolution in the M_{bh} : M_{bulge} ratio will be addressed Chapter 4.

3.6 Summary

The results are presented of a study that uses the 3CRR sample of radio-loud active galactic nuclei to investigate the evolution of the black-hole:spheroid mass ratio in the most massive early-type galaxies from $0 < z < 2$. Radio-loud unification is exploited to obtain virial black hole mass estimates from the 3CRR quasars, and stellar mass estimates from the 3CRR radio galaxies, thereby providing black hole and stellar mass estimates for a single population of early-type galaxies. At low redshift ($z \lesssim 1$) the 3CRR sample is consistent with a black-hole:spheroid mass ratio of $M_{bh}/M_{bulge} \simeq 0.002$, in good agreement with that observed locally for quiescent galaxies of similar stellar mass ($M_{bulge} \simeq 5 \times 10^{11}\,\mathrm{M}_{\odot}$). However, over the redshift interval $0 < z < 2$ the 3CRR black-hole:spheroid mass ratio is found to evolve as $M_{bh}/M_{bulge} \propto (1+z)^{2.07\pm0.76}$, reaching $M_{bh}/M_{bulge} \simeq 0.008$ by redshift $z \simeq 2$. If confirmed, the detection of evolution in the 3CRR black-hole:spheroid mass ratio further strengthens the evidence that, at least for massive early-type galaxies, the growth of the central supermassive black hole may be completed before that of the host spheroid.

CHAPTER 4

The black hole–bulge mass relationship to z = 4

A program is presented to study the co-evolution of massive galaxies and their central black holes using infrared observations of QSOs at $z = 1.5, 3, 4$. HST observations of luminous radio-loud and radio-quiet quasars in the range $0.2 < z < 2$ (McLure et al. 1999; Kukula et al. 2001; Dunlop et al. 2003; Floyd et al. 2004) show that luminous AGN are hosted by large luminous galaxies (i.e. $R_e \geq 5\,\mathrm{kpc}$, $L > L^{\star}$). Galaxy colours from the Kukula et al. (in preparation) HST/WFPC2 study of luminous QSOs indicate relatively passive stellar evolution out to $z \sim 2$. These results are consistent with recent studies of radio galaxies (de Vries et al. 2000; Zirm et al. 2003), as well as deep ground-based surveys of inactive galaxies (e.g. Glazebrook et al. 2004), which find highly evolved systems at similarly high redshifts.

Glazebrook et al. (2004) show that a significant fraction of massive inactive galaxies (i.e. $M_{bulge} > 10^{11}\,\mathrm{M}_{\odot}$) are in place by $z \sim 2$. McLure & Dunlop (2004) find that approximately 50 per cent of the local mass density of super-massive black holes ($M_{bh} > 10^{8.5}$) is already in place by $z \sim 2$. These data imply that large numbers of

galaxies at the high-mass end of the galaxy mass function are already established by $z \sim 2$. Such findings shift the emphasis of coeval black hole and galaxy evolution studies to redshifts ≥ 2.

At $z > 2$, it is *active* galaxies – in the form of quasars – which provide a unique opportunity to study how the black hole/spheroid mass relation evolves. This is because quasars are the only high-redshift objects for which estimates of *both* galaxy mass (via the luminosity of their hosts) and black hole mass (from the linewidths of broad-line clouds in the inner few parsecs) can be made. Using techniques established at $z \sim 2$ to derive black hole and host galaxy masses, samples of QSOs at $z = 1.5, 3, 4$ were used to estimate the $M_{bh} : M_{bulge}$ ratio out to $z = 4$.

4.1 Sample definition

Data were drawn from an ongoing project to obtain high-quality, near-IR imaging to determine the M_{bulge} of luminous quasars at $z = 2, 3, 4$. Figure 4.1 depicts the redshifts and luminosities of existing HST and new, partially complete $z = 2, 3, 4$ UKIRT/Gemini/VLT datasets. These new data comprise 3 sets of 10 Sloan Digital Sky Survey quasars, all with existing SDSS high-quality optical spectra, homogeneous detection criteria, and precise redshifts. Black hole mass can be obtained via virial mass estimators using broad CIV & Hβ emission linewidths and the 5100Å & 1350Å continuum luminosities from existing SDSS spectra, with quasar host luminosity derived through two-dimensional modelling and subtraction of a well-constrained PSF.

The $z > 2$ datasets shown in Figure 4.1 are under observation. In this chapter two objects from both the $z = 3$ Gemini and $z = 4$ VLT samples currently available are used. Although the results are not statistically significant, given a 4-object subsample, these data represent the highest quality and deepest near-IR images available for analysis. Also included in this chapter are a sample of 7 flat-spectrum quasars at $z = 1.5$ (*not* seen in Figure 4.1), for which M_{bh} and M_{bulge} were determined in the same fashion as the SDSS quasars. Although not suitable for direct comparison with the $z = 3, 4$ quasars, given the difference in luminosity and selection, these data were

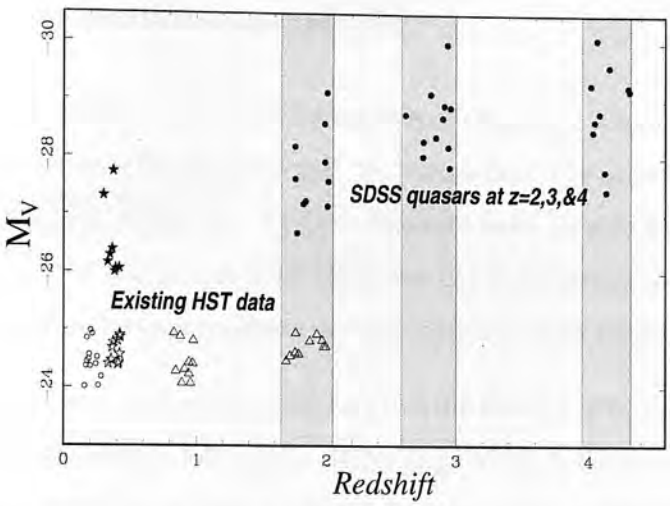

Figure 4.1: $M_V - z$ plot showing the high-luminosity quasars presented in McLure et al. (1999), Kukula et al. (2001), Dunlop et al. (2003), and Floyd et al. (2004) already observed by HST out to $z = 2$ (open symbols), and the samples of luminous SDSS quasars at $z = 2, 3, 4$ from the ongoing UKIRT/Gemini/VLT programs (filled circles).

included to provide proof of concept for the separation of nuclear and host light as described in Section 4.3.2. The original (and separate) science objectives of the $z = 1.5$ flat-spectrum quasars sample are discussed in Section 4.8.

4.1.1 z = 3, 4 radio-quiet quasar samples

The three SDSS samples shown in Figure 4.1 were selected in narrow redshift intervals centred on $z = 2, 3, 4$ and to lie within the absolute magnitude range $-26.5 > M_V > -30$. The sample consists almost entirely of radio-quiet quasars. These constitute the vast majority of the quasar population at all redshifts and are therefore more representative of the quasar population as a whole than either radio-loud quasars or radio galaxies. Each target was selected to have a star of comparable brightness to the quasar within 40 arcsec, providing a well-matched PSF model for QSO host-luminosity determination. The wavelength coverage of the SDSS spectra (3800Å→9200Å) is sufficient to include useful broad emission lines out to high redshift, such as CIV ($\lambda_{rest} = 1549$Å), which is present in the SDSS spectra out to $z \sim 4.5$. These spectroscopic data allow virial black hole mass estimates to be made for the quasars.

4.1.2 z = 1.5 flat-spectrum quasar sample

The 7-object $z = 1.5$ flat-spectrum QSO sample was originally selected to study possible inclination effects in the BLR on virial M_{bh} estimation. The quasars are all radio-loud and have $L_{408MHz}/\mathrm{WHz}^{-1}\mathrm{m}^{-2} > 10^{28}$. Thought to be viewed at an angle to the line of sight of $i < 7°$ (Jackson & Wall 1999), the flat radio spectrum ($\alpha_{rad} \sim 0$)[1] is believed to arise from the superposition of many optically thick emission regions.

Substantial evidence exists in the literature that the FWHM of broad emission lines are inclination-dependent in radio-loud AGNs (e.g. Wills & Browne 1986; Brotherton 1996; Corbin 1997; Vestergaard, Wilkes & Barthel 2000). If correct, the observed FWHM of the BLR would be dependent upon the observer's line of sight. Therefore, if FSQ are viewed virtually pole-on, the observed FWHM would be very much smaller than the intrinsic value. This distortion would render these objects unsuitable for direct comparison with the samples at $z > 2$. These separate science objectives are discussed in Section 4.8. However, host galaxies at $z = 1.5$ are more readily resolved than those at $z = 3, 4$, simplifying the use of two-dimensional modelling to recover host parameters. Analysis of this sample therefore provides a proof of concept for comparison between the two-dimensional modelling and PSF subtraction techniques used to decouple nuclear from host-galaxy flux in the higher-redshift samples.

4.2 Observations and data reduction

4.2.1 VLT imaging and spectroscopy

The 7 flat-spectrum $z = 1.5$ and 2 radio-quiet $z = 4$ quasars were imaged in the Ks–band with the Very Large Telescope (VLT) located on Cerro Paranal in the Atacama Desert, northern Chile. The VLT was also used to obtain the spectra of the flat-spectrum QSOs. Data were taken with the Infrared Spectrometer And Array Camera (ISAAC), a combined imager and spectrograph. ISAAC's SW-arm comprises a 1024

[1]The definition $S_\nu \propto \nu^{\alpha_{rad}}$ is used, where S_ν is the flux density at frequency ν and α_{rad} is the radio spectral index.

Table 4.1: Details of the VLT and Gemini QSO samples. Column 1 lists the target object names. Column 2 lists the total exposure time in seconds. Column 3 lists the measured apparent 6-arcsec aperture diameter magnitude (in the Vega system) with associated errors, as determined by randomly placed sky apertures. Column 4 lists the target redshifts.

Source	Exp. time	$K-$mag.	z
PKS 1430−155	5310	18.01±0.15	1.573
PKS 1511−100	5130	14.05±0.05	1.513
PKS 1532+01	5310	16.39±0.07	1.435
PKS 1548+056	5400	15.04±0.05	1.422
PKS 1602−00	5310	15.19±0.05	1.629
PKS 2021−330	4470	16.89±0.12	1.470
PKS 2058−297	5040	15.19±0.06	1.492
SDSS J001025.90+005447.6	12375	16.17±0.09	2.847
SDSS J104253.43−001300.9	8875	16.70±0.11	2.957
SDSS J122654.38−005430.4	8750	15.57±0.09	2.611
SDSS J125241.54−002040.5	7500	16.58±0.14	2.898
SDSS J142709.81+001450.2	8000	16.10±0.11	2.908
SDSS J152119.68−004818.6	5375	15.68±0.08	2.934
SDSS J235628.96−003601.8	9000	15.85±0.09	2.937
PKS 0040−005	9000	16.52±0.12	2.806
SDSS J131052.50−005533.2	15624	16.50±0.06	4.155
SDSS J144617.35−010131.1	18480	16.70±0.05	4.161

$\times$ 1024 Hawaii Rockwell array (typically used for shorter wavelengths, i.e. 1-2.5μm), while the LW-arm comprises a 1024 $\times$ 1024 InSb ALADDIN array (originally used exclusively for longer wavelengths, i.e. 3-5μm, although recently opened for use as a J, H, and $K-$band imager). Both arms have a pixel scale of 0.148 arcsec pixel^{-1}, providing a 2.5′ $\times$ 2.5′ field of view (FOV).

The $z = 4$ imaging data were taken with the Hawaii Rockwell array in the $Ks-$band. Raw data files consisted of 7 co-added exposures of 12 seconds each. Photometric standards were observed and pipeline-reduced at the start of each observation. Data were taken in < 0.6 arcsec seeing and photometric conditions. Calculation of the necessary total exposure times is complicated for these high-redshift galaxies, with unknown amounts of stellar and morphological evolution to offset against the K-corrections. However, studies of the $K - z$ relation for radio galaxies (e.g. Willott et al. 2003b) suggest that at $z = 4$, massive (3L$\star$) galaxies typically have apparent

magnitudes of $K \sim 19.5$. Such galaxies would passively evolve into $3L^{\star}$ objects by $z \sim 0$. This is consistent with the Floyd et al. (2004) observations of very luminous low-redshift quasars, which showed that their hosts are among the most luminous ($> 2L^{\star}$) present-day ellipticals. Simulated data recovered with two-dimensional modelling code indicated that in order to determine total luminosities for such galaxies reliably, surface-brightness profile must be followed out to a radius of ~ 4 arcsec (~ 3 expected galaxy half-light radii). This necessitates integrating down to a 3σ surface-brightness level of $\mu_K \sim 25$ mag. arcsec^{-2}. Assuming that the hosts lie on the Radio Galaxy (RG) $K - z$ relation, it was calculated from the published ISAAC sensitivities that ~ 5 hours of on-source integration would be necessary to obtain this depth. Exposure times were set to 6.5 hours on source to account for potential losses due to overheads.

The $z = 1.5$ QSOs were imaged with the ALADDIN array in the $Ks-$band. Raw data files consisted of 6 co-added exposures of 15 seconds, averaged to a 15-second integration. Photometric standards were observed and pipeline-reduced at the start of each observation. Observations were taken in < 0.6 arcsec seeing and photometric conditions. Exposure times were calculated in a similar fashion to the $z = 3, 4$ samples, with magnitude estimates derived from the infrared Hubble diagram.

Spectra of the $z = 1.5$ QSOs were obtained with ISAAC's SW-arm in Infrared Short Wavelength Spectroscopy Mode, with a resolution of 3.5Å pix^{-1} and a central wavelength of 12500Å selected to cover the H_{β} and 5100Å region of the rest-frame spectra at $z = 1.5$. The data were pipeline-reduced in the standard fashion, then flux- and wavelength-calibrated. Exposure times were set with the ISAAC Exposure Time Calculator to provide a high signal-to-noise ($20 \rightarrow 50/pix$), found to be sufficient for accurate recovery of broad-line FWHM in previous studies.

4.2.2 Gemini imaging

All objects in the $z = 3$ sample were imaged in the $K-$band with the Gemini North Telescope on Mauna Kea, Hawaii. These observations used the Near-Infrared Imager

(NIRI), a 1-5μm camera with a 1024 $\times$ 1024 ALADDIN InSb array. Camera f/14 with a pixel-scale of 0.0499 arcsec pixel^{-1} provided a 51′ $\times$ 51′ FOV. Raw data files consisted of 5 co-added exposures of 25 seconds each. Photometric standards were observed at the beginning of each night, and observations were taken in < 0.6 arcsec seeing and photometric sky. Integration times were set using the RG $K - z$ relation, following the Floyd et al. (2004) results which indicate that luminous quasar hosts should be the precursors of today's $> L^{\star}$ ellipticals. Exposures of 2.5 hours (based upon estimates from the NIRI Integration Time Calculator) were set to reach a $\sim 3\sigma$ surface-brightness limit of $\mu_K \sim 24$mag. arcsec^{-2}.

4.2.3 Data reduction

Data reduction of the VLT samples followed procedures outlined in Section 2.3 up to the registration of the final mosaic. Initial reductions of these data were registered as described, with offsets derived from the identification of one object on each frame used to create a final shiftlist by aligning multiple objects over the field. This shiftlist was passed to the IRAF routine REGISTER to shift and combine the images using a linear interpolation. It was found that these early mosaics displayed a significant increase in the final source FWHM when compared with the average FWHM of the source in each frame. The FWHM was also found to vary across the image, depending upon the position of objects used in frame alignment. This degradation of FWHM was not observed in the UKIRT or Gemini data analysed in Chapter 2, nor in the Gemini $z = 3$ quasar sample. It was determined that the poorer sampling (0.148 arcsec pixel^{-1}) of the VLT data prevented accurate determination of a common shiftlist for the images.

PSF consistency and quality are critical to decouple the nuclear point source from host galaxy in quasar imaging data. Consequently, two modifications were made to image registration for these VLT data. Final mosaics were created for each QSO and PSF star using shiftlists derived from each individual object. Image registration was then performed using a Spline3 interpolation in the IRAF routine IMSHIFT. The resulting improvements in FWHM quality are presented in Table 4.2. A clear improvement in FWHM is seen when using object-specific shiftlists and Spline3 interpolation.

Table 4.2: Comparison of FWHM for SDSS J131052.50−005533.2 and two PSF stars on the field using linear and Spline3 image registration. Column 1 lists the objects reduced with object-specific shiftlists. Column 2 lists average FWHM for individual unshifted frames. Columns 3 and 4 list the resulting FWHM from mosaics derived using Linear and Spline3 interpolations respectively. All FWHM values are given in pixels.

Source	Frame average	Linear	Spline3
QSO	2.28	2.51	2.32
PSF star 1	2.26	2.62	2.31
PSF star 3	2.25	2.58	2.30

Similar tests for the better-sampled UKIRT and Gemini data do not find a significant difference between linear and Spline3-interpolated shifts. However, for consistency the $z = 3$ Gemini quasar sample was re-reduced in this manner.

Discrepancies between the discrete pixel data and the Spline interpolation introduce some distortion (typically found to be broadening) in image shifting. The effects of Spline3 shifting were tested via comparison of source FWHM from shifted and unshifted flat-fielded frames. A negligible increase in FWHM between unshifted (∼2.89 pixels) and shifted (∼2.96 pixels) images was found.

4.2.4 Sky subtraction

The data-reduction process described in Section 2.3 subtracts the sky in each flat-fielded frame, based upon statistics from a patch of sky known to be blank at all jitter positions. The median pixel value with iterated sigma-clipping was found to be the most unbiased estimator of sky counts, although still susceptible to bias from unseen faint sources. All resulting mosaics will contain some fraction of their original sky counts, generally on the order of ± 0.02 counts per pixel. With the 0.148 arcsec pixel^{-1} scale for VLT data, this could correspond to $\sim$ 25 counts in a 6-arcsec aperture. Although negligible when compared with the $\sim$ 7000 counts for a typical QSO or PSF, these residual counts could bias the normalisation of QSO and PSF necessary for host luminosity determination. A comparison of QSO/PSF subtractions with and without

removal of latent sky counts indicated that the measured residual host-galaxy flux after subtraction could be affected by the presence of the residual sky. Curve-of-growth analysis provided a robust and unbiased estimator of the residual sky. Given slight variations across the images, each QSO and all associated PSF stars were individually processed to determine their local sky. Subsequent surface-brightness profile analyses verified the accuracy of this residual sky subtraction, with ~ 50 per cent of sky annuli possessing negative values, indicating an even distribution of sky around zero.

4.2.5 Photometric standards

Standard stars were observed with each target in the VLT and Gemini imaging for photometric calibration. VLT standards were pipeline-reduced, while Gemini standards were reduced in the same manner as the science data. Aperture photometry for these stars produced K and $Ks-$band zero-points for each target, consistent with referenced Vega values of 23.4, 23.7, and 24.14 for the Gemini, VLT LW-arm, and VLT SW-arm respectively. The good agreement between the calculated zero-points and the canonical values confirms that the data were obtained in photometric conditions.

4.2.6 VLT and SDSS spectra

Spectra for the $z = 1.5$ QSOs from ISAAC on the VLT, and the archive SDSS spectra for the $z = 3, 4$ samples were retrieved fully flux- and wavelength-calibrated. VLT spectra were scaled to the standard units ($10^{-17}\mathrm{ergs\,s^{-1}cm^{-2}\AA^{-1}}$) used by the SDSS. The SDSS data also included a separate continuum-subtracted spectra. The continua in the VLT data were fit in IRAF with CONTINUUM and subsequently subtracted.

4.3 Host galaxy analysis

Two-dimensional modelling of quasars with a well-matched PSF is the most robust available method for decoupling nuclear from host flux in QSO. However, if the scale-length of the hosts becomes smaller than the PSF's FWHM it becomes increasingly

difficult to disentangle the host and nuclear flux with any reliability. Massive 3CRR radio galaxies (see Chapter 2) and massive field ellipticals (Longhetti et al. 2007) are found to be a factor of $\sim$ 2 and $\sim$ 1.5 respectively smaller than their low-redshift counterparts. This suggests possible size evolution in massive galaxies at high redshift, which could impair two-dimensional modelling. Measurements are presented to ensure a well-matched QSO/PSF morphology in conjunction with two techniques to determine quasar host-galaxy luminosity.

4.3.1 PSF stars, saturation, and non-linearity

A well-matched QSO and PSF (in this case provided by a star) is critical to nuclear/host flux separation. Unlike space-based imaging, where the PSF is largely stable over time and also reproducible, fluctuations in seeing necessitate simultaneous observation of target and PSF in ground-based data. All targets were imaged with an equally bright or brighter star within the FOV. A PSF star brighter than the target QSO should provide an excellent FWHM match and high signal-to-noise in the wings of the profile. This PSF could then be subtracted from the quasar to separate an underlying host signal.

During data reduction, individual frames with poor image quality (as determined by FWHM) were removed. However, data-screening for the QSO samples also required consideration of source saturation and non-linearity. Exposure times were set to be well within the background-limited regime and to ensure a non-saturated PSF star. However, fluctuations in seeing (found to be as low as 0.25 arcsec) occasionally led to saturation in some frames. Saturation or non-linearity in a star would invalidate its use as a PSF, as its morphology would diverge from that of the QSO. These data were filtered using the peak pixel counts recorded for each target object during its identification for use in shiftlist creation. Any frame found to possess counts-per-pixel greater than the non-linearity limits listed in the literature was discarded. During data reduction it was occasionally found that the original PSF star was consistently saturated or non-linear. Attempts at recovering QSO host information with these PSFs proved ineffective, even where peak counts in the PSF approached the lower bound-

ary of non-linearity. The sensitivity of host-galaxy signal recovery to PSF variation also demonstrated the need to establish that PSF-subtracted QSO residuals represent QSO host flux and not PSF mismatch in the subtraction. Where possible, several alternate PSF stars were chosen from each image. Selection was based upon similarity in luminosity, proximity, and FWHM stability. Comparison of residuals from two well-matched PSF stars subtracted from each other could then quantify the level of error in the PSF-subtracted host-galaxy residuals. Where the original PSF star was not saturated or non-linear, it was used in conjunction with two alternate PSF stars.

4.3.2 PSF star selection and subtraction

After selection of several potential PSF stars from each image, reduced data were checked via model-fitting and curve-of-growth analysis to determine the FWHM match of the QSOs and PSF stars. These comparisons are presented in Table 4.3. A consistently higher FWHM for QSOs in comparison with the PSF stars is found in virtually all cases. This is consistent with the QSO profile representing a combination of both a point source and extended host galaxy. A comparison of FWHMs indicated that typically two PSF stars share a value similar to that of the QSO, while the third differs significantly. Poorly matched stars were excluded, with the two remaining used as PSFs during modelling and further analysis. The peak-pixel counts presented in Table 4.3 also suggest that better QSO/PSF FWHM matches are found when the two are of similar brightness. This could result from a small level of non-linearity at high count levels, or poorer signal-to-noise in fainter sources.

Unfortunately, only the original bright PSF stars were available for the $z = 3$ quasar data, with no viable alternative stars in the relatively restricted $50' \times 50'$ FOV of Gemini NIRI. Consequently, use of PSF–PSF subtraction to determine the magnitude of potential PSF mismatch was not possible. Large differences in QSO/PSF FWHM rendered many objects in the $z = 3$ sample unusable in this analysis. The two objects selected represent the best QSO/PSF FWHM matches in the 8-object sample. Analysis of the remaining 6 objects may be possible at a later date.

Table 4.3: Comparison of FWHM for $z = 1.5, 3, 4$ QSOs and associated PSF stars. Column 1 lists QSO names. Column 2 lists the QSO or PSF star under examination. Columns 3 and 4 list the resulting peak pixel counts and FWHM measured from a mosaic aligned solely from the target object. FWHM values are given in pixels. Peak pixel counts are the sum of the total integration.

Target QSO	z	Shifted Object	Peak counts	FWHM
PKS 1430−155	1.573	QSO	8493	2.95
PKS 1430−155		alt1	635862	2.94
PKS 1430−155		alt2	485041	2.74
PKS 1430−155		alt3	84982	2.87
PKS 1511−100	1.513	QSO	557985	2.56
PKS 1511−100		alt1	607720	2.62
PKS 1511−100		alt2	243537	2.49
PKS 1511−100		alt3	184987	2.46
PKS 1532+01	1.435	QSO	29754	3.64
PKS 1532+01		alt1	200251	3.60
PKS 1532+01		alt2	190273	3.63
PKS 1532+01		alt3	26056	3.62
PKS 1548+056	1.422	QSO	54622	5.14
PKS 1548+056		alt1	19785	5.16
PKS 1548+056		alt2	12210	5.36
PKS 1548+056		alt3	8493	5.26
PKS 1602−00	1.629	QSO	137553	3.13
PKS 1602−00		alt1	202892	3.33
PKS 1602−00		alt2	149309	3.16
PKS 1602−00		alt3	71297	3.13
PKS 2021−330	1.470	QSO	26277	2.91
PKS 2021−330		alt1	243465	2.86
PKS 2021−330		alt2	61676	3.11
PKS 2021−330		alt3	39358	2.87
PKS 2058−297	1.492	QSO	139081	2.91
PKS 2058−297		alt1	116933	2.99
PKS 2058−297		alt2	90056	3.18
PKS 2058−297		alt3	61217	3.26
SDSS J104253.43	2.957	QSO	56661	6.59
SDSS J104253.43		PSF	500256	6.31
SDSS J142709.81	2.908	QSO	32510	10.79
SDSS J142709.81		PSF	30427	10.01
SDSS J131052.50	4.155	QSO	294766	2.32
SDSS J131052.50		alt1	649551	2.31
SDSS J131052.50		alt2	1.969E6	2.50
SDSS J131052.50		alt3	1.521E6	2.30
SDSS J144617.35	4.161	QSO	205473	2.75
SDSS J144617.35		alt1	862600	2.80
SDSS J144617.35		alt2	385910	2.73
SDSS J144617.35		alt3	174861	2.78

Two anomalies are seen in Table 4.3. Firstly, PKS 1548+056 is found to have only one well-matched star. Secondly, the PSF stars for PKS 2058−297 are all significantly broader than the QSO and do not possess FWHMs within ~ 1 per cent of the QSO (as found for the other sources). Consequently, PKS 2058−297 was excluded from further analysis as no viable PSF star was available.

PSF subtraction

Two methods were used to determine the quasar nuclear-to-host ratios: normalised PSF subtraction (providing a minimum host-galaxy flux but effective at all redshifts) and two-dimensional modelling (a more robust measure of true host flux, although less effective for nuclear-dominated hosts of small angular size). The model-independent PSF subtraction technique was used to confirm the detection of an underlying host. Both the QSO and two PSF stars for each source were centroided with the IRAF routine IMSHIFT. Resulting images were then normalised by counts in their central pixel, and directly subtracted from each other. The residual counts within a 6-arcsec-diameter aperture were measured and are presented in Table 4.4. As the QSO image is a composite of host-galaxy and nuclear flux, normalised subtraction of the PSF from the QSO should leave residual host flux, assuming that the galaxy signal is of sufficient signal-to-noise. A consistent and positive residual from both QSO/PSF star subtractions – an order of magnitude larger than the residual from the two normalised PSFs subtracted from each other – confirms the detection of an underlying host. Table 4.4 shows clear detections of 5 underlying hosts at $z = 1.5$, 1 at $z \sim 3$, and both $z \sim 4$ QSOs. PSF−PSF star subtractions demonstrate that potential signal from QSO/PSF mismatch is consistently an order of magnitude smaller than the residual host-galaxy flux.

Normalised PSF subtraction was then used to determine a minimum luminosity for the QSO host galaxies. A PSF star with the closest FWHM match to the QSO was selected. IDL code developed by the author was used generate a series of PSF images whose peak-pixels were normalised (based upon previous experience) to between 1 and 0.95 times that of the QSO. These PSF normalisations were then subtracted from

Table 4.4: Comparison of normalised PSF from QSO, and PSF from PSF subtraction residuals from a 6-arcsec-diameter aperture in counter per second. Column 1 lists the QSO name. Columns 2, 3, and 4 list the residuals from the normalised subtraction of PSF stars (with the closes FWHM match to the QSO) from the QSO. Column 5 lists the residual from the normalised subtraction of one PSF from another, representing the expected levels of error in a QSO/PSF subtraction from mismatch in the PSF.

Target QSO	PSF Alt 1	PSF Alt 2	PSF Alt 3	PSF−PSF
PKS 1430−155	4.902		4.909	0.007
PKS 1511−100		0.892	0.666	0.023
PKS 1532+01	3.070		3.058	0.012
PKS 1548+056	0.407			
PKS 1602−00		0.292	0.641	0.035
PKS 2021−330	2.999		3.390	0.391
PKS 2058−297	-1.997	-0.699	-5.127	
SDSS J104253.43−001300.9	6.310			
SDSS J142709.81+001450.2	20.329			
SDSS J131052.50−005533.2	0.314		0.205	0.011
SDSS J144617.35−010131.1		0.027	0.025	0.001

the QSO image, and surface-brightness profiles were plotted for the resulting residuals. As the nuclear-to-host flux ratio is unknown, it is impossible to determine the exact fraction of PSF to subtract when using this technique. However, by selecting a PSF normalisation that produces a monotonically increasing surface-brightness profile in the inner pixel annuli, a minimum level of host flux can be determined. Although still technically an over-subtraction, this point between a clear over-subtraction (i.e. a profile which decreases toward the centre) and an under-subtraction (i.e. where the profile is positive in the centre, but as the true nuclear-to-host ratio is unknown, any fraction over a flat profile cannot be justified) represents the minimum contribution from the host galaxy that is possible without the risk of including nuclear contributions in the subtracted residual.

Having determined this minimum fraction of host-galaxy signal in the QSO's central pixel, the image was normalised to match and the total flux from a 6-arcsec-diameter aperture measured. A similar manual examination of these subtractions was

made to identify the point at which the central 9 pixels contained the same counts per pixel. These two methods produced well-matched results. An example of a QSO profile before and after scaled PSF subtraction to produce a monotonic residual is presented in Figure 4.2.

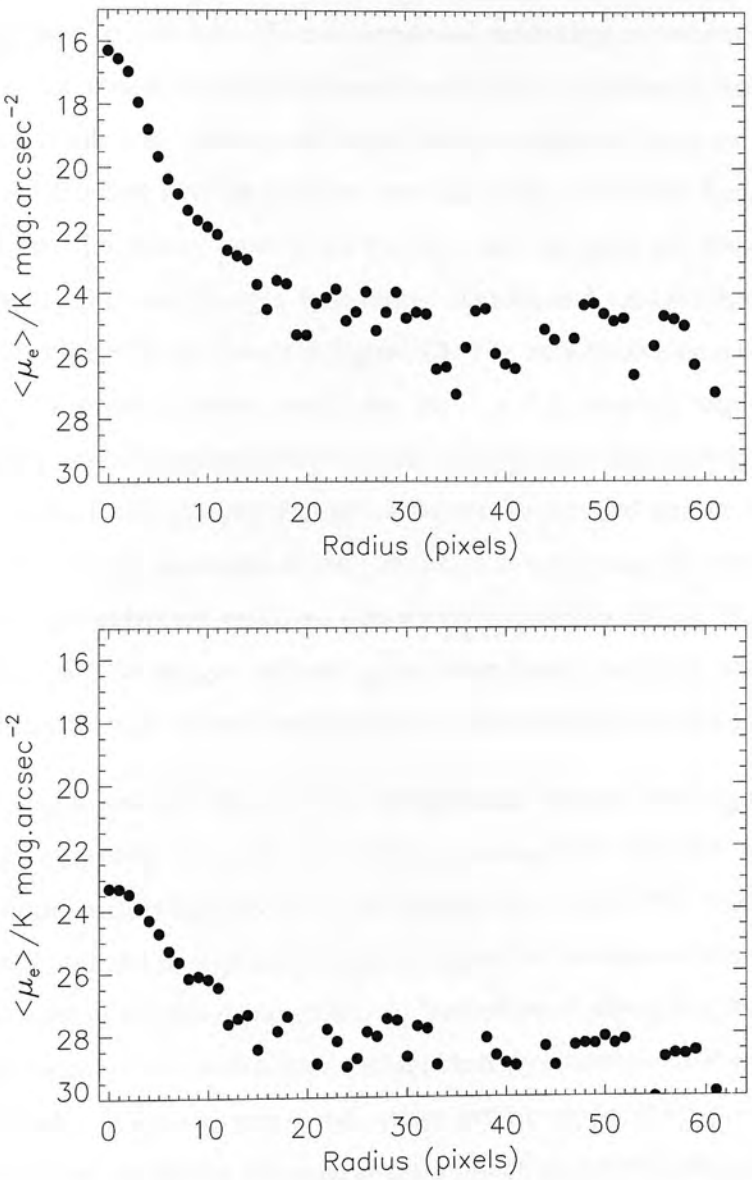

Figure 4.2: Example of raw QSO surface-brightness profile (above) and a monotonically increasing surface-brightness profile from normalised subtraction of a well-matched PSF star (below).

Two-dimensional modelling

Scaled PSF subtraction provides a robust measure of the *minimum* contribution from a host galaxy in the observed QSO, but is unable to provide a reliable measure of the *true* nuclear-to-host ratio. Two-dimensional modelling as described in Chapter 2 was used to recover host-galaxy parameters and flux contribution from the quasar data. These models included the additional free parameter of an unresolved nuclear point source. The best FWHM-matched star was used as the PSF during modelling. The best-fit model galaxy parameters for all quasar samples are presented in Table 4.5. The reduced quasar images, best-fitting models, and model-subtracted residuals for the $z = 1.5$ QSOs are shown in Figure 4.3. The two-dimensional modelling code was unable to return accurate results for the $z = 3, 4$ samples, implying that the hosts possess angular sizes such that they do not contribute significantly beyond the central few pixels. Consequently, Figure 4.4 shows the reduced quasar image, selected PSF star, and the residual after scaling to obtain a monotonic surface-brightness profile. These PSF-subtracted residuals present morphologies distinct from asymmetries in the QSO or PSF images, indicating that morphological information from the host is present, although not recoverable via two-dimensional modelling.

It was found that the $z = 1.5$ flat-spectrum quasars are large ($< r_{1/2} >= 4.1 \pm 1.0\,\mathrm{kpc}$) ellipticals ($< n >= 4.2 \pm 0.8$) (excluding PKS 2058−297 and PKS 1511−100). The model results for PKS 1511−100 represent a fit to the PSF only (negligible flux associated with the host galaxy). This is indicated by a collapsed Sérsic Index $\equiv 1$ (a hard lower limit in the code) and small $r_{1/2}$, indicative of attempting to fit host galaxy flux in the central pixels, which does not significantly contribute to the combined profile at larger radii. In quasars where the surface-brightness profile beyond the central pixels is dominated purely by the nuclear component, or where host galaxies have angular sizes such that they do not contribute significantly beyond the central few pixels, the nuclear-dominated wings will be fit solely with the PSF. In these cases the code is unable to determine morphology for the residual (essentially PSF-subtracted) core. Such

Table 4.5: Results of two-dimensional modelling of the $z = 1.5, 3, 4$ quasar samples. Column 1 lists the the source name. Columns 2 and 3 list the best-fit counts from the nuclear and host-galaxy components in the model. Column 4 lists the semi-major axis scalelength of the host-galaxy fit in kiloparsecs. Column 5 lists the mean surface brightness in K or Ks magnitudes per square arcsec. Column 6 lists the value of the Sérsic Index. Column 7 lists the axial ratio of the host galaxy. Column 8 lists the total host-integrated magnitude and Column 9 the reduced χ^2 of the model fit.

Source	Nuclear	Host	$r_{1/2}$	$< \mu_e >$	Sérsic n	Ax-ratio	$K-$mag.	χ^2
PKS 1430−155	122	83	7.63	20.27	1.17	2.18	19.35	1.06
PKS 1511−100	6005	1291	1.61	14.15	1.00	1.74	16.36	1.32
PKS 1532+01	697	160	3.50	17.36	5.15	3.47	18.63	1.27
PKS 1548+056	2817	300	1.89	15.64	4.45	2.64	17.95	1.18
PKS 1602−00	2332	179	2.33	16.98	5.81	1.93	18.51	1.37
PKS 2021−330	416	127	5.65	19.68	3.91	1.35	18.88	1.21
SDSS J104253.43	397	86	1.13	16.39	6.51	1.00	–	1.92
SDSS J142709.81	722	0	–	–	–	–	–	–
SDSS J131052.50	916	71	0.51	15.86	1.17	2.12	–	2.03
SDSS J144617.35	997	162	0.51	14.96	1.00	3.75	–	3.10

a fit is seen for PKS 1511−100 (the brightest object in the $z = 1.5$ sample) and for the $z = 3$ and $z = 4$ data.

Comparison of minimum host-galaxy flux as determined by scaled PSF subtraction and two-dimensional modelling for the $z = 1.5$ sample indicates that the PSF-subtraction technique consistently underestimates host flux by an average factor of $\sim 1.3 \pm 0.1$. For the un-modelled $z = 3, 4$ samples, the minimum flux as determined by PSF subtraction was multiplied by this factor to provide a better luminosity estimate. In terms of magnitude, this correction corresponds to only ± 0.27 mag.

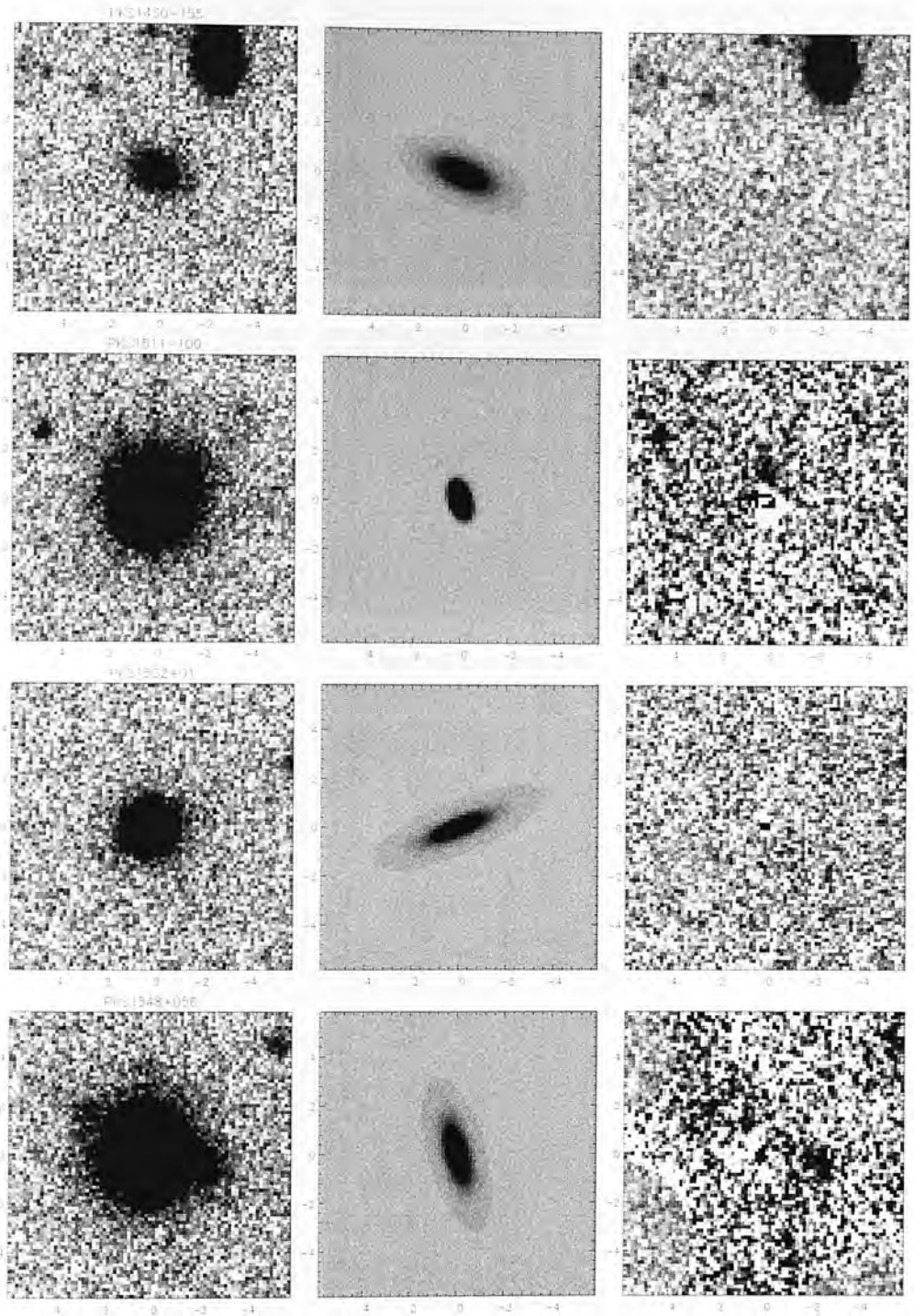

Figure 4.3: Two-dimensional modelling analysis of the flat-spectrum QSOs. The left-hand panels show cut-outs of the reduced VLT Ks–band ISAAC images centred on the quasars. The centre panels show the best-fitting host-galaxy models without the nuclear component. The right-hand panels show the residual images produced by subtracting the best-fitting combined nuclear and host models from the original QSO image. All panels are $12.0'' \times 12.0''$. Images are displayed at 2.5σ above and 1σ below the median sky value.

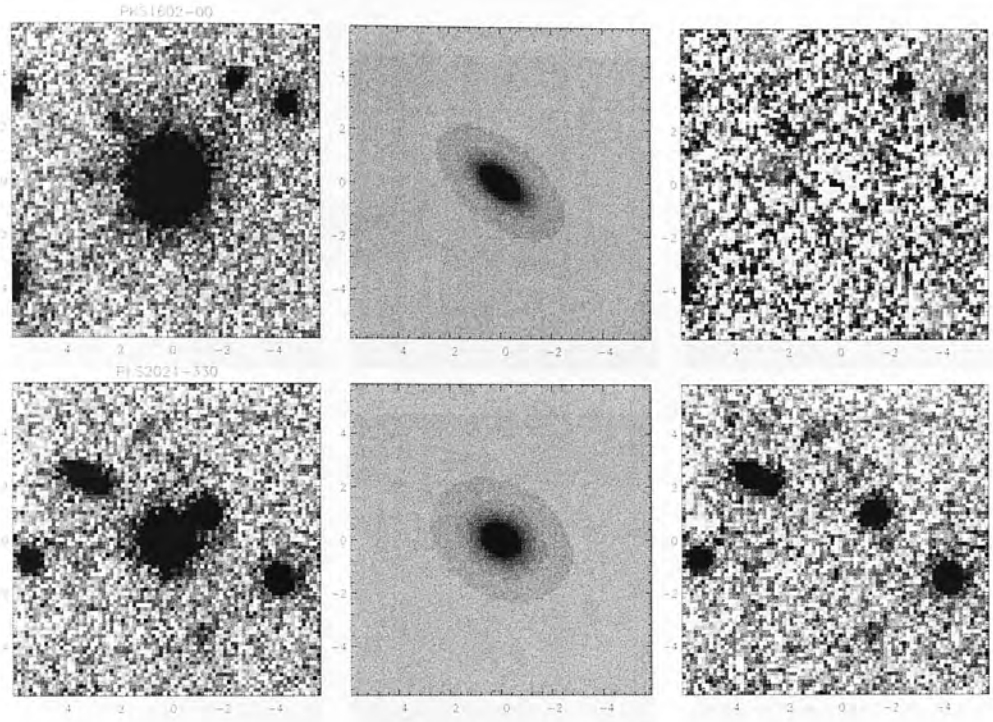

Figure 4.3: - continued

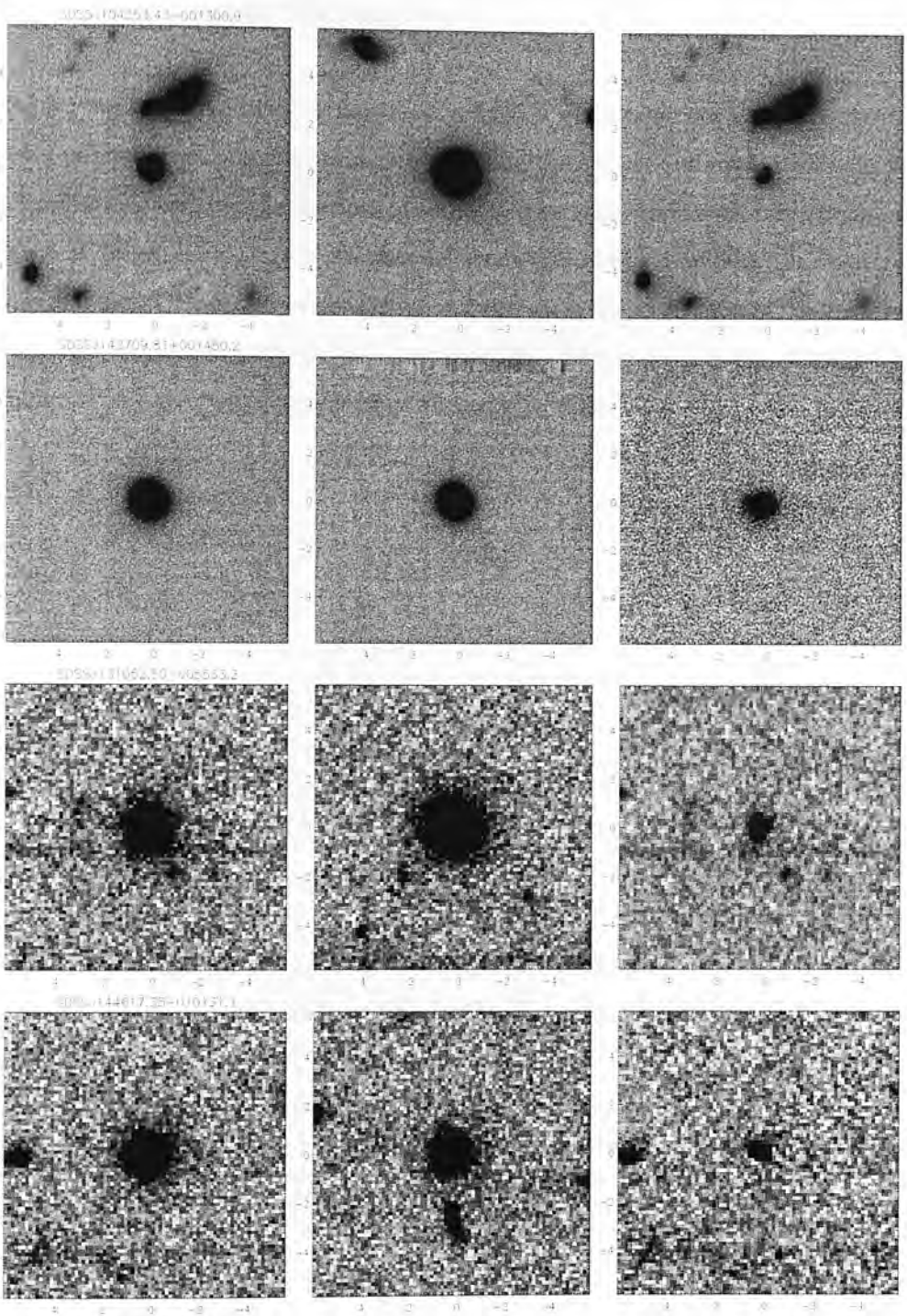

Figure 4.4: Reduced data and monotonic PSF-subtraction residual for the $z = 3,4$ quasar samples. The left-hand and central panels show cut-outs of the reduced Gemini (top pair) and VLT (bottom pair) images of the quasars and best-matched PSF star respectively. The right-hand panels show the residual images produced by subtracting the normalised PSF star to produce a monotonic residual. All panels are $12.0'' \times 12.0''$. Images are displayed at 2.5σ above and 1σ below the median sky value.

4.4 Infrared Hubble diagram

The infrared Hubble diagram for the $z = 1.5, 3, 4$ quasars before and after separation of nuclear and host contributions via two-dimensional modelling is shown in Figure 4.5. QSO host-galaxy magnitudes are found to be consistent with the formal best-fit to the 7CRS, 6CE, 6C, and 3CRR samples from Willott et al. (2003b). This consistency suggests that the quasar hosts are among the most massive galaxies in existence at these redshifts, given that the $K - z$ relation is believed to trace the envelope of the most massive galaxies in existence at all redshifts (Rocca-Volmerange et al. 2004).

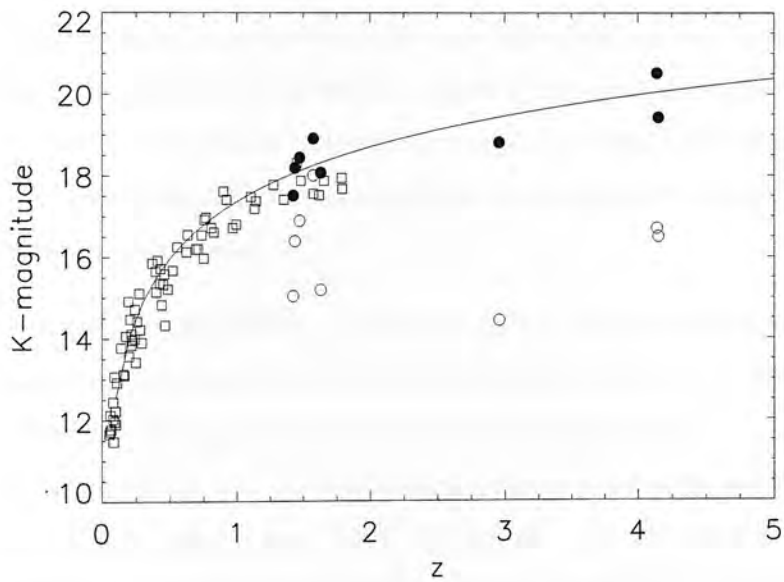

Figure 4.5: The infrared Hubble diagram for $z < 2$ 3CRR radio galaxies (Willott et al. 2003a) and $z = 1.5, 3, 4$ QSOs before (open circles) and after (filled circles) separation of nuclear and host contributions via two-dimensional modelling. Also shown is the best second-order polynomial fit to the 7CRS, 6CE, 6C, and 3CRR samples from Willott et al. The two $z \sim 1.5$ and one $z \sim 3$ QSOs with poorly matched PSF stars or inaccurate two-dimensional modelling results are excluded.

4.5 Quasar host-galaxy masses

Two techniques were used to convert host-galaxy luminosity to mass. An initial estimate was obtained using the Bruzual & Charlot (2003) GALAXEV code. Assuming a Salpeter initial mass function for an elliptical galaxy with solar metallicity formed at redshift 10 ($z_{form} = 10$), the GALAXEV code determines the expected apparent magnitude of $1\,M_{\odot}$ of material from $0 < z < z_{form}$. The total host-galaxy mass was determined using the offset between the total observed host flux and that of the $1\,M_{\odot}$ model. This technique is limited by the assumptions made when selecting the galaxy model. The z_{form} can be constrained by the time required to assemble a large black hole by accretion at the Eddington limit, typically taken to be $\sim$1 Gyr (e.g. Haiman & Loeb 2001). This assumes an initial low-mass black hole and a ~ 10 per cent efficiency in energy dissipation in the accretion system. This constraint does not substantially reduce the large number of potential formation redshifts, but does eliminate recent formation models in which significant stellar population evolution would heavily influence the resulting mass.

The second, more robust, galaxy-mass estimate was obtained via SED-fitting of stellar population models from Bruzual & Charlot (2003) at varying formation redshifts to the $K-$band photometry for the quasars. The range of z_{form} was constrained by the Eddington limit ~ 1 Gyr formation time for the central black hole. Although a single $K-$band point is insufficient to determine the actual SED of the host galaxy, this analysis can constrain the possible range of masses that the sources could possess. The $z_{form} = 10$ mass estimate was consistent with the upper limit of the mass range determined by SED fitting.

Host-galaxy fluxes and masses derived via monotonic PSF subtraction and two-dimensional modelling are presented in Table 4.6.

4.6 Quasar black hole masses

The black hole mass estimates for the quasar samples were calculated using the virial mass estimator. Spectra for the $z = 1.5$ sample included the broad H_β line at $\lambda_{rest} = 4861$Å (used to determine BLR velocity) and the quasar continuum at 5100Å (serving as a proxy for BLR radius). The SDSS spectra for the $z = 3, 4$ samples included the broad CIV at $\lambda_{rest} = 1549$Å and continuum data for 1350Å. Examples of SDSS and ISAAC continuum-normalised spectra are presented in Appendix B. Data were examined using SPLOT in IRAF. The spectra were smoothed with a boxcar algorithm, with absorption features and artificial noise peaks removed by linking neighbouring points astride the artifact. Emission linewidths were fit with a Gaussian profile and the FWHM recorded. Continuum fluxes at 1350Å and 5100Å were measured from the continuum fits. Where the global continuum fit was poor at the required wavelength, a section around the target wavelength was extracted and separately fit to provide the necessary data. Virial black hole mass estimators from Vestergaard & Peterson (2006) (Equation 4.1), and McLure & Jarvis (2002) (Equation 4.2) were used to determine black hole mass.

$$log\frac{M_{bh}}{\mathrm{M}_\odot} = log\left[\left(\frac{\lambda L_{1350}}{10^{44}\mathrm{ergs}^{-1}}\right)^{0.53}\left(\frac{FWHM(CIV)}{1000\mathrm{kms}^{-1}}\right)^2\right] + 6.66 \tag{4.1}$$

$$\frac{M_{bh}}{\mathrm{M}_\odot} = 4.74\left(\frac{\lambda L_{5100}}{10^{37}\mathrm{W}}\right)^{0.61}\left(\frac{FWHM(H_\beta)}{\mathrm{kms}^{-1}}\right)^2 \tag{4.2}$$

FWHM measurements in Å were corrected for $(1 + z)$ broadening to $z = 0$ and converted to 1000km s^{-1} and km s^{-1} units. Continuum fluxes were converted to luminosities using the standard flux/luminosity relationship (with consideration of the offset between observed flux and emitted luminosity), then converted to $10^{44}\mathrm{ergs}^{-1}$ and 10^{37}W units.

4.7 The M_{bh}/M_{bulge} relationship to z = 4

Host galaxy magnitudes derived from monotonic PSF subtraction and two-dimensional modelling, with the associated mass estimates from Bruzual & Charlot (2003) aperture-magnitude scaling (assuming $z_{form} = 10$), and the mass range from model SED fitting are presented in Table 4.6. These data are tabulated with black hole masses, as determined via Equations 4.1 and 4.2.

The derived $M_{bh} : M_{bulge}$ ratios for the $z = 3, 4$ quasars are shown in Figure 4.6, using the upper (left panel) and lower (right panel) host mass estimates from SED fitting. Despite the large separation expected in M_{bh}/M_{bulge} for the best-fit evolving and non-evolving models at $z = 3, 4$, consistency with either scenario cannot be ruled out given the range of potential host masses. However, given the young age of the universe at $z = 4$, it is likely that younger SED models (resulting in lower host masses and higher $M_{bh} : M_{bulge}$ ratios) provide a more accurate mass estimate for the $z = 3, 4$ quasars.

Also plotted in Figure 4.6 are M_{bh}/M_{bulge} data for: 3CRR galaxies from Chapter 3 with associated 1σ uncertainty, SDSS J1148+5251, and the results from Peng et al. (2006). The factor $3 - 6$ increase at $z \sim 2$ found by Peng et al. is in good agreement with the evolution found in Chapter 3. These data would suggest that at high redshift the $M_{bh} : M_{bulge}$ ratio does evolve with redshift as described be McLure et al. (2006).

We demonstrate that both black hole and host galaxy masses can be obtained for high-redshift quasars from emission linewidths and deep high-quality imaging. Clearly, multi-frequency information for SED fitting is necessary to constrain host-galaxy mass if accurate M_{bh}/M_{bulge} estimates are to be made. The suggested evolution of M_{bh}/M_{bulge} could be verified after data acquisition for the remaining quasars in the samples at $z = 3, 4$ in the near-infrared J, H, and $K-$bands.

Table 4.6: Details for quasar host galaxy and black hole mass estimates. Column 1 lists the source name. Column 2 lists the quasar magnitude from a 6-arcsec-diameter aperture. Columns 3 and 4 list quasar host galaxy magnitudes from monotonic PSF subtraction and two-dimensional modelling. Column 5 lists the stellar mass estimated by matching the two-dimensional model magnitude with a Bruzual & Charlot (2003) stellar population model, which undergoes an instantaneous burst of star formation at a formation redshift of $z_f = 10$. Columns 6 and 7 list the lower and upper values of the host-mass range determined via SED fitting. Column 8 lists the FWHM of the Gaussian fit to the H_{beta} ($z = 1.5$ QSOs) and CIV ($z = 3, 4$ QSOs) emission linewidths. Column 9 lists the continuum luminosity at 5100Å in $10^{37}W$ ($z = 1.5$ QSOs) and 1350Å in $10^{44}erg\,s^{-1}$ ($z = 3, 4$ QSOs). Column 10 lists the resulting estimate of the black hole mass.

Source	$K-$mag. (total)	$K-$mag. (monotonic)	$K-$mag. (model)	Ap. M_{bulge} (10^{11} $M_\odot$)	Min. M_{bulge} (10^{11} $M_\odot$)	Max. M_{bulge} (10^{11} $M_\odot$)	FWHM ($1000kms^{-1}$)	Contin. Lum.	M_{bh} (10^9 $M_\odot$)
PKS 1430−155	18.01	19.24	18.91	4.00	1.58	3.98	1.90	40.45	0.16
PKS 1532+01	16.39	18.36	18.19	6.66	2.51	6.31	3.43	38.99	0.52
PKS 1548+056	15.04	17.73	17.51	12.5	3.98	12.6	4.33	39.42	0.84
PKS 1602−00	15.19	18.45	18.07	9.29	3.16	10.0	3.32	39.83	0.49
PKS 2021−330	16.89	18.46	18.44	5.49	2.00	6.31	3.46	39.13	0.53
SDSS J104253.43	16.17	19.08	18.81	13.8	7.94	15.8	6.82	315.16	4.48
SDSS J131052.50	16.70	20.78	20.51	4.98	2.00	7.94	5.37	421.25	3.24
SDSS J144617.35	16.50	19.69	19.42	13.7	5.01	20,0	5.10	491.68	3.17

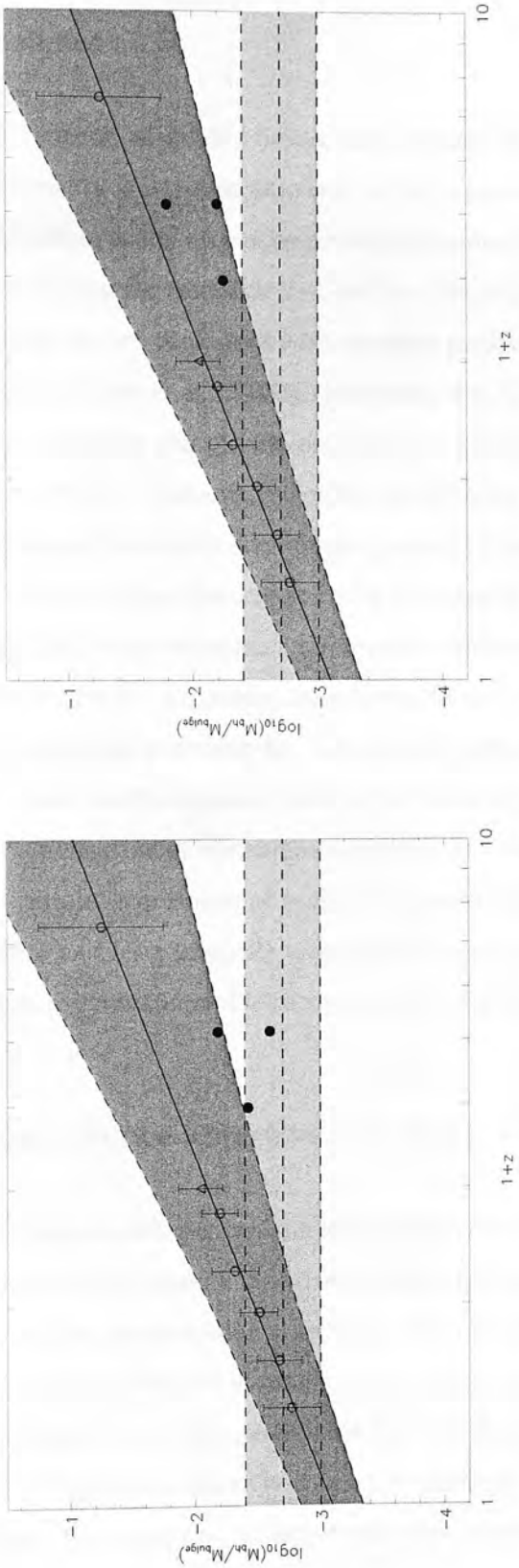

Figure 4.6: The M_{bh} : M_{bulge} estimates for $z = 3, 4$ quasars (filled circles) using the maximum (left panel) and minimum (right panel) mass estimates from SED fitting. The solid line shows the best fit to the observed evolution in 3CRR galaxies (open circles) from McLure et al. (2006), while the dark-grey shaded area shows the 1σ uncertainty of this fit. The light-grey shaded area illustrates the ± 0.3-dex uncertainty on the local M_{bh}/M_{bulge} ratio, centred on $M_{bh}/M_{bulge} = 0.002$.

4.7.1 Uncertainties

Accurate determination of quasar host-galaxy masses at high redshift with single waveband photometry is impracticable due to large uncertainties in the result. The $z = 1.5$ FSQ host-mass estimates can be considered more reliable, as the $K-$band observations are sampling the restframe $I-$band ($\sim 0.86\mu m$), and $K-$band magnitudes on the $K - z$ diagram are consistent with massive passively evolving galaxies from the 3CRR sample (Willott et al. 2003b). However, the $K-$band observations of the $z = 3$ and $z = 4$ quasars sample the restframe $V-$band ($\sim 0.55\mu m$) and $B-$band ($\sim 0.43\mu m$) respectively. These wavelengths are strongly susceptible to contamination from ongoing star-formation, likely to be present at these high redshifts given the young age (~ 1.5 Gyr) of the universe at $z = 4$. The bright $K-$band magnitudes (and correspondingly high mass estimates), apparently consistent with massive passively evolving sources in the $K - z$ diagram, could arise from star-formation contamination at these restframe optical wavelengths. An accurate estimate of quasar host mass at $z > 3$ would require multi-frequency data at rest wavelengths short and long of the 4000Å break and a measure of restframe magnitude at wavelengths longer than $1\mu m$. For the $z = 4$ sample, acquisition of such data would require high sensitivity, high spatial resolution, and long (mid-IR) wavelengths, a combination that may only be possible with future generations of telescope, such as the James Webb Space Telescope.

4.8 Original science objectives for the z = 1.5 QSO sample

At present, virial mass techniques are the only practical tool for M_{bh} estimation at high redshift. Although consistent with more robust black hole mass-estimation methods at low redshift – such as reverberation mapping – the use of broad-emission linewidth as a proxy for rotational velocity assumes a spherical BLR geometry, which is as yet unproven. We present $M_{bh} : M_{bulge}$ estimates for 5 flat-spectrum quasars at $z \sim 1.5$, in which the central engine is observed within $i < 7°$ (Jackson & Wall 1999), to determine whether the broad-line region is consistent with random orbital motion or a disk-like geometry.

4.9 BLR orientation

The well-established, orientation-dependent unification picture of AGN (e.g. Barthel 1989; Antonucci 1993) has now been in place for well over a decade. Constraining source orientation through the use of radio data has played a crucial role in the development of the unified model (Urry & Padovani 1995). Under this scheme, AGN with radio jets directed along the observer's line of sight are seen as flat-spectrum radio-loud quasars (FSQs) with a radio spectral index $\alpha_{rad} < 0.5$. The flat spectrum is believed to arise from the superposition of many relativistically beamed synchrotron self-absorbed spectra. FSQ hosts are unresolved in optical imaging, while the optical spectra are dominated by nuclear light and associated broad permitted emission lines (FWHM $>$ 2000km s^{-1}) typical of quasars. High-frequency ($\nu > 1$ GHz) radio surveys (e.g. Drinkwater et al. 1997) preferentially select FSQs whose radio emission does not become fainter at high frequencies, as is observed in optically thin synchrotron sources.

In AGN with radio jets aligned along the plane of the sky, the dominant radio emission arises from the optically thin lobes that can extend up to Mpc scales from the central engine. The radio spectra of the lobes are predominantly steep, with $\alpha_{rad} > 0.5$. Such sources typically possess only narrow emission lines (FWHM $<$ 2000km s^{-1}) that are believed to arise from beyond the obscuring torus. Host galaxies are found to be similar to quiescent ellipticals, usually with some extended line emission in the direction of the radio jets, consistent with the so-called alignment effect (e.g. van Breugel, Heckman & Miley 1984; Inskip et al. 2002). These sources are classified as radio galaxies, which are typically found in low-frequency radio surveys, such as the 3CRR (Laing, Riley & Longair 1983), 6CE (Eales et al. 1997), 7CRS (Willott et al. 2002) and the Westerbork Northern Sky Survey (Rengelink et al. 1997).

Where source inclination falls between the edge-on and face-on regimes, i.e. the jets lie at an angle $< 45°$ (e.g. Barthel 1989) to the line of sight, both the broad emission lines and some contribution from the flat-spectrum core are visible. However, there is also a large contribution from the large-scale steep-spectrum radio lobes. The total radio spectra are found to be somewhere between the flat-spectrum, core-

dominated sources and the core-less, lobe-dominated radio galaxies and can thus exhibit both components. These sources are known as steep-spectrum radio-loud quasars (SSQs).

Total radio spectral index is therefore an indicator of source orientation to the observer's line of sight. This view is consistent with another quasar-orientation estimator based on the strength of the core radio emission compared with the extended emission (e.g. Wills & Browne 1986; Brotherton 1996). However, uncertainty in orientation using such core-to-lobe radio measurements is high. Under the unification model, FSQ inclinations are well constrained to $i < 7°$, and hence most susceptible to potential BLR inclination effects.

4.10 BLR inclination

The basic premise of virial mass techniques is that the dominant mechanism responsible for the width of the broad emission lines is the gravitational potential of the central black hole, and that the linewidths reflect the Keplerian velocities of the line-emitting material (e.g. Peterson & Wandel 2000). If this assumption is valid, then the so-called virial mass estimate for the central black hole is represented by

$$M_{bh} = G^{-1} R_{BLR} V_{BLR}^2 \tag{4.3}$$

where R_{BLR} is the radius of the BLR and V is the velocity of the line-emitting material. However, if the BLR possesses a disk-like morphology (as opposed to the spherical one assumed in Equation 4.3), a factor f (see Equation 4.4, where i represents source inclination) is introduced, linking the observed FWHM to the intrinsic velocity of the line-emitting material (McLure & Dunlop 2002).

$$f = 1/(2 \sin i) \tag{4.4}$$

The literature contains substantial evidence that the FWHM of broad emission lines are inclination-dependent in radio-loud AGNs (e.g. Wills & Browne 1986; Brotherton

1996; Corbin 1997; Vestergaard, Wilkes & Barthel 2000). Recently, Jarvis & McLure (2006) used a well-defined sample of RLQs, SSQs, and RQQs to investigate the dependence of the observed broad linewidths on orientation. H_β linewidths were found to be significantly broader in SSQs than in FSQs or RQQs. However, as the FSQs and RQQ broad-linewidth distributions were also found to be the same, the authors posit that this similarity can be explained within unified schemes if a substantial fraction of the flat-spectrum sources is composed of Doppler-boosted RQQs. It has been argued that RQQs contain less-massive black holes than their radio-loud counterparts (Laor (2000), McLure & Dunlop (2001). If so, then potential orientation effects from the BLR could not be decoupled from a potential difference in black hole masses between FSQs and SSQs. The M_{bh}/M_{bulge} relationship is used to determine whether virial mass estimators are biased by orientation, independent of potential differences in M_{bh} between populations of galaxies.

4.11 The black hole to bulge mass ratio and inclination

Figure 4.7 shows the $M_{bh} : M_{bulge}$ ratio for the $z = 1.5$ FSQs, where the data point is $< log(M_{bh}/\mathrm{M}_\odot) > - < log(M_{bulge}/\mathrm{M}_\odot) >$ for the 5 quasars, and errors estimated by assuming ± 0.3-dex (Vestergaard & Peterson 2006) and ± 0.4-dex (McLure et al. 2006) uncertainty in black hole and host galaxy masses respectively as seen in the literature. M_{bulge} was taken to be the midpoint of the mass range determined by SED fitting to the $K-$band magnitude. The FSQs were found to have an average M_{bh}/M_{bulge} of ~ 0.0007, a factor of ~ 3 smaller than the 0.002 established for local galaxies, and a factor of ~ 7 smaller than the evolving estimate from McLure et al. (2006).

For low-frequency selected quasar samples such as the 3CRR, the QSO are consistent with being confined to $i < 45°$ (Barthel 1989), leading to an average value of $i \sim 30$ and hence $f = 1$. However, comparing the FSQ result with the non-evolving evolutionary track in Figure 4.7, the factor ~ 3 decrease in M_{bh} implies an average value of $i \sim 17°$. However, the factor 7.83 separation between the FSQs and the evolving McLure et al. (2006) ratio suggests an average inclination of $i \sim 10°$, which is in

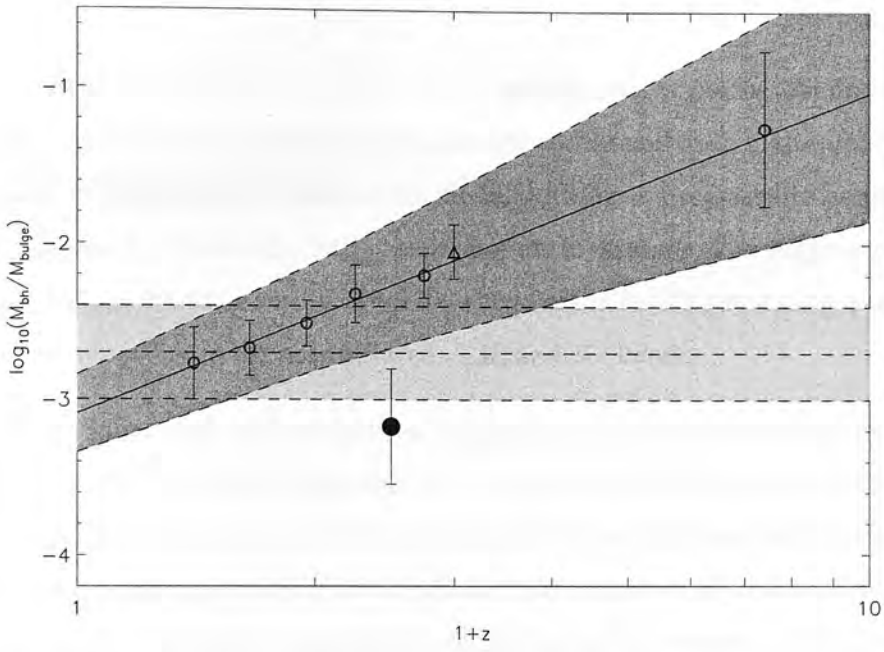

Figure 4.7: The M_{bh} : M_{bulge} estimate for $z = 1.5$ flat-spectrum quasars using the mid-point of the mass estimates from SED fitting. The filled circle is $< log(M_{bh}/\mathrm{M}_{\odot}) > - < log(M_{bulge}/\mathrm{M}_{\odot}) >$ for the 5 quasars. The solid line shows the best fit to the observed evolution in 3CRR galaxies (open circles) from McLure et al. (2006), while the dark-grey shaded area shows the 1σ uncertainty of this fit. The light-grey shaded area illustrates the ± 0.3-dex uncertainty on the local M_{bh}/M_{bulge} ratio, centred on $M_{bh}/M_{bulge} = 0.002$.

good agreement with the expected ($i \sim 7°$) value for FSQs from Jackson & Wall (1999). These data suggest that the BLR of AGN possess a disk-like morphology, whose observed broad linewidths are dependent upon orientation to the observer.

4.12 Summary

It is shown that both black hole and host galaxy masses can be obtained for high-redshift quasars in the SDSS from emission linewidths and deep high-quality imaging. Clearly, multi-frequency information for SED fitting is necessary to constrain host-galaxy mass if accurate M_{bh}/M_{bulge} estimates are to be made. The suggested evolution of M_{bh}/M_{bulge} could be verified after data acquisition for the remaining quasars in the samples at $z = 3, 4$ in the near-infrared J, H, and $K-$bands.

It was found that the host galaxies of bright $z = 1.5$ flat-spectrum quasars are large ($< r_{1/2} >= 4.1 \pm 1.0\,\mathrm{kpc}$) ellipticals ($< n >= 4.2 \pm 0.8$). The $M_{bh} : M_{bulge}$ ratio for the FSQs was found to be ~ 0.0007, a factor of ~ 3 smaller than the 0.002 established for local galaxies and a factor of ~ 7 smaller than the evolving estimate from McLure et al. (2006). These data suggest that the BLR of AGN possess a disk-like morphology, whose observed broad linewidths are dependent upon source orientation to the observer.

Given the uncertainties involved in determining black hole and galaxy masses with virial techniques and single-waveband SED fitting respectively, these conclusions must be regarded as preliminary in nature. However, the success of the techniques employed, and the results obtained, clearly indicate that further and ongoing data acquisition could provide a robust measurement of AGN host-galaxy masses at high redshift.

CHAPTER 5

Conclusions

The results of this thesis are summarised in each chapter. Following the pilot program described in Chapter 4, new data from the ongoing observational program (Figure 4.1) to constrain $M_{bh} : M_{bulge}$ ratio evolution at $z = 2, 3, 4$ will be taken.

In Chapter 2 the hosts of the brightest radio sources in 3CRR catalog at $z \sim 2$ were found have surface brightness distributions consistent with those expected for classic ellipticals, demonstrating that massive early-type galaxies are in place at this high redshift. The half-light radii of these sources were found to be, on average, a factor ~ 2 smaller than the $z < 1$ 3CRR radio galaxies from McLure et al. (2004). These radio hosts represent some of the most massive galaxies in place at $z \sim 2$, implying that they are the progenitors of the most massive galaxies at $z = 0$. It can be argued that passive evolution alone could account for the difference in $K-$band magnitude between the $z \sim 2$ and $z \sim 0$ radio hosts, as indicated by the infrared Hubble diagram. This assessment would seem to be supported by the similarity of 3C-type radio galaxy scalelengths for $0 < z < 1$ sources. However, passive evolution alone cannot account for the approximate factor-of-two decrease found in $r_{1/2}$ of the $z \sim 2$ radio hosts. By implication, the $z \sim 2$ radio galaxies would need to undergo major mergers to relax their $r_{1/2}$ to local values. The low submm flux of 3CRR hosts suggests that dry

merging is responsible for the observed size evolution. This discovery is consistent with a hierarchical merging view of galaxy evolution, with massive compact galaxies growing in size via dry mergers over cosmic time.

The submillimetre hosts were found to be disk galaxies, possessing half-light radii consistent with the most massive known disks of stars at high redshift. The luminosities of the submillimetre galaxies are ~ 1.5 magnitudes brighter than Lyman-break galaxies at comparable redshifts, indicating that submillimetre galaxies are significantly more massive. Chapter 2 strongly supports the view of submm galaxies as the progenitors of today's massive ellipticals. Specifically, surface-mass densities for both the submm hosts and $z \sim 2$ radio galaxies were found to be consistent with quiescent elliptical galaxies at high redshift, and not star-forming or Lyman-break galaxies. However, it must be noted that whereas the radio galaxies are a complete sample of the most radio-luminous objects in the redshift range $1.5 < z < 2.5$, the submm sources are drawn solely from a 260 arcmin^2 field. Consequently, the nature of these SCUBA galaxies may differ from the most luminous submm objects detected in subsequent surveys. New data from the next generation of submm instruments will allow direct comparison of massive ellipticals at high redshift, with the brightest submm sources located in large-area submm surveys.

In Chapter 3, the 3CRR sample of radio-loud active galactic nuclei was used to investigate the evolution of the black-hole:spheroid mass ratio in the most massive early-type galaxies from $0 < z < 2$. Radio-loud unification was exploited to obtain virial black hole mass estimates from the 3CRR quasars, and stellar mass estimates from the 3CRR radio galaxies, thereby providing black hole and stellar mass estimates for a single population of early-type galaxies. At low redshift ($z \lesssim 1$) the 3CRR sample is consistent with a black-hole:spheroid mass ratio of $M_{bh}/M_{bulge} \simeq 0.002$, in good agreement with that observed locally for quiescent galaxies of similar stellar mass ($M_{bulge} \simeq 5 \times 10^{11}\,\mathrm{M}_{\odot}$). However, over the redshift interval $0 < z < 2$ the 3CRR black-hole:spheroid mass ratio was found to evolve as $M_{bh}/M_{bulge} \propto (1+z)^{2.07\pm0.76}$, reaching $M_{bh}/M_{bulge} \simeq 0.008$ by redshift $z \simeq 2$. If confirmed, the detection of evolution in the 3CRR black-hole:spheroid mass ratio further strengthens the evidence that, at least for

massive early-type galaxies, the growth of the central supermassive black hole may be completed before that of the host spheroid.

Chapter 4 demonstrates that both host spheroid and black hole mass can be obtained from deep near-infrared imaging and optical spectra out to $z \sim 4$. The $K-$band magnitudes for the $z \sim 3$ and $z \sim 4$ galaxies were found to be consistent with the brightest galaxies expected in the infrared Hubble diagram. However, accurate determination of quasar host-galaxy masses at high redshift with single waveband photometry was impracticable due to significant uncertainties in the results. Given the success of the pilot program, multi-frequency data for the existing and remaining $z = 3, 4$ targets in the J, H and $K-$bands could provide the first statistically significant sample capable of constraining the evolution of the $M_{bh} : M_{bulge}$ ratio to $z = 4$.

The low $M_{bh} : M_{bulge}$ ratio of the five flat-spectrum quasars suggests that the BLR of AGN (used to estimate M_{bh}) possesses a disk-like morphology. However, data for a larger sample of FSQs is required to corroborate these results. Additionally, under the current unification scheme, broad-line radio galaxies could be used to sample AGN restricted to a more edge-on viewing angle, from which both host and black hole masses could be obtained. These sources should possess $M_{bh} : M_{bulge}$ ratios greater than that observed in quasars if M_{bh} estimates from virial techniques are orientation-dependent.

Much of the work in the thesis has been conducted at the limits of ground-based resolution. Consequently, the scope of the results presented has been limited both by the angular resolution currently achievable at $2.2\,\mu$m and by the lack of wide-area imaging at submm wavelengths. The first of these restrictions is currently being removed with the advent of laser-adaptive optic systems, and will ultimately be revolutionised by the JWST in 2013. The second limitation should be overcome in the next few years with the advent of deep wide-area submm imaging with SCUBA2 on the JCMT. Nevertheless, the results presented here clearly demonstrate the potential of high-resolution near-infrared imaging to clarify our picture of galaxy formation and evolution.

Bibliography

Aars C.E., Hough D.H., Yu L.H., Linick J.P., Beyer P.J., Vermeulen R.C., Readhead A.C.S., 2005, AJ, 130, 23

Aguilar L.A., Merritt D., 1990, ApJ, 354, 33

Aldcroft T., Elvis M., Bechtold J., 1994, In Bulletin of the American Astronomical Society, pp. 1337–+

Almaini O., Dunlop J.S., Conselice C.J., Targett T.A., Mclure R.J., 2005, ArXiv Astrophysics e-prints

Almaini O., et al., 2003, MNRAS, 338, 303

Antonucci R., 1993, ARA&A, 31, 473

Archibald E.N., Dunlop J.S., Hughes D.H., Rawlings S., Eales S.A., Ivison R.J., 2001, MNRAS, 323, 417

Archibald E.N., Dunlop J.S., Jimenez R., Friaça A.C.S., McLure R.J., Hughes D.H., 2002, MNRAS, 336, 353

Aretxaga I., Hughes D.H., Dunlop J.S., 2005, MNRAS, 358, 1240

Aretxaga I., Hughes D.H., Dunlop J.S., 2007, ArXiv Astrophysics e-prints

Arimoto N., Yoshii Y., 1987, A&A, 173, 23

Baldry I.K., Balogh M.L., Bower R., Glazebrook K., Nichol R.C., 2004, In Allen R.E., Nanopoulos D.V., Pope C.N., eds., The New Cosmology: Conference on Strings and Cosmology, vol. 743 of American Institute of Physics Conference Series, pp. 106–119

Barth A.J., Martini P., Nelson C.H., Ho L.C., 2003, ApJ, 594, L95

Barthel P., 1989, Scientific American, 260, 20

Barthel P.D., Tytler D.R., Thomson B., 1990, A&AS, 82, 339

Baugh C.M., Lacey C.G., Frenk C.S., Granato G.L., Silva L., Bressan A., Benson A.J., Cole S., 2005, MNRAS, 356, 1191

Bell E.F., et al., 2004, ApJ, 608, 752

Best P., Longair M., Rottgering H., 1997, In da Costa L.N., Renzini A., eds., Galaxy Scaling Relations: Origins, Evolution and Applications, pp. 232–+

Best P.N., Longair M.S., Roettgering H.J.A., 1998, MNRAS, 295, 549

Best P.N., Röttgering H.J.A., Lehnert M.D., 1999, MNRAS, 310, 223

Bettoni D., Falomo R., Fasano G., Govoni F., Salvo M., Scarpa R., 2003, In Bender R., Renzini A., eds., The Mass of Galaxies at Low and High Redshift, pp. 154–+

Blanton M.R., et al., 2001, AJ, 121, 2358

Bower R.G., Benson A.J., Malbon R., Helly J.C., Frenk C.S., Baugh C.M., Cole S., Lacey C.G., 2006, MNRAS, 370, 645

Bressan A., Chiosi C., Fagotto F., 1994, ApJS, 94, 63

Brotherton M.S., 1996, ApJS, 102, 1

Bruzual G., Charlot S., 2003, MNRAS, 344, 1000

Capaccioli M., 1989, In Corwin Jr. H.G., Bottinelli L., eds., World of Galaxies (Le Monde des Galaxies), pp. 208–227

Caputi K.I., Dunlop J.S., McLure R.J., Roche N.D., 2004, MNRAS, 353, 30

Caputi K.I., et al., 2006, ApJ, 637, 727

Chapman S.C., Windhorst R., Odewahn S., Yan H., Conselice C., 2003, ApJ, 599, 92

Chapman S.C., Blain A.W., Smail I., Ivison R.J., 2005, ApJ, 622, 772

Cimatti A., Andreani P., Röttgering H., Tilanus R., 1998, Nature, 392, 895

Cimatti A., Daddi E., Renzini A., 2006, A&A, 453, L29

Cimatti A., et al., 2002, A&A, 381, L68

Conselice C.J., 2003, ApJS, 147, 1

Coppin K., et al., 2006, MNRAS, 372, 1621

Corbin M.R., 1997, ApJS, 113, 245

Cowie L.L., Songaila A., Hu E.M., Cohen J.G., 1996, AJ, 112, 839

Croton D.J., 2006, MNRAS, 369, 1808

Daddi E., Cimatti A., Renzini A., 2000, A&A, 362, L45

Daddi E., Cimatti A., Renzini A., Fontana A., Mignoli M., Pozzetti L., Tozzi P., Zamorani G., 2004, ApJ, 617, 746

Daddi E., et al., 2005, ApJ, 626, 680

De Breuck C., van Breugel W., Stanford S.A., Röttgering H., Miley G., Stern D., 2002, AJ, 123, 637

De Lucia G., Springel V., White S.D.M., Croton D., Kauffmann G., 2006, MNRAS, 366, 499

de Vaucouleurs G., 1959, Handbuch der Physik, 53, 275

de Vries W.H., O'Dea C.P., Barthel P.D., Fanti C., Fanti R., Lehnert M.D., 2000, AJ, 120, 2300

Dey A., Graham J.R., Ivison R.J., Smail I., Wright G.S., Liu M.C., 1999, ApJ, 519, 610

Dickinson M., GOODS Team, 2004, In Bulletin of the American Astronomical Society, pp. 701–+

Djorgovski S., Davis M., 1987, ApJ, 313, 59

Draine B.T., Lee H.M., 1984, ApJ, 285, 89

Dressler A., Lynden-Bell D., Burstein D., Davies R.L., Faber S.M., Terlevich R., Wegner G., 1987, ApJ, 313, 42

Drinkwater M.J., Francis P.J., Webster R.L., 1997, In Peterson B.M., Cheng F.Z., Wilson A.S., eds., ASP Conf. Ser. 113: IAU Colloq. 159: Emission Lines in Active Galaxies: New Methods and Techniques, pp. 437–+

Drory N., Bender R., Feulner G., Hopp U., Maraston C., Snigula J., Hill G.J., 2004, ApJ, 608, 742

Drory N., Salvato M., Gabasch A., Bender R., Hopp U., Feulner G., Pannella M., 2005, ApJ, 619, L131

Dunlop J., Peacock J., Spinrad H., Dey A., Jimenez R., Stern D., Windhorst R., 1996, Nature, 381, 581

Dunlop J.S., Peacock J.A., 1993, MNRAS, 263, 936

Dunlop J.S., Hughes D.H., Rawlings S., Eales S.A., Ward M.J., 1994, Nature, 370, 347

Dunlop J.S., McLure R.J., Kukula M.J., Baum S.A., O'Dea C.P., Hughes D.H., 2003, MNRAS, 340, 1095

Eales S., Rawlings S., Law-Green D., Cotter G., Lacy M., 1997, MNRAS, 291, 593

Eggen O.J., Lynden-Bell D., Sandage A.R., 1962, ApJ, 136, 748

Elston R., Rieke G.H., Rieke M.J., 1988, ApJ, 331, L77

Faber S.M., Huang J.S., Noeske K.G., Bundy K., DEEP2 Team, IRAC GTO Team, Palomar K-band Team, 2005, In Bulletin of the American Astronomical Society, vol. 37 of Bulletin of the American Astronomical Society, pp. 1298–+

Fan X., et al., 2003, AJ, 125, 1649

Fanaroff B.L., Riley J.M., 1974, MNRAS, 167, 31P

Ferrarese L., Merritt D., 2000, ApJ, 539, L9

Ferrarese L., Pogge R.W., Peterson B.M., Merritt D., Wandel A., Joseph C.L., 2001, ApJ, 555, L79

Feulner G., Gabasch A., Salvato M., Drory N., Hopp U., Bender R., 2005, ApJ, 633, L9

Floyd D.J.E., Kukula M.J., Dunlop J.S., McLure R.J., Miller L., Percival W.J., Baum S.A., O'Dea C.P., 2004, MNRAS, 355, 196

Fontana A., et al., 2004, A&A, 424, 23

Franx M., et al., 2003, ApJ, 587, L79

Gebhardt K., et al., 2000, ApJ, 539, L13

Genzel R., Eckart A., Ott T., Eisenhauer F., 1997, MNRAS, 291, 219

Glazebrook K., Peacock J.A., Collins C.A., Miller L., 1994, MNRAS, 266, 65

Glazebrook K., et al., 2004, Nature, 430, 181

Granato G.L., De Zotti G., Silva L., Bressan A., Danese L., 2004, ApJ, 600, 580

Greve T.R., Ivison R.J., Bertoldi F., Stevens J.A., Dunlop J.S., Lutz D., Carilli C.L., 2004, MNRAS, 354, 779

Haardt F., Maraschi L., 1993, ApJ, 413, 507

Haiman Z., Loeb A., 2001, ApJ, 552, 459

Häring N., Rix H.W., 2004, ApJ, 604, L89

Harms R.J., et al., 1994, ApJ, 435, L35

Heavens A., Panter B., Jimenez R., Dunlop J., 2004, Nature, 428, 625

Hewitt A., Burbidge G., 1991, ApJS, 75, 297

Holland W.S., Cunningham C.R., Gear W.K., Jenness T., Laidlaw K., Lightfoot J.F., Robson E.I., 1998, In Phillips T.G., ed., Proc. SPIE Vol. 3357, p. 305-318, Advanced Technology MMW, Radio, and Terahertz Telescopes, Thomas G. Phillips; Ed., pp. 305–318

Hozumi S., Burkert A., Fujiwara T., 2000, MNRAS, 311, 377

Hubble E.P., 1926, ApJ, 64, 321

Hughes D.H., et al., 1998, Nature, 394, 241

Inskip K.J., Best P.N., Rawlings S., Longair M.S., Cotter G., Röttgering H.J.A., Eales S., 2002, MNRAS, 337, 1381

Ivison R.J., et al., 2002, MNRAS, 337, 1

Ivison R.J., et al., 2005, MNRAS, 364, 1025

Jackson C.A., Wall J.V., 1999, MNRAS, 304, 160

Jackson N., Browne I.W.A., 1991, MNRAS, 250, 414

Jarvis M.J., McLure R.J., 2006, MNRAS, 369, 182

Jarvis M.J., Rawlings S., Eales S., Blundell K.M., Bunker A.J., Croft S., McLure R.J., Willott C.J., 2001, MNRAS, 326, 1585

Jarvis M.J., Wilman R.J., Röttgering H.J.A., Binette L., 2003, MNRAS, 338, 263

Kaspi S., Smith P.S., Netzer H., Maoz D., Jannuzi B.T., Giveon U., 2000, ApJ, 533, 631

Kauffmann G., Haehnelt M., 2000, MNRAS, 311, 576

Khochfar S., Silk J., 2006, ApJ, 648, L21

Kormendy J., 1977, ApJ, 217, 406

Kormendy J., Richstone D., 1995, ARA&A, 33, 581

Kristian J., 1973, ApJ, 179, L61

Krolik J.H., 2001, ApJ, 551, 72

Kukula M.J., Dunlop J.S., McLure R.J., Miller L., Percival W.J., Baum S.A., O'Dea C.P., 2001, MNRAS, 326, 1533

Labbé I., et al., 2003, ApJ, 591, L95

Laing R.A., Riley J.M., Longair M.S., 1983, MNRAS, 204, 151

Lane K.P., et al., 2007, MNRAS, pp. L55+

Laor A., 2000, ApJ, 543, L111

Larson R.B., 1975, MNRAS, 173, 671

Lawrence C.R., Zucker J.R., Readhead A.C.S., Unwin S.C., Pearson T.J., Xu W., 1996, ApJS, 107, 541

Lilly S.J., Longair M.S., 1984, MNRAS, 211, 833

Londrillo P., Messina A., Stiavelli M., 1991, MNRAS, 250, 54

Longhetti M., et al., 2007, MNRAS, 374, 614

Lynden-Bell D., 1969, Nature, 223, 690

Madau P., Ferguson H.C., Dickinson M.E., Giavalisco M., Steidel C.C., Fruchter A., 1996, MNRAS, 283, 1388

Magorrian J., et al., 1998, AJ, 115, 2285

Mannucci F., Basile F., Poggianti B.M., Cimatti A., Daddi E., Pozzetti L., Vanzi L., 2001, MNRAS, 326, 745

Marconi A., Hunt L.K., 2003, ApJ, 589, L21

Marziani P., Sulentic J.W., Zwitter T., Dultzin-Hacyan D., Calvani M., 2001, ApJ, 558, 553

May A., van Albada T.S., 1984, MNRAS, 209, 15

McGlynn T.A., 1984, ApJ, 281, 13

McLean I.S., Chuter T.C., McCaughrean M.J., Rayner J.T., 1986, In Crawford D.L., ed., Instrumentation in astronomy VI; Proceedings of the Meeting, Tucson, AZ, Mar. 4-8, 1986. Part 2 (A87-36376 15-35). Bellingham, WA, Society of Photo-Optical Instrumentation Engineers, 1986, p. 430-437., pp. 430–437

McLure R.J., Dunlop J.S., 2000, MNRAS, 317, 249

McLure R.J., Dunlop J.S., 2001, MNRAS, 327, 199

McLure R.J., Dunlop J.S., 2002, MNRAS, 331, 795

McLure R.J., Dunlop J.S., 2004, MNRAS, 352, 1390

McLure R.J., Jarvis M.J., 2002, MNRAS, 337, 109

McLure R.J., Kukula M.J., Dunlop J.S., Baum S.A., O'Dea C.P., Hughes D.H., 1999, MNRAS, 308, 377

McLure R.J., Dunlop J.S., Kukula M.J., 2000, MNRAS, 318, 693

McLure R.J., Willott C.J., Jarvis M.J., Rawlings S., Hill G.J., Mitchell E., Dunlop J.S., Wold M., 2004, MNRAS, 351, 347

McLure R.J., Jarvis M.J., Targett T.A., Dunlop J.S., Best P.N., 2006, MNRAS, 368, 1395

Moran J.M., Sub-Millimeter Array Team, 2001, In Bulletin of the American Astronomical Society, pp. 1468–+

Mortier A.M.J., et al., 2005, MNRAS, 363, 563

Mushotzky R., 2004, Kluwer Academic Publishers, ISBN 1-4020-2470-3

Nelson C.H., Green R.F., Bower G., Gebhardt K., Weistrop D., 2004, ApJ, 615, 652

Nipoti C., Londrillo P., Ciotti L., 2003, MNRAS, 342, 501

Onken C.A., Peterson B.M., 2002, ApJ, 572, 746

Papovich C., Dickinson M., Ferguson H.C., 2001, ApJ, 559, 620

Peng C.Y., Impey C.D., Ho L.C., Barton E.J., Rix H.W., 2006, ApJ, 640, 114

Pentericci L., McCarthy P.J., Röttgering H.J.A., Miley G.K., van Breugel W.J.M., Fosbury R., 2001, ApJS, 135, 63

Peterson B.M., 1997, Cambridge University Press, ISBN 0521479118

Peterson B.M., Wandel A., 2000, ApJ, 540, L13

Pope A., Borys C., Scott D., Conselice C., Dickinson M., Mobasher B., 2005, MNRAS, 358, 149

Pozzetti L., et al., 2003, A&A, 402, 837

Pozzetti L., et al., 2007, ArXiv e-prints, 704

Press W., 1992, Cambridge University Press, ISBN 0521437202

Rengelink R.B., Tang Y., de Bruyn A.G., Miley G.K., Bremer M.N., Roettgering H.J.A., Bremer M.A.R., 1997, A&AS, 124, 259

Renzini A., 2007, ArXiv Astrophysics e-prints

Rigopoulou D., et al., 2006, ApJ, 648, 81

Robertson B., Hernquist L., Cox T.J., Di Matteo T., Hopkins P.F., Martini P., Springel V., 2006, ApJ, 641, 90

Rocca-Volmerange B., Le Borgne D., De Breuck C., Fioc M., Moy E., 2004, A&A, 415, 931

Salpeter E.E., 1964, ApJ, 140, 796

Saracco P., Giallongo E., Cristiani S., D'Odorico S., Fontana A., Iovino A., Poli F., Vanzella E., 2001, A&A, 375, 1

Saracco P., et al., 2003, A&A, 398, 127

Saracco P., et al., 2005, MNRAS, 357, L40

Saracco P., et al., 2006, MNRAS, 367, 349

Sawicki M., Yee H.K.C., 1998, AJ, 115, 1329

Schmidt M., Green R.F., 1983, ApJ, 269, 352

Scott S.E., et al., 2002, MNRAS, 331, 817

Serjeant S., Rawlings S., Lacy M., Maddox S.J., Baker J.C., Clements D., Lilje P.B., 1998, MNRAS, 294, 494

Sersic J.L., 1968, Atlas de galaxias australes. Cordoba, Argentina: Observatorio Astronomico, 1968

Shapley A.E., Steidel C.C., Adelberger K.L., Dickinson M., Giavalisco M., Pettini M., 2001, ApJ, 562, 95

Shen S., Mo H.J., White S.D.M., Blanton M.R., Kauffmann G., Voges W., Brinkmann J., Csabai I., 2003, MNRAS, 343, 978

Smail I., Chapman S.C., Ivison R.J., Blain A.W., Takata T., Heckman T.M., Dunlop J.S., Sekiguchi K., 2003, MNRAS, 342, 1185

Smail I., Chapman S.C., Blain A.W., Ivison R.J., 2004, ApJ, 616, 71

Smith E.P., Heckman T.M., Bothun G.D., Romanishin W., Balick B., 1986, ApJ, 306, 64

Soifer B.T., Matthews K., Neugebauer G., Armus L., Cohen J.G., Persson S.E., Smail I., 1999, AJ, 118, 2065

Spinrad H., Marr J., Aguilar L., Djorgovski S., 1985, PASP, 97, 932

Steidel C.C., Giavalisco M., Pettini M., Dickinson M., Adelberger K.L., 1996, ApJ, 462, L17+

Steidel C.C., Adelberger K.L., Giavalisco M., Dickinson M., Pettini M., 1999, ApJ, 519, 1

Stockton A., Canalizo G., Maihara T., 2004, ApJ, 605, 37

Thomas D., Maraston C., Bender R., Mendes de Oliveira C., 2005, ApJ, 621, 673

Toomre A., 1977, ARA&A, 15, 437

Tremaine S., et al., 2002, ApJ, 574, 740

Trenti M., 2005, In Bulletin of the American Astronomical Society, vol. 37 of Bulletin of the American Astronomical Society, pp. 1314–+

Udry S., 1993, A&A, 268, 35

Urry C.M., Padovani P., 1995, PASP, 107, 803

van Albada T.S., 1982, MNRAS, 201, 939

van Breugel W., Heckman T., Miley G., 1984, ApJ, 276, 79

van Dokkum P.G., 2005, AJ, 130, 2647

van Dokkum P.G., et al., 2003, ApJ, 587, L83

Vestergaard M., 2002, ApJ, 571, 733

Vestergaard M., Peterson B.M., 2006, ApJ, 641, 689

Vestergaard M., Wilkes B.J., Barthel P.D., 2000, ApJ, 538, L103

Walter F., Carilli C., Bertoldi F., Menten K., Cox P., Lo K.Y., Fan X., Strauss M.A., 2004, ApJ, 615, L17

Wandel A., Peterson B.M., Malkan M.A., 1999, ApJ, 526, 579

Wehner E.H., Barger A.J., Kneib J.P., 2002, ApJ, 577, L83

White S.D.M., Frenk C.S., 1991, ApJ, 379, 52

Willott C.J., Rawlings S., Blundell K.M., Lacy M., Eales S.A., 2001, MNRAS, 322, 536

Willott C.J., Rawlings S., Blundell K.M., Lacy M., Hill G.J., Scott S.E., 2002, MNRAS, 335, 1120

Willott C.J., McLure R.J., Jarvis M.J., 2003a, ApJ, 587, L15

Willott C.J., Rawlings S., Jarvis M.J., Blundell K.M., 2003b, MNRAS, 339, 173

Wills B.J., Browne I.W.A., 1986, ApJ, 302, 56

Worthey G., Faber S.M., Gonzalez J.J., 1992, ApJ, 398, 69

Yasuda N., et al., 2001, AJ, 122, 1104

Young P.J., Westphal J.A., Kristian J., Wilson C.P., Landauer F.P., 1978, ApJ, 221, 721

Zel'dovich Y.B., 1964, Sov. Phys. Dokl, 9, 195

Zirm A.W., Dickinson M., Dey A., 2003, ApJ, 585, 90

Zirm A.W., et al., 2007, ApJ, 656, 66

APPENDIX A

Unusable observations, unsecured identifications, and non-detections

For completeness and future reference, $K-$band data for unusable observations, unsecured identifications, and non-detections are presented.

0016−12

Emission from the multi-component radio galaxy is contaminated by a saturated star to the west.

N2 850.03

No clear radio, $K-$band, or $I-$band counterpart is found for this submm source. The faint $K-$band source was selected owing to its bright $I-$band magnitude.

N2 850.05

This source is believed to be spurious, and is absent in the $1200\,\mu$m MAMBO survey. The $K-$band image is centred on the submm position.

N2 850.10

No clear radio, $K-$band, or $I-$band counterpart is found for this submm source. The $K-$band image is centred on a faint source undetected in IV02 or $I-$band imaging.

IV02 takes the bright object to the south-west to be the submm host. Two-dimensional modelling and curve-of-growth analysis suggests this object to be stellar in nature.

N2 850.11

No clear radio, $K-$band, or $I-$band counterpart is found for this submm source. The $K-$band image is centred on a low-redshift galaxy with a radio core to the south-west of the submm position.

N2 850.14

Emission from the bright submm host is contaminated by a saturated star to the south-west.

LE 850.01

A strong radio core is identified with this faint $K-$band detection.

LE 850.05

This source is believed to be spurious, and is absent in the $1200\,\mu$m MAMBO survey. The $K-$band image is centred on the submm position.

LE 850.09

No clear radio, $K-$band, or $I-$band counterpart is found for this submm source. The $K-$band image is centred on a saturation residual close to the submm position.

LE 850.15

No clear radio, $K-$band, or $I-$band counterpart is found for this submm source. The $K-$band image is centred on a faint $K-$band detection closest to the submm position.

LE 850.17

This radio ID form IV02 was intrinsically too weak for two-dimensional modelling.

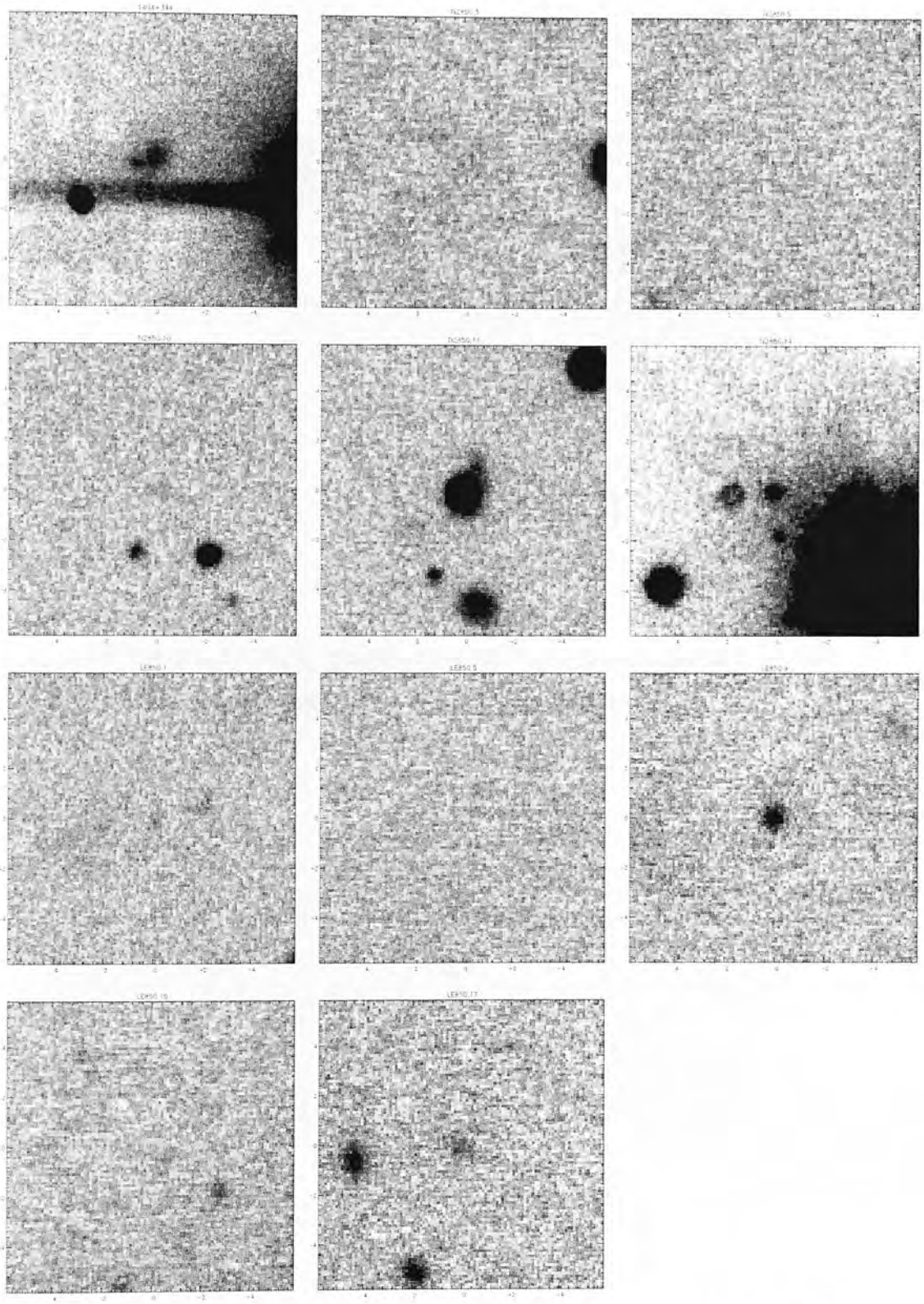

Figure A.1: Imaging of unusable objects, non-detections, and unconfirmed identifications.

APPENDIX B

Example spectra

Examples of the broad CIV (top panel) and H_β (bottom panel) emission lines used to determine black hole masses via the virial technique are shown.

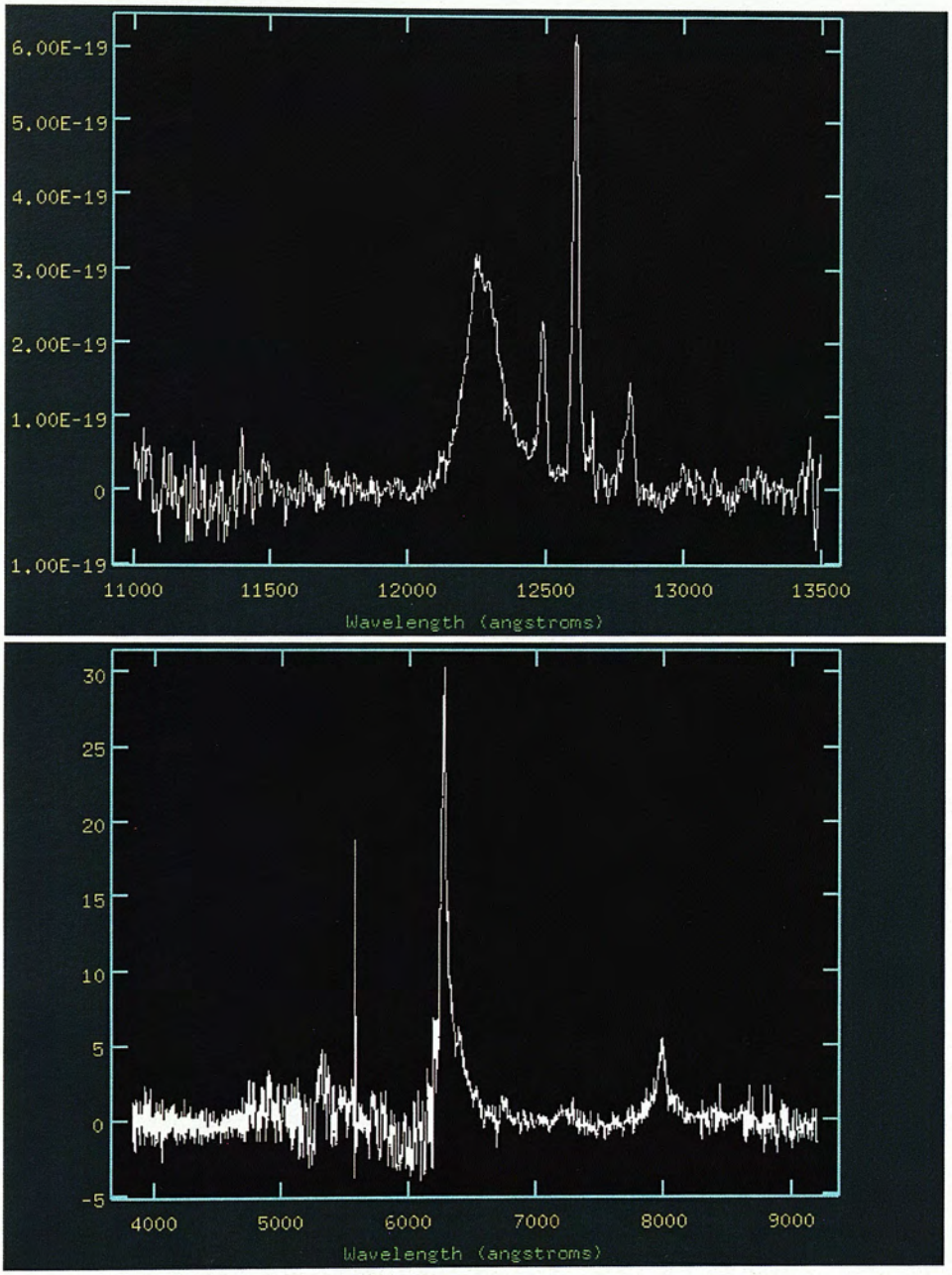

Figure B.1: Examples of continuum-normalised flux and wavelength-calibrated spectra from ISAAC (top) in $\mathrm{Ws^{-1}m^2\AA^{-1}}$ and the SDSS (bottom) in $E^{-17}\mathrm{ergs\,s^{-1}cm^2\AA^{-1}}$, including the broad 4861Å H_β and 1528Å CIV lines respectively.